ON THE MECHANICAL RESPONSE OF ANISOTROPIC GRANULAR MATERIALS

ON THE MECHANICAL RESPONSE OF ANISOTROPIC GRANULAR MATERIALS

By

ALIREZA AZAMI, M.Sc., B.Sc.

A Thesis

Submitted to the School of Graduate Studies
in Partial Fulfillment of the Requirements
for the Degree

Doctor of Philosophy

McMaster University

DOCTOR OF PHILOSOPHY (2009) **McMaster University**
(Engineering) **Hamilton, Ontario**

TITLE: **On the mechanical response of anisotropic granular materials**

AUTHOR: **Alireza Azami**
M.Sc., B.Sc., Sharif University of Technology, Tehran, Iran

SUPERVISORS: **Professor S. Pietruszczak**
Associate Professor P. Guo

NUMBER OF PAGES: xv, 126

ABSTRACT

The subject of this thesis is the mechanical response of inherently anisotropic granular materials. The study comprises both the experimental and numerical aspects and provides a rigorous methodology for the solution of geotechnical problems involving anisotropic frictional materials.

The experimental investigation has been carried out at both the material and structural levels. The material tests involved a series of direct shear, triaxial and hollow cylinder experiments on crushed limestone sand, whose mechanical characteristics are strongly affected by the orientation of the sample. In addition, a scaled foundation setup was designed and a series of experimental tests was carried out to examine the effects of anisotropy on bearing capacity.

The numerical part of this work was associated with development and implementation of a constitutive framework that describes the mechanical response of transversely isotropic frictional materials. The framework is based on elasto-plasticity and accounts for the effects of strain localization and inherent anisotropy of both the deformation and strength characteristics. An implicit scheme was proposed for identification of material parameters/functions, which incorporates predictions based on critical plane analysis. As a part of constitutive modeling, a suitable numerical algorithm was also developed to integrate the constitutive equations.

The constitutive framework has been implemented in a commercial FE package (ABAQUS). A series of numerical simulations were carried out focused on the assessment of the bearing capacity of a shallow foundation in transversely isotropic granular medium. The results of numerical simulations have been compared with the experimental data. A parametric study was also carried out aimed at examining the influence of various simplifications in the mathematical framework on its predictive abilities.

ACKNOWLEDGEMENTS

I would like to express my deepest and most sincere gratitude to my supervisors, Dr. Stan Pietruszczak and Dr. Peijun Guo, whose excellent guidance, unceasing encouragement, patience and expertise supported me throughout the course of my research.

I am deeply grateful to Dr. Amir Reza Khoei, my former supervisor at Sharif University of Technology, who introduced me to the field of Computational Mechanics/Geomechanics.

I would like to thank Mr. Peter Koudys for helping me with the development of the experimental setups and assisting me in the laboratory experiments.

Warmest thanks to my many friends who were there for me when I needed them. Thanks for being with me at happy and sad moments of my rather difficult life far from my family. Their friendship, support and care helped me to remain sane, overcome setbacks and stay focused on my graduate study.

I owe my heartiest gratitude to my family, my parents, my sister and brothers. My journey would not have reached here without their inspiration, encouragement and support. Thanks for loving me and believing in me. I am pleased to dedicate this thesis to my Mom and Dad. I would not be where I am or who I am if it was not for them.

TABLE OF CONTENTS

LIST OF ILLUSTRATIONS

LIST OF TABLES

CHAPTER 1
INTRODUCTION

1.1 Problem Statement

The main objective of this thesis is to develop a comprehensive and rigorous approach, including both experimental and numerical aspects, for the solution of geotechnical problems that involve anisotropic materials. This includes conducting a comprehensive experimental investigation, formulation of an inelastic constitutive model to describe the behavior of the material, development of a procedure to identify the material parameters, and an extensive numerical analysis.

On the practical side, the focus is on the assessment of bearing capacity of a shallow foundation in an inherently anisotropic particulate medium.

1.1.1 Material Anisotropy and Related Issues

Natural soils and sedimentary rocks are typically formed by deposition and progressive consolidation during the diagenesis. Such formations usually have a distinct internal structure. For example, in sedimentary rocks the microstructure is often visible to eye through the appearance of multiple sedimentary layers or bedding planes. As a result, the mechanical characteristics in both the elastic and inelastic ranges display a strong inherent anisotropy. Oda and Koishikawa (1977) and Oda et al. (1978) have shown that a distinct microstructure associated with the parallel alignment of particles is universally

observed not only in river, beach and dune sand but also in artificially deposited sands. Considering that the particle deposition takes place in the vertical direction, the plane of isotropy tends to be horizontal. The presence of anisotropy has a significant influence on the performance of geotechnical structures. For example, the anisotropy of strength properties of soil affects the stability of natural slopes and the bearing capacity of foundations. An appropriate consideration of anisotropy is also essential in the context of the design and stability analysis of underground structures, such as chemical and nuclear waste storage facilities, oil wellbores, tunnels, etc. While the presence of anisotropy in various geomaterials has been widely accepted, its modeling and experimental investigation still poses significant challenges.

In geotechnical engineering, laboratory tests such as direct shear, triaxial and hollow cylinder tests are typical in studies of the strength and the mechanical behavior of geomaterials. Over the last few decades, extensive experimental studies have been conducted on various geomaterials to investigate the anisotropy in their mechanical behavior. These include studies on natural clay deposits (e.g., Graham and Houlsby 1983, Kirkgard and Lade 1991, Nishimura et al. 2007), sand specimens (e.g., Oda et al.1978, Yamada and Ishihara 1979, Lam and Tatsuoka 1988) as well as sedimentary rocks (e.g., Atwell and Sandford 1974, Duveau et al. 1998, Oka et al. 2002). The most straightforward way to assess the anisotropic strength properties is to employ a direct shear test. Note that in this case the results cannot be explicitly used to investigate the deformation response of the sample as a continuum, as the displacement measurements are taken along a predetermined localization plane. Further more, due to the non-

uniformity of the displacement and stress fields, the stress-strain characteristics can not be evaluated from direct shear tests. In general, triaxial and hollow cylinder tests are more suitable to determine both strength and stress-deformation characteristics. However, the triaxial tests on transversely isotropic materials are also restrictive in the sense that the results are reliable only for vertical and horizontal samples. This stems from the fact that for inclined specimens the distortion is constrained by the presence of loading platens, which leads to non-uniformity in the resulting stress field. Note that several investigators conducted extensive triaxial experiments on inclined samples (e.g., Duveau et al. 1998, Oka et al. 2002); however the quantitative conclusions are, in this case, questionable. Finally, hollow cylinder tests have also been widely used to investigate the anisotropy in the response of geomaterials (e.g., Symes et al. 1984, Lade et al. 2008). In this case, the samples are typically prepared with horizontal bedding planes, but unlike in a triaxial test, the directions of the principal stresses can deviate from the principal material directions by any desired angle. Hollow cylinder tests are performed in two general loading configurations. In the first case, it is possible to have the rotation of principal stresses with equal intermediate and minor principal stresses (Hight et al. 1983, Symes et al. 1984). This is a desirable configuration to study the anisotropic effects; however, it is associated with a non-uniform stress state within the sample. In the other procedure, the loading combination is set up to provide a rather uniform stress distribution in the sample, but the intermediate and minor principal stresses are not equal and the effects anisotropy and the intermediate principal stress are coupled (Saada 1988 and 2000, Lade et al. 2008). Methods have been suggested in which the effect of

intermediate principal stress is solely studied using true triaxial tests, but again in the true triaxial testing device stress non-uniformity in the sample is an issue.

Numerical analysis of the behavior of geomaterials is not a trivial task either. Generally, the constitutive models employed for this purpose are based on the theory of elasto-plasticity. The major features that should be considered in the model are compaction/dilation, pressure sensitivity, anisotropy and localization. Implementation of any constitutive model requires the identification of material parameters, which is also challenging. The modeling of the mechanical response of anisotropic materials is typically based on the notion of a continuum with microstructure and requires the introduction of a tensorial measure (fabric tensor) that describes the anisotropy. The available methods are essentially based on the representation theorems of scalar function of tensor variables (e.g. Boehler and Sawezuk 1977 and Boehler 1987, Cowin 1987, Oka et al. 2002, Pietruszczak and Mroz 2001, Pietruszczak et al. 2002). While these approaches are mathematically rigorous, the main problem is the complexity of the formulation and, subsequently, the identification of material parameters.

1.1.2 Anisotropy and Bearing Capacity

In both structural mechanics and soil mechanics limit load calculations pose some of the most challenging problems in non-linear analysis. In structural mechanics limit load is generally associated with geometric non-linearity, so that large deformation theories have to be used for solving the problems. In contrast to this, the collapse of soil bodies is usually dominated by material non-linearity, which in numerical context falls

within the area of constitutive modeling.

Computation of limit loads in geomechanics, using numerical and analytical analyses, has received considerable attention in the literature. The stability of shallow foundations is traditionally assessed using the bearing capacity formula (Terzaghi 1943). The classical bearing capacity factors N_c, N_q, and N_γ (e.g. Meyerhof 1951) are functions of the internal friction angle, and reflect the contribution of cohesion, surcharge/embedment and self weight of the soil in the failure zone beneath the footing. Several different expressions for bearing capacity factors can be found in standard soil mechanics/foundation engineering text books (e.g. Bowles 1996, Das 1999, Das 2002, Craig 2004, Budhu 2006).

The bearing capacity equation stems from the limit equilibrium approach whose mechanical bases are rather questionable. A more rigorous methodology is that of limit analysis, which provides both lower and upper bound assessments (e.g., Chen 1975, Sarma and Iossifelis 1990, Drescher and Detournay 1993, Michalowski 1995 and 1997, Ukrichto et al. 2003, etc.). The basic premise of the limit analysis is the assumption of an associated rigid-perfectly plastic material and the bounds are established with no reference to the deformation history. A more accurate approximation involves a numerical assessment based on finite element analysis (e.g., Sloan and Randolph 1982, Griffiths 1982 and 1989, de Borst and Vermeer 1984, Frydman and Burd 1997, Woodward and Griffiths 1998, etc.). The latter can incorporate more advanced constitutive models that reflect the salient features of the mechanical response of the material.

Different issues associated with the assessment of the bearing capacity have been investigated in the literature using the finite-element method. The evaluation of the bearing capacity factor N_γ in particular has received a considerable attention (e.g. Frydman and Burd 1997, Woodward and Griffiths 1998). The effect of non-associativity of flow rule has also been addressed in some works including those of de Borst and Vermeer (1984) and Yin et al. (2001).

The issue that has not been adequately addressed in the assessment of ultimate bearing capacity is the influence of anisotropy of the material. Over the last decade attempts have been made to include the effect of anisotropy in the evaluation of bearing capacity (e.g., Siddiquee et al. 2001), but the problem has yet to be more rigorously approached. Another related issue, which is usually ignored in standard assessments of bearing capacity, is that of the onset of localized deformation. In the post-localized regime, the formulation of the problem requires a non-classical framework, such as a non-local approach, gradient dependent description (e.g., Bazant and Lin 1988, Bazant and Pijaudier-Cabot 1988, Triantafyllidis and Aifantis 1986), or similar, and this has not yet been properly addressed for the class of problems considered here.

1.2 Scope of the Work

This thesis is structured as follows. In Chapter 2, the results of experimental study are presented. The experimental program consisted of two independent parts. The first part involved a series of direct shear, triaxial and hollow cylinder tests aimed at investigation of the anisotropic material characteristics. The second one involved a series

of small-scale footing tests carried out to assess the variation of the bearing capacity with orientation of principal material axes. In Chapter 3, the mathematical formulation of the problem is outlined. The constitutive framework presented there is a multi-yield surface plasticity model, extended for the case of inherently anisotropic materials. In addition, the description of post-localized response is also addressed. Discussion regarding the procedure for identification of material functions/parameters is presented in Chapter 4. Subsequently, the integration algorithm for the elastoplastic constitutive equations is reviewed (Chapter 5), followed by some numerical examples. The results of numerical simulations of the footing test are also presented in Chapter 5 and the performance of the framework is compared with the experimental data given in Chapter 2. In addition, a parametric study is carried out aimed at examining the influence of various simplifying assumptions on the predictive abilities of the framework. The last chapter gives the conclusions as well as some suggestions for future work.

CHAPTER 2
EXPERIMANTAL INVESTIGATION

2.1 Introduction

In this chapter, the results of an experimental study, which is focused on examining the anisotropy effects in the behavior of geomaterials, are presented. First, a preliminary study that was aimed at selecting a material with the desired mechanical characteristics, is briefly outlined. Subsequent sections describe the testing procedures used, together with the experimental results and conclusions. The experimental program consisted of two parts. The first one involved a series of direct shear, triaxial and hollow cylinder tests aimed at investigating the anisotropic material characteristics, while the second part involved a series of small-scale footing tests carried out to assess the variation of the bearing capacity with orientation of principal material axes.

The examined materials were all prepared/remolded in the laboratory, and to obtain the desired internal microstructure different preparation methods were employed. It is very well established that naturally over-consolidated clayey deposits show significant anisotropy in their mechanical behavior (Graham and Houlsby 1983, Graham et al. 1983, Kirkgard and Lade 1991, Nishimura et al. 2007). Considering this fact, the first two trials in selecting the material for the investigations were clayey material, i.e. *Dundas clay* and *kaolinite*.

Bulk samples of Dundas clay (a silty clay material) were remolded in a cylindrical mold, 10cm in diameter and 30cm high. The inside of the mold was sprayed with Teflon to reduce the friction between soil and mold, and thus the sample disturbance during molding and extracting the sample from the mold. Samples with 12% moisture content were consolidated in 5 layers of about 4cm thickness under an axial stress of 500 kPa. Each layer was kept under the pressure for 5 min. To prevent separation between the layers, the surface of each consolidated layer was scratched with a sharp instrument before adding the next consecutive layer. This preparation method provided samples with a set of bedding planes normal to the axis of the cylinder, i.e. normal to the axial pressure. The bulk sample was then extracted form the mold with a hydraulic jack. Subsequently, a number of direct shear samples, with different orientations, were cut from the bulk sample (see Fig 2-1), and a series of direct shear tests were performed.

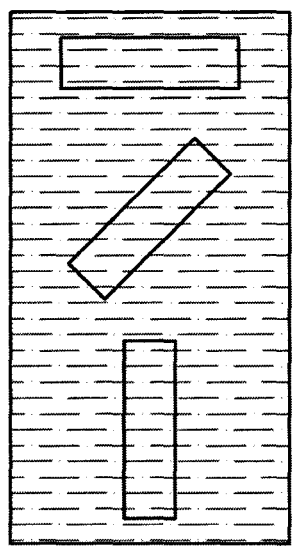

Fig 2-1 Cutting direct shear samples with different bedding plane orientations from the bulk sample

The results of direct shear tests, as presented in Fig 2-2a, did not show a significant anisotropy in the behavior of the material, even though the over-consolidation ratios for the tests were quite high, i.e. OCR=5.0, 7.5 and 10.0. Therefore, it was decided to increase the consolidation time so that more significant changes in the microstructure could develop. For the next series of tests, the bulk sample within the mold was placed under the same 500 kPa axial stress for an additional consolidation time of 41 hrs. Again the results did not show any significant anisotropy in the strength and the deformation response of the material (see Fig 2-2b). Allowing even more time, e.g. one week, for consolidation helped to induce a rather weak anisotropy in the material, as shown in Fig 2-2c, but due to the time constraints of the study, it was decided to change the type of the material.

Assuming that the silty particles in Dundas clay are the main cause that obstructs the development of anisotropic behavior, the same procedure was employed in examining the response of kaolinite, a white clay material that consists of long clay mineral sheets. Although, the consolidation time was one week, the results again did not show significant anisotropy in the mechanical response of this material either (see Fig 2-3). Allowing a much longer time for consolidation might have lead to more pronounced effects, but considering that all tests on clayey materials require long period, due to their low permeability, a sandy material was eventually selected for the experiments conducted in this study.

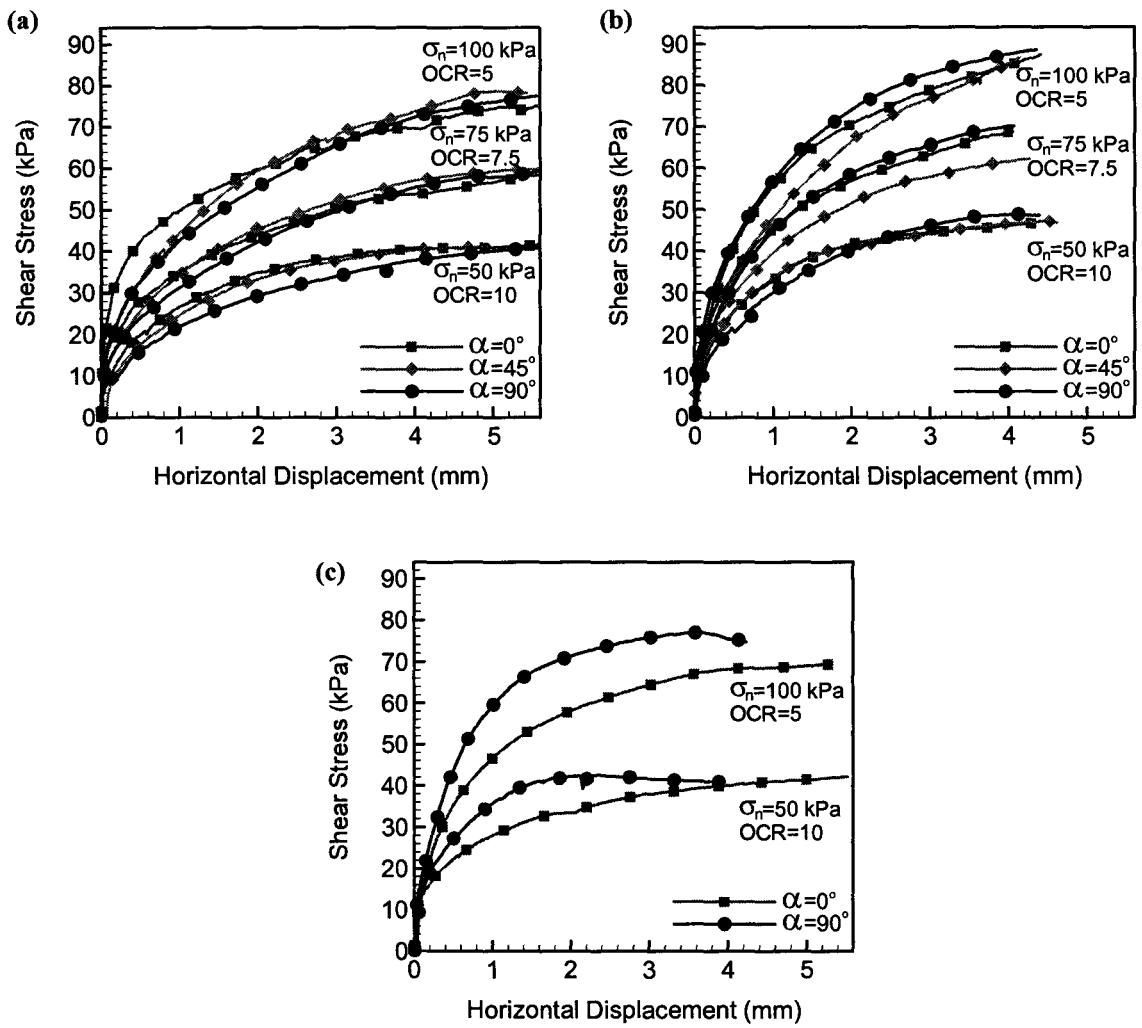

Fig 2-2 Direct shear test results on Dundas Clay; variation of shear stress versus horizontal displacement for samples with different bedding plane orientations with different overconsolidation ratios; (a) no time for additional consolidation, (b) consolidated for an additional 41 hrs and (c) consolidated for an additional one week

The particular material, which was chosen, was taken from the LAFARGE PIT at Hwy 5, Dundas. The material is *crushed limestone* with elongated angular-shaped aggregates of particle size between 0.15mm and 2mm (sieve#10 to sieve #100). The samples were prepared by the sand rain method using a constant falling height of 80cm. Considering that the particle deposition takes place in the vertical direction, i.e. the

direction of sand rain, a major plane of each particle tends to be arranged horizontally. The plane characterized by the parallel alignment of particles, which is in turn normal to the direction of deposition and the preferred material axis, can be tentatively called the *bedding plane* (Oda and Koishikawa 1979). The sand rain method has proven to be a consistent sample preparation method providing reproducible testing samples. All the samples prepared with the mentioned method had a void ratio of approximately $e = 0.6$. The samples proved to be highly anisotropic. The mechanical properties were examined using the direct shear, triaxial and hollow cylinder devices. The details on the mechanical response, including specification of the conditions at failure, are provided in the following sections.

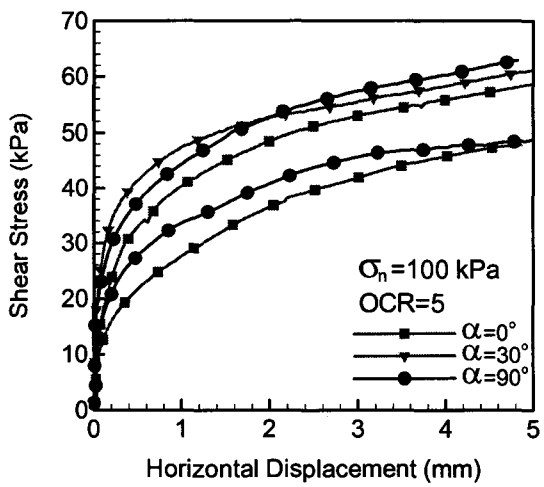

Fig 2-3 Direct shear test results on kaolinite; variation of shear stress versus horizontal displacement for samples with different bedding plane orientations; samples were consolidated for one week

2.2 Direct Shear Tests

Direct shear test is a displacement-controlled test. A specimen is placed in a shear box, with typical dimensions of $60 \times 60 \times 40\text{mm}$, and consolidated under a vertical load. The box is split into two separate halves, an upper and a lower. After the application of normal load and completion of the consolidation stage, the sample is sheared by applying horizontal displacement to the upper portion of the box. More details on the direct shear device and the standard testing procedure can be found in ASTM D 3080.

The direct shear test imposes stress conditions on the soil sample that force the failure to occur along a predetermined orientation, i.e. along the horizontal plane that separates the two halves of the box. The test is typically performed on three or four identical specimens under different levels of normal stress. The classical shear strength parameters, i.e. friction angle (φ) and cohesion (c), are then determined by finding a linear best fit to the obtained experimental data.

The advantages of the direct shear test are:

1- The test is cheap, fast and simple; especially for sands.

2- Failure occurs along a single surface, which approximates observed slip or shear type failures in natural soils.

Disadvantages of the test include:

1- It is difficult or impossible to control drainage, especially for fine-grained soils.

2- Failure plane that is forced, may not be the weakest or critical plane

3- Non-uniform stress conditions exist in the specimen.

4- The principal stresses rotate during shear, and the rotation cannot be controlled.

Because the drainage conditions, during all stages of the test, influence the shear strength of soils, the direct shear test is mainly applicable to relatively clean sands which are free draining during shear. For clay soils, some consolidation may occur during shear, which would give a larger shear strength than actual. Therefore the test is not generally recommended for cohesive soils.

Since the failure plane is fixed in this test, it is possible to measure the shear strength on planes with specific inclinations relative to the material axes. This very well serves the purpose of the investigation of directional dependency of the strength parameters.

2.2.1 Sample Preparation Method

In order to be able to prepare samples with different bedding plane orientations some modifications have been made to the standard shear box (Guo 2008). Fig 2-4 shows the modified shear box positioned to be filled with sand by the sand rain method. Fig 2-4a shows the sample preparation method and Fig 2-4b shows a schematic picture of the shear box device with the soil sample inside. As mentioned earlier, the test samples were prepared by the sand rain method using a constant falling height of 80cm. A vertical cut was made on one side of the shear box, providing the possibility of filling the box with sand at desired orientation by positioning the box on a tilted base. Considering that the particle deposition takes place in the vertical direction, i.e. the direction of sand rain, a major plane of each particle tends to be arranged horizontally. The deposition angle (or

the bedding plane orientation) α, here is the angle between the sand rain direction and the direction normal to the plane of isotropy.

As shown in Fig 2-4a with the sand rain method the shear box was literally buried under the sand; afterward the extra material was carefully removed, the sample was trimmed and the removable side parts of the box were reassembled. The sample contained in the shear box (Fig 2-4b) was then ready to be put in the direct shear testing device. The sand rain method has proven to be a consistent sample preparation method providing reproducible test samples in all the tests presented in this chapter. All the samples were prepared with a void ratio of approximately $e = 0.6$. The direct shear tests were performed on dry samples, with a displacement rate of 0.18 mm/min. Since the failure plane in the direct shear apparatus is always horizontal, the shear strength characteristics could be examined for different values of the deposition angle α.

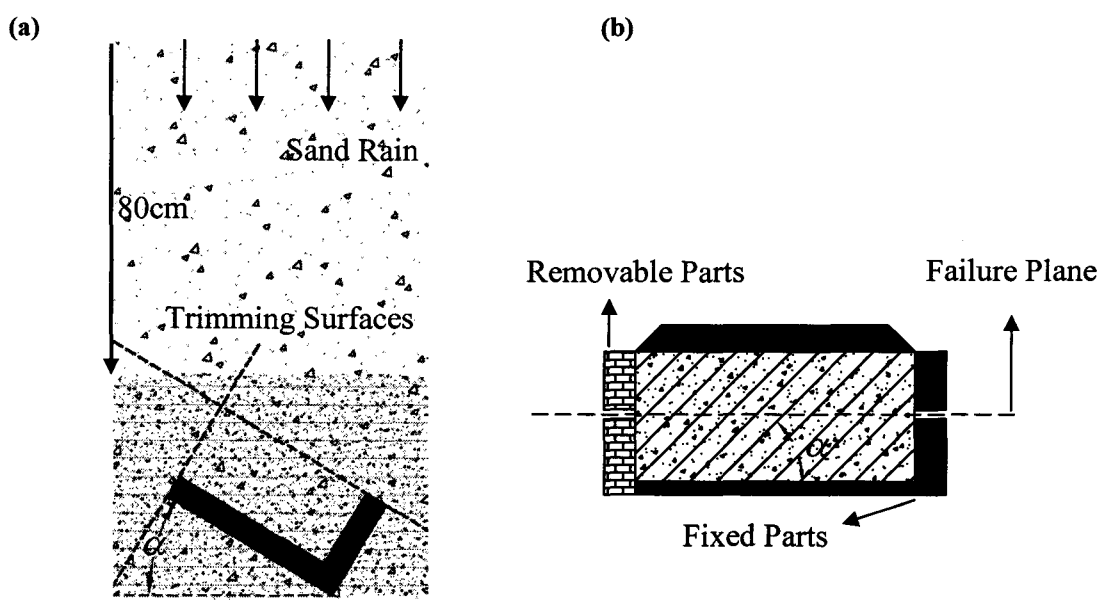

Fig 2-4 (a) Schematic diagram of sample preparation for direct shear tests; (b) modified shear box

2.2.2 Direct Shear Test Result

The direct shear tests were carried out at four different levels of normal stress, σ_n=1, 25, 50, 75kPa. Fig 2-5 to Fig 2-8 show the mechanical response of the material for different values of α. Due to stress non-uniformity in the direct shear specimen, the deformation characteristics cannot be evaluated form this test. The variation of shear stress and the corresponding evolution of volume change are presented in Fig 2-5 toFig 2-8. Clearly, the material shows a significant degree of anisotropy, as the strength is profoundly affected by the direction of deposition. The directional dependency of the shear strength of the material seems to be more intense at lower levels of normal stress, but it is persistent for all stress levels. At low normal stresses, the evolution of volume change shows a progressive dilation (see Fig 2-5b), while at higher normal stresses a transition from compaction to dilatancy takes place as the shear stress increases (see Fig 2-8b).

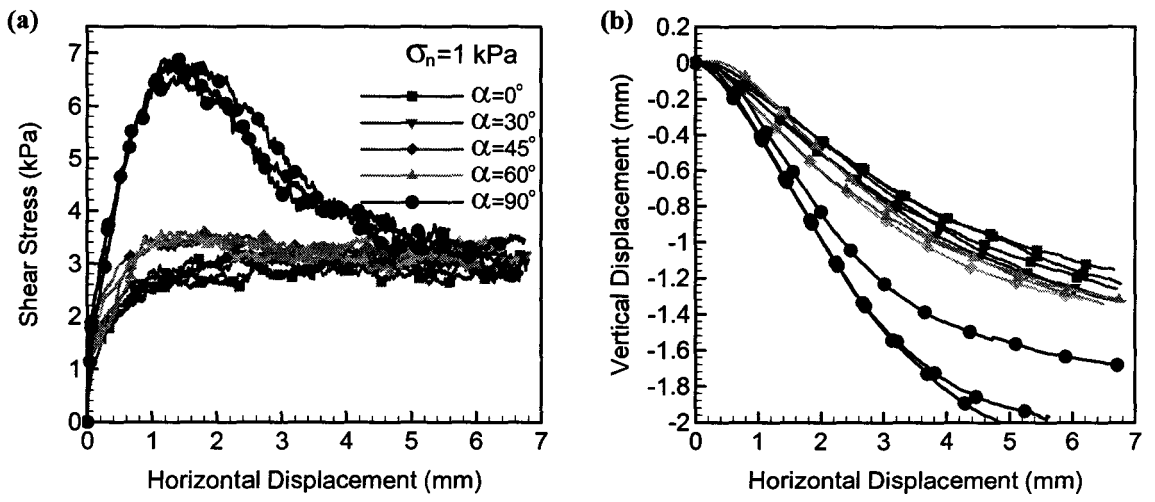

Fig 2-5 Mechanical response at normal stress of $\sigma_n = 1$ kPa for different values of α ; (a) shear stress-horizontal displacement characteristics, (b) evolution of volume change

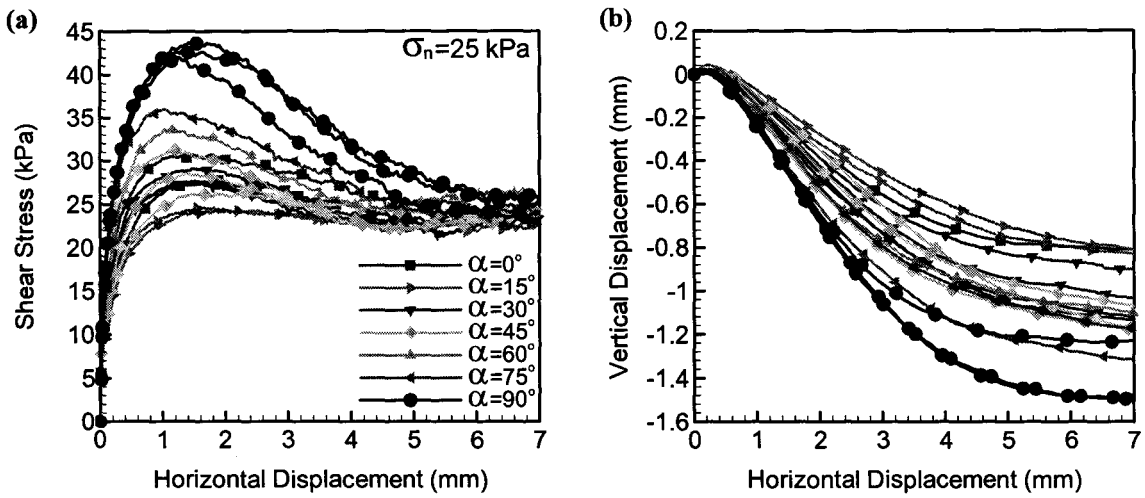

Fig 2-6 Mechanical response at normal stress of $\sigma_n = 25$ kPa for different values of α ; (a) shear stress-horizontal displacement characteristics, (b) evolution of volume change

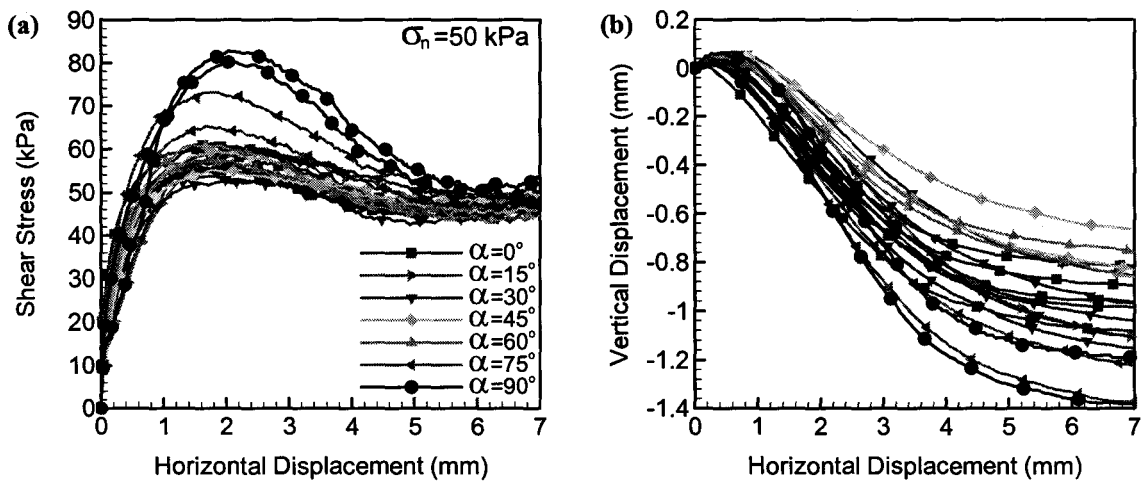

Fig 2-7 Mechanical response at normal stress of $\sigma_n = 50$ kPa for different values of α ; (a) shear stress-horizontal displacement characteristics, (b) evolution of volume change

Considering a linear form of Mohr-Coulomb criterion, the direct shear test under low normal stress (σ_n=1) emphasizes the anisotropy in the apparent cohesion of the material. At the same time, the tests under higher normal stresses give more focus to the

anisotropy in internal friction angle. Fig 2-9 shows the failure envelopes for different values of α along with the experimental data obtained from direct shear tests. It is evident that the material develops an apparent cohesion due to interlocking of aggregates, though it only consists of sandy non-plastic particles.

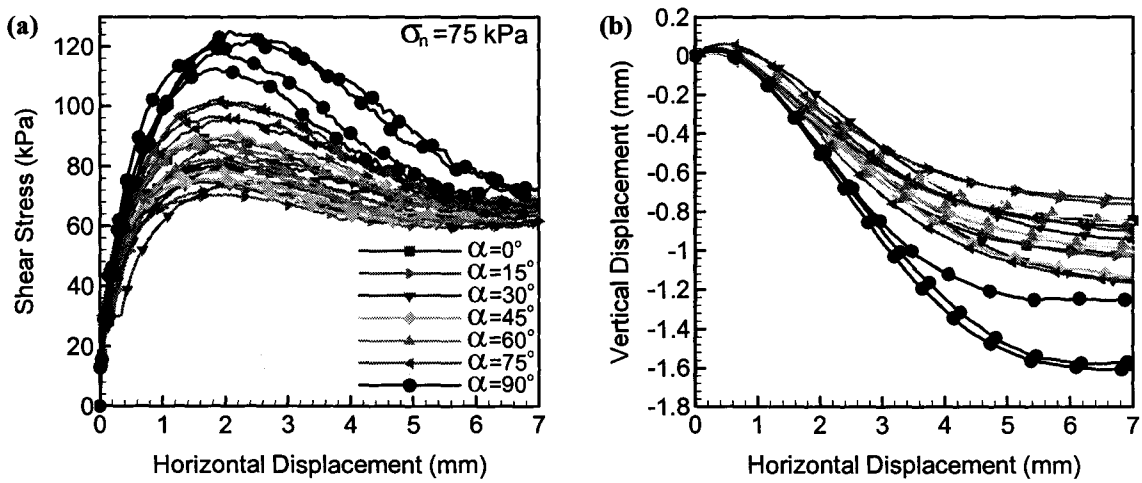

Fig 2-8 Mechanical response at normal stress of $\sigma_n = 75$ kPa for different values of α ; (a) shear stress-horizontal displacement characteristics, (b) evolution of volume change

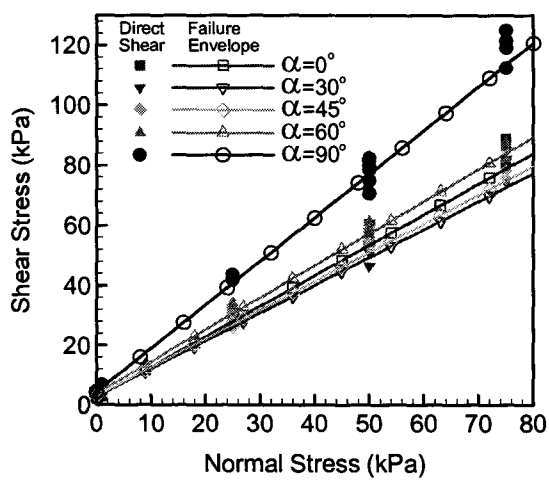

$\tau = 1.0196\,\sigma_n + 2.48$ $\alpha=0^{O}$

$\tau = 0.9327\,\sigma_n + 2.6$ $\alpha=15^{O}$

$\tau = 0.9316\,\sigma_n + 2.8$ $\alpha=30^{O}$

$\tau = 0.9599\,\sigma_n + 3.0$ $\alpha=45^{O}$

$\tau = 1.0693\,\sigma_n + 3.86$ $\alpha=60^{O}$

$\tau = 1.3000\,\sigma_n + 4.2$ $\alpha=75^{O}$

$\tau = 1.4538\,\sigma_n + 4.41$ $\alpha=90^{O}$

Fig 2-9 Coulomb failure envelopes for different values of α

Fig 2-10a and Fig 2-10b present the distribution of the friction angle ϕ and cohesion c, as a function of the deposition angle. Both the cohesion and the friction angle are direction dependent, but the strength anisotropy is more pronounced in the friction angle. The maximum friction angle, $\phi \simeq 56^0$, corresponds to vertical bedding plane ; the minimum, $\phi \simeq 44^0$, occurs at $\alpha \simeq 30^0$.

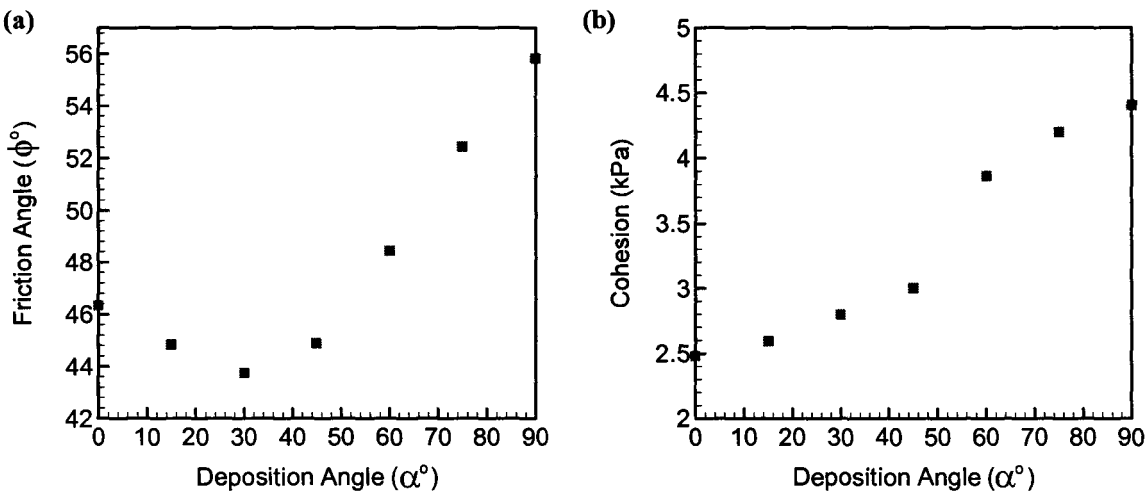

Fig 2-10 Variation of (a) the friction angle ϕ and (b) cohesion c with the deposition angle α

2.3 Triaxial Tests

The triaxial tests are used to measure the shear strength and study deformation characteristics of a geomaterials under controlled drainage conditions (e.g. Holtz and Kovacs 1981, Head 1998). In a conventional triaxial test, a cylindrical specimen is encased in a rubber membrane and is placed in a triaxial compression chamber. The specimen is subjected to a confining fluid pressure, and then loaded axially (or laterally) to failure. Connections at the ends of the specimen permit controlled drainage of pore

water from the specimen. Prior to shear, the three principal stresses are equal to the chamber fluid pressure. During shear, the major principal stress, σ_1 is equal to the applied axial stress plus the chamber pressure, σ_3. The intermediate principal stress, σ_2 and the minor principal stress, σ_3 are identical in the test, and are equal to the confining or chamber pressure.

There are 3 types of triaxial tests, depending on the drainage conditions at the consolidation and shearing phases of a triaxial test. Unconsolidated-undrained (UU) or quick (Q) triaxial test performed with the drainage valve closed for all phases of the test (ASTM D2850). In consolidated-undrained (CU) triaxial tests drainage is allowed to take place during the application of the confining pressure, but not during the shearing phase (ASTM D4767). The excess pore pressures can be measured for the shearing phase. Consolidated-drained (CD) test, also called slow test (S), is performed with free drainage condition for the whole period of the test, i.e. no generation of excess pore pressure during the test. This may require a slow rate in application of load. The volume change of the sample during consolidation and shear can be measured.

The main advantages of the triaxial test over the direct shear test are the uniformity of the stress and deformation fields in the sample, and the accuracy of the measurements in volume change of the sample.

2.3.1 Sample Preparation Method

The triaxial tests can be conducted on samples with vertical and horizontal bedding planes only ($\alpha = 0^{O}$ and $\alpha = 90^{O}$) ; although several investigators carried out

tests on inclined samples as well (for instance see Lo and Hori 1979, Duveau et al. 1998, Oka et al. 2002). Note that for inclined bedding planes, the sample has a tendency to distort. In a triaxial environment, however, this distortion is constrained by the presence of loading platens. Consequently, the stress field is no longer uniform and the results, in the sense of variation of strength and deformation characteristics with sample orientation, are not fully reliable. Therefore in this work triaxial tests were performed only on samples with vertical and horizontal bedding planes.

The samples were prepared in a rectangular prism mold with the dimensions of $100 \times 50 \times 50$ mm. Analogous to the direct shear samples, the triaxial samples were prepared by sand rain method using a constant falling height of 80cm. The sample preparation method is illustrated in Fig 2-11.

In order to preserve the composition of the fabric, the specimen with the mold was first submerged in water. Then, excess water was drained out under gravity to obtain a moist specimen with low moisture content. The entire set up, i.e. the mold and the moist sample within, was then frozen. The frozen specimen was subsequently removed from the mold and transferred to the base of the triaxial cell and enclosed in a membrane. A small confining pressure was then applied while unfreezing the specimen. Finally, the specimen was saturated and consolidated under a hydrostatic pressure prior to the shearing phase. To minimize the end friction effects two layers of membrane with silicon grease in between were placed between the sample and loading plates. Proper cuts were made on the membranes to allow both seepage through the sample and free lateral expansion of the sample.

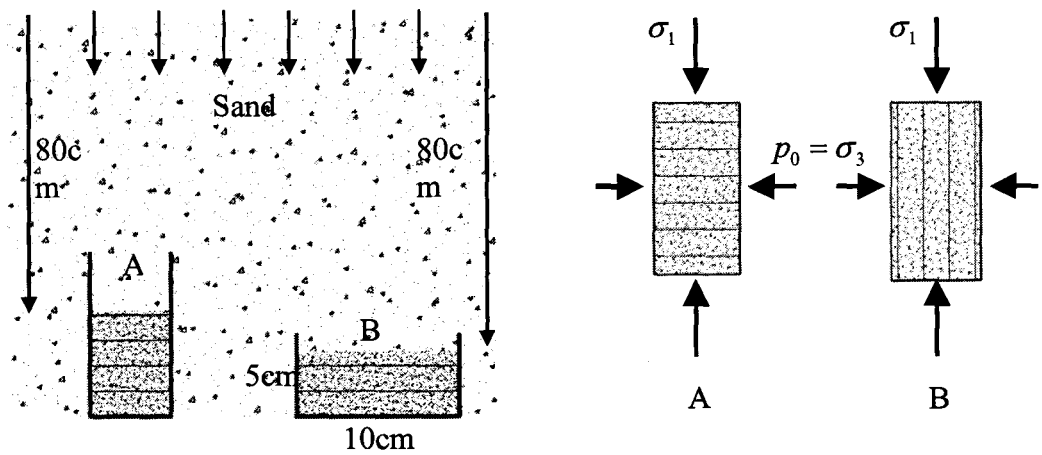

Fig 2-11 Schematic diagram of sample preparation and loading configuration for triaxial tests

2.3.2 Triaxial Test Results

The tests were conducted under four levels of confining pressure, i.e. $p_0 = 10, 50, 100, 150$ kPa. The variations of deviatoric stress and volumetric strain with the increasing axial strain for each level of confining pressure are presented in Fig 2-12 to Fig 2-15.

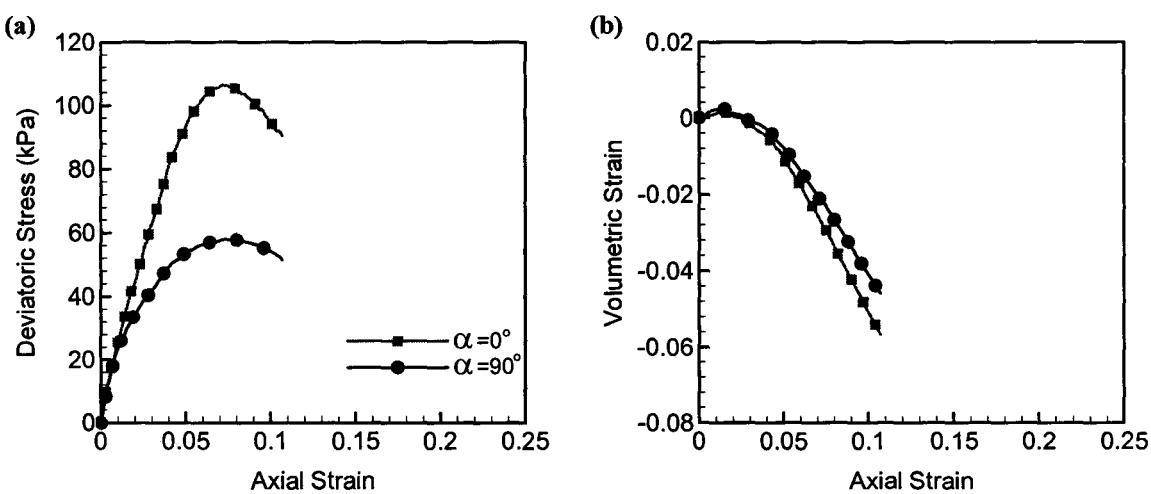

Fig 2-12 Results of triaxial test at confining pressure $p_0 = 10$ kPa ; variation of (a) deviatoric stress and (b) volumetric strain with axial deformation

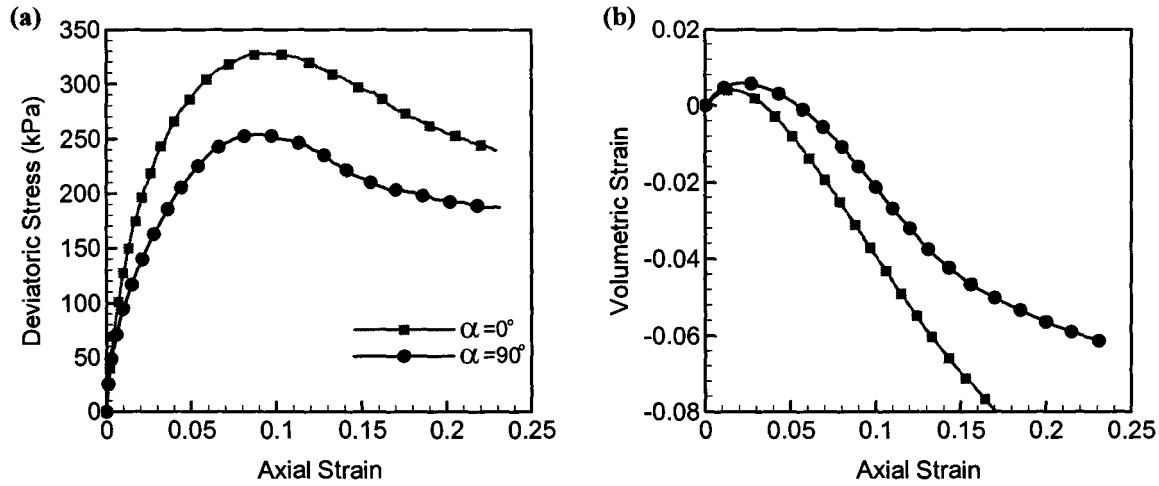

Fig 2-13 Results of triaxial test at confining pressure $p_0 = 50$ kPa ; variation of (a) deviatoric stress and (b) volumetric strain with axial deformation

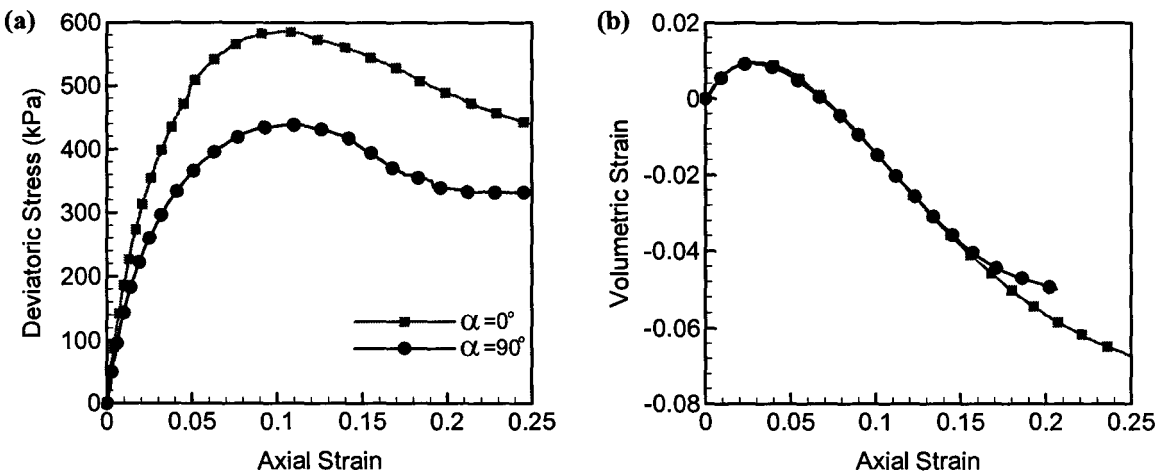

Fig 2-14 Results of triaxial test at confining pressure $p_0 = 100$ kPa ; variation of (a) deviatoric stress and (b) volumetric strain with axial deformation

Each curve is the average of at least two tests with the corresponding testing conditions. This is illustrated in Fig 2-16, which shows the results of two consecutive tests at $p_0 = 100$ kPa. It is clear that the testing procedure and the sample preparation method gave results that were very consistent and repeatable.

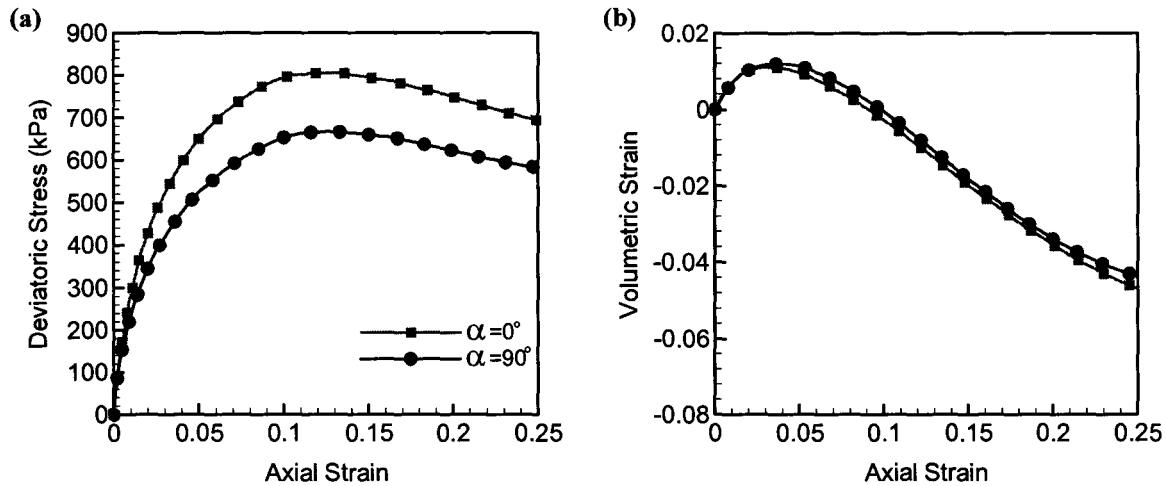

Fig 2-15 Results of triaxial test at confining pressure $p_0 = 150$ kPa ; variation of (a) deviatoric stress and (b) volumetric strain with axial deformation

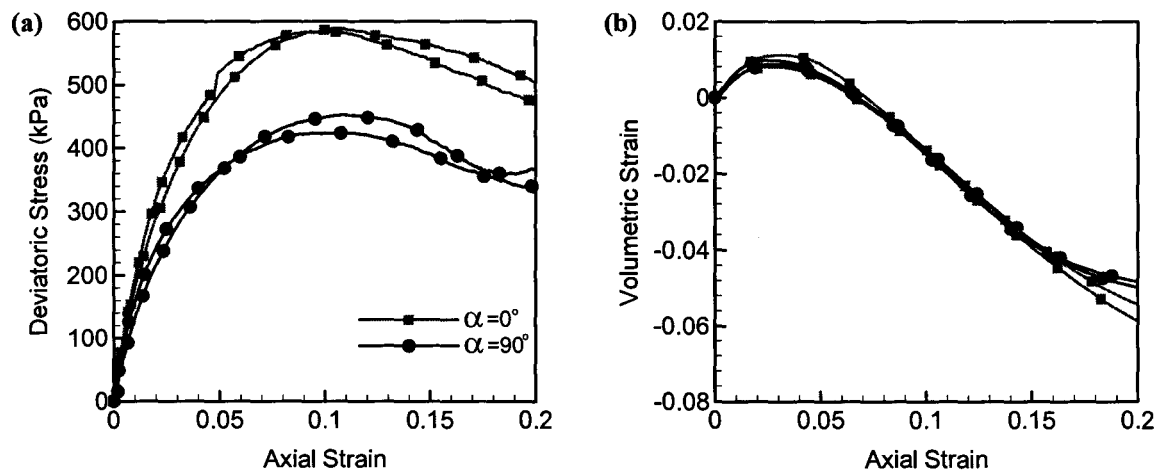

Fig 2-16 Results of triaxial test at confining pressure $p_0 = 100$ kPa ; variation of (a) deviatoric stress and (b) volumetric strain with axial deformation

It is evident that the behavior is orientation-dependent. The anisotropy effects, in terms of both strength and deformation response, are more pronounced at low confining pressures and gradually decrease as the confinement increases. Regarding the volume change characteristics, it is evident that at low confinements, the predominant mode is

dilation; i.e. the compaction stage is negligible. At higher confining pressures, similar to direct shear test results, a transition from compaction to dilatancy is observed.

In general, the triaxial tests gave results that were consistent with trends reported in direct shear. Note that the results of both triaxial and direct shear tests will be used later in Chapter 4 to identify the material parameters for the constitutive model proposed in Chapter 3.

2.4 Hollow Cylinder Tests

Long hollow cylindrical samples subjected to combination of hydrostatic, axial and torsional stresses (see Fig 2-17) have been widely used to study the behavior of geomaterials under combined stresses. One of the advantages of this configuration is the ability to conduct tests at different orientations of principal stress axes, relative to the axes of symmetry of the material. The state-of-the-art paper by Saada (1988) gives extensive details about hollow cylinder devices, their advantages and limitations.

The hollow cylinder samples can be tested under various and quite elaborated stress paths. Different loading combinations of inner (p_i) and outer (p_o) cell pressures, axial load (F) and torque (M) can be applied leading to a complex 3D stress state. Compared to the triaxial tests, where the principal stress axes coincide with the material axes (vertical and horizontal), in hollow cylinder device it is possible to have non-coaxial material and principal stress triads.

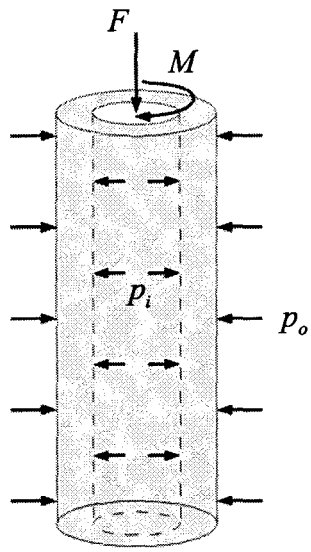

Fig 2-17 Schematic diagram of hollow cylinder sample and its loading combination

The average state of stress in the hollow cylinder sample shown in Fig 2-17, with inner and outer radius of r_i and r_o, is as follow (Saada 1988 and 2000)

$$\sigma_a = \frac{F}{\pi(r_o^2 - r_i^2)} + \frac{p_o r_o^2 - p_i r_i^2}{r_o^2 - r_i^2}$$

$$\sigma_r = \frac{p_o r_o + p_i r_i}{r_o + r_i} \quad , \quad \sigma_\theta = \frac{p_o r_o - p_i r_i}{r_o - r_i} \quad , \quad \tau_{\theta z} = \frac{3M}{2(r_o^3 - r_i^3)} \tag{2.1}$$

Testing procedure usually starts with consolidating the sample under a hydrostatic state of stress by applying equal inner and outer cell pressure, i.e. $\sigma_a = \sigma_r = \sigma_\theta = p_i = p_o$. The addition of axial and tortional stresses causes a rotation in the direction of major and minor principal stresses. If the ratio of $\Delta\sigma_a / \Delta\tau_{\theta z}$ remains constant, this rotation also remains constant. In addition, tests are usually performed at a constant mean stress, so that the stress path remains within the initial octahedral plane (Π plane). This is done by

adjusting the cell pressures while the axial load and torque are being increased/decreased such that $\Delta\sigma_a / \Delta\tau_{\theta z} = const.$ and $\sigma_a + \sigma_r + \sigma_\theta = const.$. This provides the possibility of investigating the effects of anisotropy at certain stress levels.

2.4.1 Sample Preparation and Testing Method

The hollow cylinder samples, with 100mm outer diameter, 60mm inner diameter and 200mm high, were again prepared by the sand rain method. Sample preparation technique is illustrated schematically in Fig 2-18. To obtain cylindrically shaped samples, suction was applied between the outer membrane and the outer wall of the mold; a thin layer of filter paper was placed in-between them to distribute the suction evenly. For the inner side, the membrane was tight enough not to leave any gaps between the membrane and the inner wall of the mold.

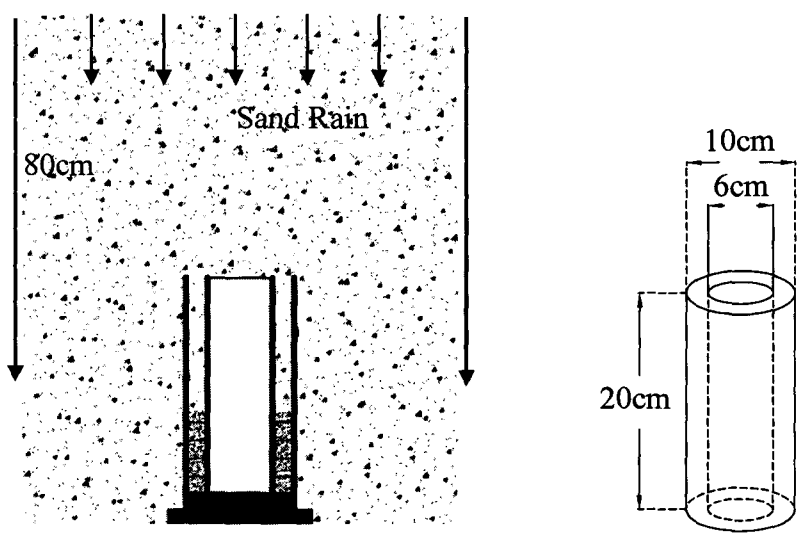

Fig 2-18 Schematic diagram of sample preparation method for hollow cylinder tests

After filling the mold by the sand rain method, top of the sample was trimmed and the sample within the mold was carefully transferred and mounted on the device. The top cap was placed on the sample and rubber o-rings were put in place to fully isolate the sample from the inner and outer chambers. A small suction was then applied to the sample so that it remained stable while the mold was being removed. The inner and outer cells were filled with water, sample was saturated and then the shearing phase started.

In general two different testing methods have been suggested for the hollow cylinder apparatus. In the first one the rotation of principal stress axes takes place, while the averaged principal stresses are such that $\sigma_1 > \sigma_2 = \sigma_3$ (Hight et al. 1983, Symes et al. 1984). To produce such a stress combination the inner and outer cell pressures should be different, and that causes stress non-uniformity along the sample wall. The non-uniformity becomes more pronounced when the material axes and the directions of principal stresses depart. In the second method, the rotation of principal stress axes takes place while the inner and outer cell pressures are kept equal, providing a rather uniform distribution of stress in the specimen. The principal stress combination in this case is such that $\sigma_1 > \sigma_2 > \sigma_3$ where the effects of intermediate stress and rotation of principal stresses are coupled (Saada 1988 and 2000, Lade et al. 2008). In this configuration the relationship between the principal stresses and the angle α defining deviation of the major principal stress from the vertical axis, is

$$\sin^2 \alpha = \frac{\sigma_2 - \sigma_3}{\sigma_1 - \sigma_3} \tag{2.2}$$

Note that compared to triaxial test configuration presented earlier, α here is the same as the deposition angle. In this study all the hollow cylinder tests were performed using the second procedure.

2.4.2 Hollow Cylinder Test Results

The adopted loading combination was such that the directions of major and minor principal stresses could be rotated from vertical and horizontal directions by a constant value of α during the shearing phase. The intermediate principal stress was fixed in the direction normal to the wall of the specimen. In view of (2.2), the state of stress in hollow cylinder tests is representative of a triaxial compression test for $\alpha = 0^0$, and a triaxial extension test for $\alpha = 90^0$. For intermediate values of α, the principal stress σ_2, which is the same as inner and outer cell pressures, is intermediate between major and minor principal stresses.

The hollow cylinder tests reported here were performed with equal inner and outer cell pressures and under a constant mean stress of $p = 100\,\text{kPa}$. Rotation of major principal stress from the vertical axis, i.e. α, was kept constant for each test. The evolution of deviatoric stress and volumetric strain with the increasing octahedral shear strain is presented in Fig 2-19 for different values of α.

As mentioned earlier, the results presented in Fig 2-19 incorporate the coupled effects of anisotropy and the intermediate principal stress on the mechanical behavior of the material. Therefore, it is not possible to study the anisotropy alone on the basis of this data. In view of this, the results of hollow cylinder tests were not directly used in

identification of the material parameters, but instead they were employed, later in Chapter 4, to verify the performance of the model.

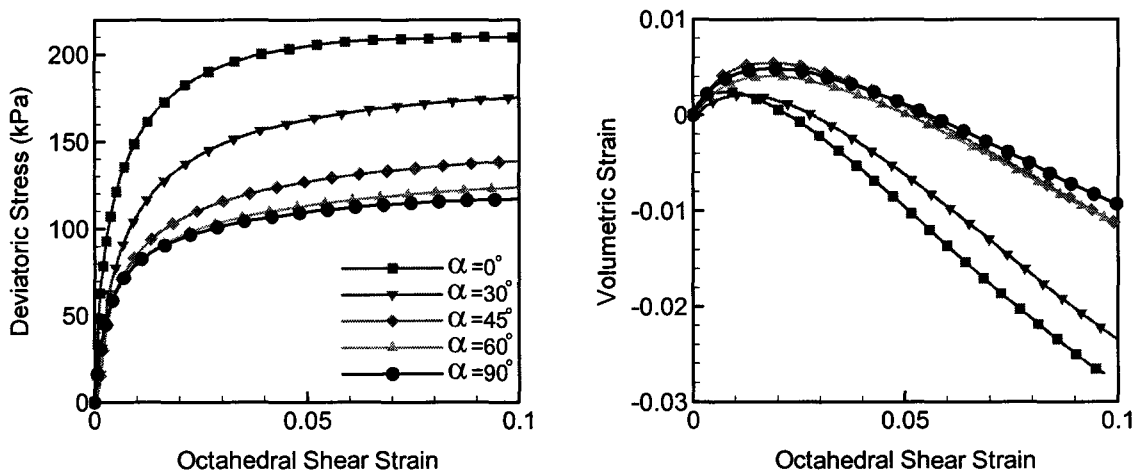

Fig 2-19 Results of hollow cylinder tests at a constant mean pressure $p = 100$ kPa; variation of deviatoric stress and volumetric strain with octahedral shear strain

2.5 Scaled Shallow Foundation Model Tests

A number of small-scale model tests were performed in order to examine the variation of bearing capacity of a rigid foundation as a function of the angle of deposition of the material. All tests were later simulated via finite element analysis that incorporated the constitutive framework proposed in Chapter 3. The details on numerical simulations, including a comparison with experimental data, are given in Chapter 5.

2.5.1 Scaled Model Preparation Method

The experimental setup employed in this study is shown schematically in Fig 2-20. The material was placed inside an aluminum box (50cm wide, 35cm high and 20cm

thick) that had two fixed and two removable sides, Fig 2-21. The front and the back plates were made of thick Plexiglas. The soil was again prepared by the sand rain method using a constant falling height of 80cm. The setup gave the possibility of producing samples at desired orientation by keeping the box tilted and maintaining the sand rain height constant. The procedure was able to provide fairly uniform and reproducible specimen with a void ratio of approximately $e \simeq 0.6$. Note that the solid lines shown in the schematic of test setup, which are normal to the direction of deposition, define the planes of material isotropy. All tests were carried out under plane stain conditions. In order to reduce the friction along the sides, the Plexiglas plates were covered by two layers of transparent plastic sheets that were lubricated with a viscous oil. After filling, the box was placed flat on the floor and the top layer of soil was trimmed. The footing, 5.7cm wide and 20cm long, was made of a 2.5cm thick rigid aluminum plate. The tests were performed by applying vertical displacements at the midpoint of the footing, while allowing for the in-plane rotation.

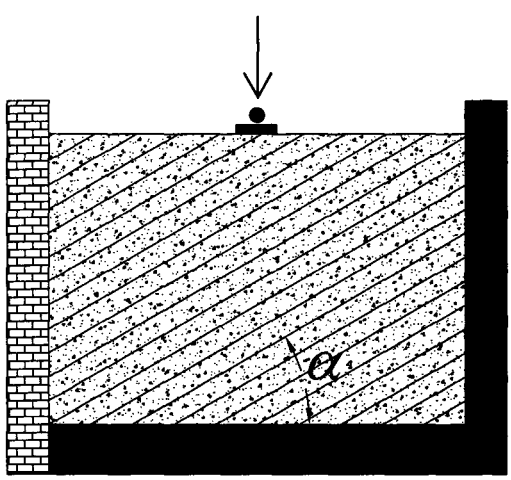

Fig 2-20 Experimental setup for the footing test (Note: α is the direction of deposition of the material)

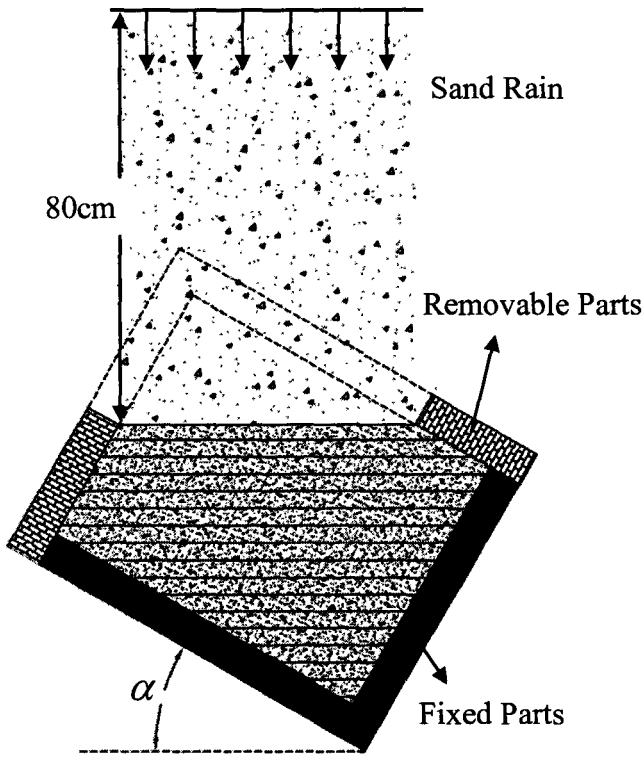

Fig 2-21 Schematic diagram of sample preparation by sand rain

2.5.2 Scaled model Test Results

The main results of experimental tests are shown in Fig 2-22. Fig 2-22a presents the load-displacement curves for selected values of the deposition angle α, ranging from 0^{o} to 90^{o}. Note that for each orientation a number of tests were performed in order to check the consistency of the testing procedure. Fig 2-22b presents the best fit characteristics obtained through the least square approximation. It is evident that both the initial stiffness as well as the ultimate load are affected by the direction of deposition. Fig 2-22c shows the variation of the average ultimate bearing capacity with the deposition angle α. The maximum corresponds to $\alpha = 0^{o}$, while the minimum is attained at $\alpha \simeq 60^{o}$.

For orientations of $\alpha = 30^{\circ}, \alpha = 45^{\circ}$ and $\alpha = 60^{\circ}$ the in-plane rotation of the footing was observed from the early stages of the loading process. For vertical and horizontal configurations, $\alpha = 0^{\circ}$, $\alpha = 90^{\circ}$, the in-plane rotation took place only when the load was close to the ultimate bearing capacity. In all cases a diffused failure mode was observed, i.e. no localization took place at the macroscale.

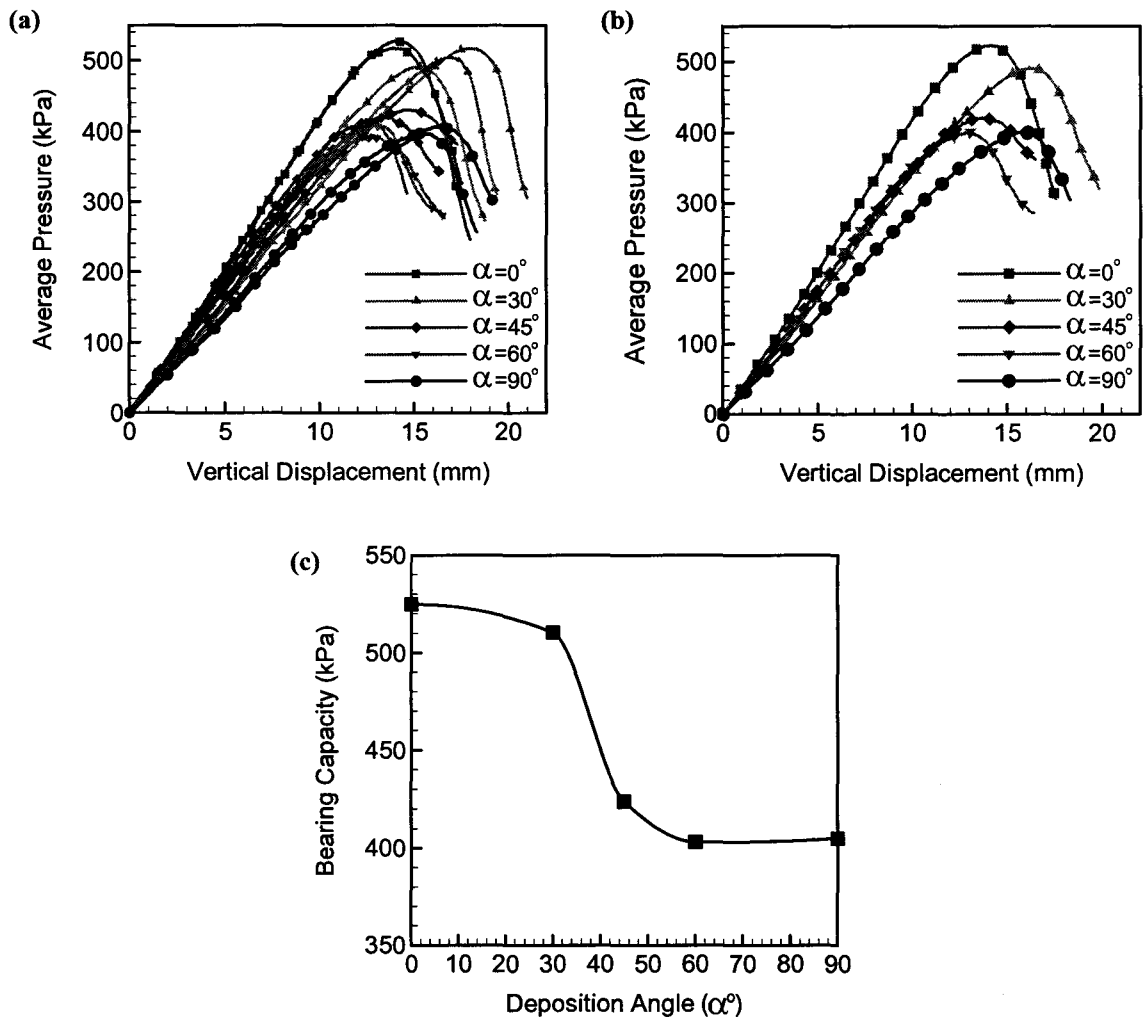

Fig 2-22 Results of scaled footing tests: (a) load-displacement response for different values of α, (b) averaged characteristics, (c) variation of the bearing capacity with the deposition angle α

CHAPTER 3
MATHEMATICAL FORMULATION

3.1 Introduction

In this section, the mathematical formulation of the constitutive model is discussed. The approach presented here is able to simulate complex nonlinear behavior of geomaterials with inherent anisotropy. A general framework is also outlined to identify the onset of localization and to deal with post localization behavior.

3.2 Elastoplastic Constitutive Equations (General Overview)

In the framework of classical plasticity there are two basic functions or surfaces that are defined in the stress space, i.e. "*yield surface*" and "*plastic potential*" (e.g., Owen and Hinton 1980, Simo and Hughes 1998). These two functions are used in the derivation of stress-strain relations (constitutive equations) of the materials.

Based on experimental evidence, plasticity theory postulates that irreversible or plastic strains occur whenever the stress state satisfies the yield criterion

$$F(\sigma_{ij}, \kappa) = 0 \tag{3.1}$$

where σ_{ij} is the stress tensor and κ is the material state (hardening) parameter. In the framework of plasticity, following the observation on the plastic flow of metals, it is

assumed that the plastic strain increments ($\dot{\varepsilon}_{ij}^{p}$) are coaxial with the gradient of plastic potential function Q

$$Q(\sigma_{ij}) = const. \quad , \quad \dot{\varepsilon}_{ij}^{p} = \dot{\lambda}\frac{\partial Q}{\partial \sigma_{ij}} \tag{3.2}$$

where $\dot{\lambda}$ is the plastic multiplier and eq. (3.2) is referred to as the flow rule.

Constitutive relation is the mathematical description of the relationship between the states of stress and strain. Since the behavior of geomaterials is nonlinear, that relation is defined in an incremental form as follow

$$\dot{\sigma}_{ij} = D_{ijkl}^{ep}\dot{\varepsilon}_{kl} \tag{3.3}$$

In (3.3) $\dot{\sigma}_{ij}$ is the incremental stress tensor, $\dot{\varepsilon}_{kl}$ is the incremental strain tensor and D_{ijkl}^{ep} is the 4th order elasto-plastic constitutive tensor. The operator D_{ijkl}^{ep} is derived by invoking the consistency condition, Hooke's law, additivity postulate, and the flow rule, i.e.

$$\dot{F} = \frac{\partial F}{\partial \sigma_{ij}}\dot{\sigma}_{ij} + \frac{\partial F}{\partial \kappa}\dot{\kappa} = 0 \tag{3.4}$$

$$\dot{\sigma}_{ij} = D_{ijkl}^{e}\dot{\varepsilon}_{kl}^{e} \tag{3.5}$$

$$\dot{\varepsilon}_{kl} = \dot{\varepsilon}_{kl}^{e} + \dot{\varepsilon}_{kl}^{p} \tag{3.6}$$

$$\dot{\varepsilon}_{kl}^{p} = \dot{\lambda}\frac{\partial Q}{\partial \sigma_{kl}} \tag{3.7}$$

where D^e_{ijkl} is the elastic constitutive matrix.

Substituting $\dot{\sigma}_{ij}$ from eq. (3.5) into eq. (3.4), and considering the additivity postulate leads to

$$\dot{F} = \frac{\partial F}{\partial \sigma_{ij}} D^e_{ijkl}(\dot{\varepsilon}_{kl} - \dot{\varepsilon}^p_{kl}) + \frac{\partial F}{\partial \kappa}\frac{\partial \kappa}{\partial \varepsilon^p_{ij}}\dot{\varepsilon}^p_{ij} = 0 \tag{3.8}$$

Introducing now the flow rule in (3.7), the above equation can be rewritten as

$$\dot{F} = \frac{\partial F}{\partial \sigma_{ij}} D^e_{ijkl}(\dot{\varepsilon}_{kl} - \dot{\lambda}\frac{\partial Q}{\partial \sigma_{kl}}) + \dot{\lambda}\frac{\partial F}{\partial \kappa}\frac{\partial \kappa}{\partial \varepsilon^p_{ij}}\frac{\partial Q}{\partial \sigma_{ij}} = 0 \tag{3.9}$$

So that the plastic multiplier can be determined as

$$\dot{\lambda} = \frac{\dfrac{\partial F}{\partial \sigma_{ij}} D^e_{ijkl}\dot{\varepsilon}_{kl}}{\dfrac{\partial F}{\partial \sigma_{ij}} D^e_{ijkl}\dfrac{\partial Q}{\partial \sigma_{kl}} + H^p} \quad , \quad H^p = -\frac{\partial F}{\partial \kappa}\frac{\partial \kappa}{\partial \varepsilon^p_{ij}}\frac{\partial Q}{\partial \sigma_{ij}} \tag{3.10}$$

In the equation above, H^p is the so called plastic hardening modulus. Substituting now eq. (3.10) into eq. (3.7) and invoking the Hook's law (3.5) yields

$$\begin{aligned}\dot{\sigma}_{ij} &= D^e_{ijkl}\dot{\varepsilon}^e_{kl} = D^e_{ijkl}(\dot{\varepsilon}_{kl} - \dot{\varepsilon}^p_{kl}) = D^e_{ijkl}\left(\dot{\varepsilon}_{kl} - \dot{\lambda}\frac{\partial Q}{\partial \sigma_{kl}}\right) \\ &= D^e_{ijkl}\left(\dot{\varepsilon}_{kl} - \frac{\dfrac{\partial F}{\partial \sigma_{mn}} D^e_{mnkl}\dot{\varepsilon}_{kl}}{\dfrac{\partial F}{\partial \sigma_{mn}} D^e_{mnpq}\dfrac{\partial Q}{\partial \sigma_{pq}} + H^p}\frac{\partial Q}{\partial \sigma_{kl}}\right) = \left(D^e_{ijkl} - \frac{D^e_{ijpq}\dfrac{\partial Q}{\partial \sigma_{pq}}\dfrac{\partial F}{\partial \sigma_{mn}} D^e_{mnkl}}{\dfrac{\partial F}{\partial \sigma_{mn}} D^e_{mnpq}\dfrac{\partial Q}{\partial \sigma_{pq}} + H^p}\right)\dot{\varepsilon}_{kl}\end{aligned} \tag{3.11}$$

Thus comparing eq. (3.11) with the functional form (3.3), the elasto-plastic constitutive tensor can be expressed as

$$D^{ep}_{ijkl} = D^{e}_{ijkl} - \frac{D^{e}_{ijpq}\dfrac{\partial Q}{\partial \sigma_{pq}}\dfrac{\partial F}{\partial \sigma_{mn}}D^{e}_{mnkl}}{\dfrac{\partial F}{\partial \sigma_{mn}}D^{e}_{mnpq}\dfrac{\partial Q}{\partial \sigma_{pq}} + H^{p}} \tag{3.12}$$

If the material is isotropic, the representation theorems of scalar function of tensor variable allow to express the yield function in terms of stress invariants

$$F(J_1, J_2, J_3, \kappa) = 0 \quad , \quad F(J_1, J_{2D}, J_{3D}, \kappa) = 0 \quad , \quad F(p, q, \theta, \kappa) = 0 \tag{3.13}$$

where the stress invariants are defined as follow

$$J_1 = 3p = \sigma_{ii}$$

$$J_2 = \frac{1}{2}\left(\sigma_{ii}\sigma_{jj} - \sigma_{ij}\sigma_{ji}\right) \;;\; J_{2D} = \frac{1}{2}s_{ij}s_{ij} \;;\; q = \sqrt{3J_{2D}} \tag{3.14}$$

$$J_3 = \frac{1}{3}\sigma_{ij}\sigma_{jk}\sigma_{ki} \;;\; J_{3D} = \frac{1}{3}s_{ij}s_{jk}s_{ki} \;;\; \theta = \frac{1}{3}\sin^{-1}\left(-\frac{3\sqrt{3}}{2}\frac{J_{3D}}{\left(J_{2D}\right)^{3/2}}\right) \quad -\frac{\pi}{6} \le \theta \le \frac{\pi}{6}$$

In equations above s_{ij} is the stress deviator defined as $s_{ij} = \sigma_{ij} - \delta_{ij}p$, δ_{ij} is the Kronecher's delta and θ is the Lode's angle.

The strain tensor has also some commonly used invariants. The work conjugates of the stress invariants (p,q) , i.e. volumetric and deviatoric strains $(\varepsilon_v,\varepsilon_q)$, are defined as follow:

$$\varepsilon_v = \varepsilon_{ii}$$

$$e_{ij} = \varepsilon_{ij} - \frac{1}{3}\delta_{ij}\varepsilon_v \quad , \quad \varepsilon_q = \frac{2}{\sqrt{3}}\sqrt{\bar{\varepsilon}} = \frac{2}{\sqrt{3}}\sqrt{\frac{1}{2}e_{ij}e_{ij}} \tag{3.15}$$

where

$$\dot{W} = \sigma_{ij}\dot{\varepsilon}_{ij} = p\dot{\varepsilon}_v + q\dot{\varepsilon}_q \tag{3.16}$$

Finally, the derivatives of the stress invariants with respect to stress components have some applications in the elastoplastic constitutive modeling. These derivatives can be calculated as follows

$$\frac{\partial J_1}{\partial \sigma_{ij}} = \frac{\partial \sigma_{mm}}{\partial \sigma_{ij}} = \delta_{im}\delta_{jm} = \delta_{ij} \quad , \quad \frac{\partial p}{\partial \sigma_{ij}} = \frac{1}{3}\frac{\partial J_1}{\partial \sigma_{ij}} = \frac{1}{3}\delta_{ij} \tag{3.17}$$

$$\frac{\partial J_{2D}}{\partial \sigma_{ij}} = s_{ij} \quad , \quad \frac{\partial q}{\partial \sigma_{ij}} = \frac{\sqrt{3}}{2\sqrt{J_{2D}}}\frac{\partial J_{2D}}{\partial \sigma_{ij}} = \frac{3}{q}s_{ij} \tag{3.18}$$

$$\frac{\partial J_{3D}}{\partial \sigma_{ij}} = s_{ki}s_{jk} - \frac{2}{3}\delta_{ij}J_{2D} \quad , \quad \frac{\partial \theta}{\partial \sigma_{ij}} = \frac{\sqrt{3}}{2\sqrt{J_2}^3\cos 3\theta}\left(\frac{3J_3}{2J_2}s_{ij} - s_{ik}s_{kj} + \frac{2}{3}J_2\delta_{ij}\right) \tag{3.19}$$

3.3 A Multi-Surface Plasticity Model

The constitutive framework presented here is based on multi-yield loci plasticity and accounts for the salient features that include the notions of compaction/dilation, pressure sensitivity and hardening induced by both densification and plastic distortion. In what follows, the basic framework will be outlined first. In the next two sections, an extension to anisotropy and post localization regime will be discussed. Later, in Chapter 5, a discussion on the numerical integration scheme will be provided.

Three basic mechanisms are considered in this model, viz. deviatoric hardening, volumetric hardening and a tension cutoff. The yield surface and hardening characteristics of the volumetric and deviatoric hardening mechanisms are shown in Fig 3-1a and Fig 3-1b. The elastic domain, i.e. the region inside the domain enclosed by the yield surfaces, is illustrated in Fig 3-1c. The yield surfaces, plastic potentials and hardening rules of the three mechanisms are defined as

$$F_1 = \frac{q}{g(\theta)} - \eta(p+C) = 0, \quad \eta(\varepsilon_q^p) = \eta_f \frac{\left(\varepsilon_q^p\right)_1}{B + \left(\varepsilon_q^p\right)_1}$$

$$Q_1 = \frac{q}{g(\theta)} + \eta_c (p+C) \ln\left(\frac{p+C}{p_0}\right) = const., \tag{3.20}$$

$$F_2 = \left(\frac{q}{g(\theta)\eta_f}\right)^2 + (p - p_c)(p+C) = 0,$$

$$p_c = p_0 e^{-\left(\varepsilon^p\right)_2/(\lambda-\kappa)}, \quad \left(\dot{e}^p\right)_2 = -(1+e_0)\left(\dot{\varepsilon}_v^p\right)_2 \tag{3.21}$$

$$F_3 = T - p = 0 \tag{3.22}$$

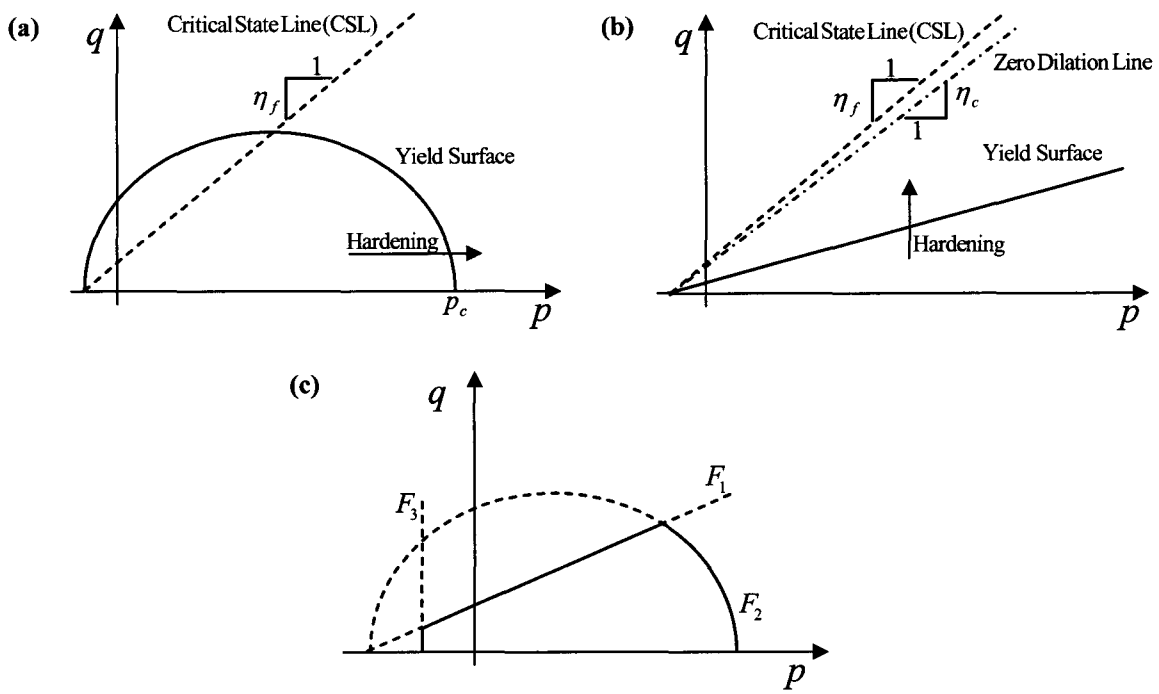

Fig 3-1 Yield surfaces of the proposed multimechanism model, (a) volumetric mechanism, (b) deviatoric mechanism and c) the elastic domain confined inside the three yield surfaces

In the expressions above, $(\eta_f, C, \eta_c, B)_1$, $(\eta_f, C, \lambda, \kappa, e_0)_2$ and $(T)_3$ are the material parameters for deviatoric, volumetric and tension cut off mechanism, respectively. The function $g(\theta)$ satisfies $g(\pi/6) = 1$ and $g(-\pi/6) = K$, where K is a constant.

The proposed multimechanism model is simply formed by combining well established individual mechanisms. The volumetric hardening is essentially the modified Cam-Clay model. In the deviatoric hardening mechanism, if the conditions at failure are assumed to be consistent with Mohr-Coulomb criterion, then the basic material parameters become $\eta_f = 6\sin\phi/(3-\sin\phi)$, $C = c\cot\phi$; where ϕ and c are the angle of friction and cohesion, respectively. The function $g(\theta)$ is selected so that to provide a smooth approximation to Mohr-Coulomb irregular hexagonal cross-section in the

octahedral plane (see Fig 3-2). In particular, the form given by Jiang and Pietruszczak (1988) is employed

$$g(\theta)=\frac{\left(\sqrt{1+a}-\sqrt{1-a}\right)K}{K\sqrt{1+a}-\sqrt{1-a}+(1-K)\sqrt{1+a\cos 3\theta}},\quad a\to 1 \tag{3.23}$$

where a is a constant. Note that the sufficient condition for convexity is $K\geq\left(7a-2(1-\sqrt{1-a^2})\right)/9a$. Thus, for $a=0.9999$ for example, there is $K\geq 0.5587$, which corresponds to $\varphi\leq 58.15^{o}$.

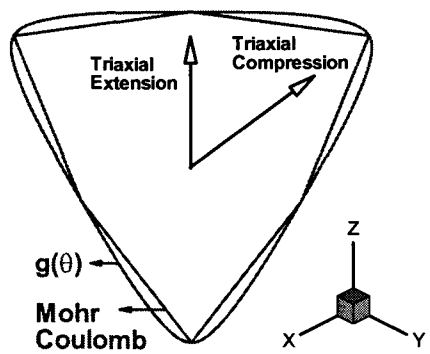

Fig 3-2 Projection of normalized Mohr-coulomb yield surface and the function $g(\theta)$ on the π plane (normal to the stress space diagonal)

In the deviatoric mechanism, which has a nonassociated flow rule, η_f is the ultimate stress ratio, C is the hydrostatic tension resistance, B is a material parameter that controls the hardening behavior, and η_c is the stress ratio beyond which the volumetric behavior of material switches from compaction to dilation. By implementing an associated flow rule in the volumetric hardening mechanism, η_f also marks the critical state, similar to the modified Cam-Clay model. Here λ and κ are the slopes of loading/unloading branches of the relation between void ration (e) and natural logarithm

of p. For the tension cut off, T is the hydrostatic tension resistance, which should be less than C for this mechanism to be activated.

The hardening effects are attributed to accumulated deviatoric plastic strain for the deviatoric mechanism, and to accumulated volumetric plastic strain for the volumetric mechanism. The hardening rules are not coupled, e.g. the volumetric plastic strain generated by the deviatoric mechanism does not contribute to the hardening associated with the volumetric mechanism, and vice versa.

When the stress state is at the intersection of two yield surfaces the elastoplastic constitutive operator (D^{ep}_{ijkl}) can be calculated based on Koiter's postulate. The consistency conditions, Hooke's law and the respective flow rules are used in the derivation of the constitutive tensor (Pasternack and Timmerman 1986). Note that in the case of multimechanism plasticity the consistency condition should be satisfied for all the active yield surfaces contributing to the plastic flow, i.e. $\dot{F}_1 = \dot{F}_2 = 0$. The constitutive tensor for case of two active mechanisms can be calculated as

$$D^{ep}_{ijkl} = D^{e}_{ijkl} - \frac{D^{e}_{ijkl}\dfrac{\partial Q_1}{\partial \sigma_{kl}}\left(N_1\right)_{ij} D^{e}_{ijkl}}{H^{ep}} - \frac{D^{e}_{ijkl}\dfrac{\partial Q_2}{\partial \sigma_{kl}}\left(N_2\right)_{ij} D^{e}_{ijkl}}{H^{ep}} \tag{3.24}$$

where

$$H^{p}_{\beta} = -\frac{\partial F_\beta}{\partial \kappa_\beta}\frac{\dot{\kappa}_\beta}{\dot{\lambda}_\beta} \quad ; \quad H^{e}_{\beta\gamma} = \frac{\partial F_\beta}{\partial \sigma_{ij}} D^{e}_{ijkl}\frac{\partial Q_\gamma}{\partial \sigma_{kl}} \tag{3.25}$$

$$\left(N_\beta\right)_{ij} = \left(H^{e}_{\gamma\gamma} + H^{p}_{\gamma}\right)\frac{\partial F_\beta}{\partial \sigma_{ij}} - H^{e}_{\beta\gamma}\frac{\partial F_\gamma}{\partial \sigma_{ij}} \quad ; \quad \beta,\gamma = 1,2$$

Details of the derivation of eq. (3.24) are presented in Appendix I.

3.4 Inherent Anisotropy

The modeling of mechanical response of anisotropic materials is typically based on the notion of a continuum with microstructure and requires the introduction of a tensorial measure that describes the anisotropy. The available methodologies are essentially based on the representation theorems of scalar functions of tensor variables. The most common is the approach presented by Boehler and Sawczuk (1977) and Boehler (1987), which is mathematically rigorous but, at the same time, very complex as it employs ten independent basic and mixed invariants of both the stress and fabric tensors. Simplified versions are also difficult in implementation as they still incorporate an excessive number of material functions/parameters. Cowin (1987), for example, developed a quadratic approximation to the failure function in terms of components of σ_{ij}. However, even such a simple representation employs 12 functions of material fabric, which cannot be easily identified from standard experiments. In the simplified approach presented by Oka et al. (2002), a transformed state of stress is defined based on the real state of stress and the microstructure tensor. The applied transformation functions are rather vague and the identification of material parameters is not very clear. A different approach has been proposed by Pietruszczak and Mroz (2001) and Pietruszczak et al. (2002), in which the effects of anisotropy are considered in the material parameters, i.e. the material properties are considered to be directionaly-dependent.

3.4.1 Conditions at Failure for Anisotropic Materials (Critical Plane Approach)

An extensive review and assessment of various failure criteria for anisotropic materials can be found, for example, in the work by Duveau et al. (1998). The specification of conditions at failure for anisotropic materials constitutes an important problem which has attracted the attention of numerous researchers. One of the approaches to formulate failure criteria is to invoke linear as well as quadratic terms of stress components referred to the coordinate system associated with the axes of symmetry of the material. An example of such an approach is an extension of the well-known Hill's criterion (Hill 1950), as proposed by Tsai and Wu (1971). Mathematically rigorous approaches, which make use of general representation theorems, were first proposed by Boehler and Sawczuk (1970) and later were extended by others, e.g. Nova (1980). The problem was also formulated by invoking the notion of a fabric tensor specifying the directional distribution of lineal/areal porosity (Pietruszczak 1999).

The other group of failure criteria was derived by adopting the weakness plane approach. This approach requires the failure condition to be satisfied on a predefined discrete weakness plane, e.g. Walsh and Brace (1964), Hoek and Brown (1980), Hoek (1983).

The disadvantage of most of these phenomenological formulations stems from the fact that they employ numerous material parameters or functions. Their relation to material microstructure is not explicitly defined and the identification procedure requires an extensive experimental program.

The method applied in this research is based on the critical plane approach presented by Pietruszczak and Mroz (2001) and Pietruszczak and Pande (2001). The method consists of identifying the orientation of the critical/localization plane on which the failure function reaches maximum. Assume that for a cohesive-frictional material the conditions at failure are defined in terms of Coulomb's linear form

$$F = \tau - \mu\sigma - c = 0; \quad \mu = \mu(n_i), \; c = c(n_i) \tag{3.26}$$

In above $\mu = \tan(\phi)$ and c (cohesion) are both said to be orientation dependent and τ, σ represent the shear and normal components of the traction vector on an arbitrary plane with unit normal n_i

$$\sigma = \sigma_{ij} n_i n_j \; ; \quad \tau = \sigma_{ij} n_i s_j \tag{3.27}$$

$$s_i = \frac{T_i^s}{\left|T_i^s\right|} \; ; \quad T_i^s = (\delta_{ij} - n_i n_j)\sigma_{jk} n_k \tag{3.28}$$

The distribution of strength parameters can be defined based on the results of direct shear tests. Let the distribution of $\mu = \tan\phi$ be described by

$$\mu = \hat{\mu}\left(1 + \Omega_{ij} n_i n_j + b_1(\Omega_{ij} n_i n_j)^2 + b_2(\Omega_{ij} n_i n_j)^3 + b_3(\Omega_{ij} n_i n_j)^4 + ...\right) \tag{3.29}$$

where Ω_{ij} is a traceless symmetric tensor.

Referring the problem to the principal material system and assuming that $\hat{x}_3$-axis is normal to the bedding planes (plane of isotropy), so that $\hat{\mathbf{e}}_3 = (0, \sin\alpha, \cos\alpha)$, there is

$$\Omega_1 = \Omega_2; \quad \Omega_1 + \Omega_2 + \Omega_3 = 0; \qquad \Omega_{ij} n_i n_j = \Omega_1 (1 - 3\cos^2\alpha) \tag{3.30}$$

so that

$$\mu = \hat{\mu}\left(1 + \Omega_1(1 - 3\cos^2\alpha) + b_1\Omega_1^2(1 - 3\cos^2\alpha)^2 + b_2\Omega_1^3(1 - 3\cos^2\alpha)^3 + ...\right) \tag{3.31}$$

A similar methodology may be applied to describe the bias in the spatial variation of cohesion c.

The framework outlined above can be employed to define the conditions at failure for an arbitrary stress state at a material point. The general criterion, under 3D stress condition represents a constrained optimization problem

$$F = \underbrace{\max}_{n_i}\left(\tau - \mu\sigma - c\right) = 0; \quad \mu = \mu(n_i),\ c = c(n_i),\ n_i n_i = 1 \tag{3.32}$$

which can be solved by Lagrange multipliers or any other known technique (e.g. interior point method, Renegar 2001).

3.4.2 Mechanical Behavior of Anisotropic Material

The general formulation to simulate the mechanical behavior of transversally isotropic material is presented in this section. Anisotropy is considered for the material both in elastic and plastic ranges of deformation.

3.4.2.1 Anisotropy in Elastic Behavior

Consider an arbitrary coordinate system with base vectors $(\mathbf{e}_1, \mathbf{e}_2, \mathbf{e}_3)$, and let the material coordinate system be defined by the normal basis $(\hat{\mathbf{e}}_1, \hat{\mathbf{e}}_2, \hat{\mathbf{e}}_3)$ with $\hat{\mathbf{e}}_3$ being the vector normal to the bedding plane (plane of isotropy). The relation between the stress tensor in the material and the global systems is

$$\hat{\sigma}_{pq} = R_{pi}\sigma_{ij}R_{qj} \tag{3.33}$$

where R_{ij} is the transformation tensor whose components are the direction cosines of the material triads.

In the elastic range, for a transversally isotropic material, the constitutive equation in the material coordinate system can be formulated in terms of 5 independent elastic parameters, $E_1, E_3, \nu_{12}, \nu_{13}, G_{13}$ (e.g. Timoshenko and Goodier 1970, Saada 1993)

$$\hat{\sigma}_{ij} = \hat{D}^e_{ijkl}\hat{\varepsilon}_{kl} \tag{3.34}$$

The components of the elastic constitutive tensor are

$$
\begin{aligned}
&\hat{D}^e_{1111} = \hat{D}^e_{2222} = E_1(1-\nu_{31}\nu_{13})\Upsilon \\
&\hat{D}^e_{3333} = E_3(1-\nu_{12}^2)\Upsilon \\
&\hat{D}^e_{1122} = \hat{D}^e_{2211} = E_1(\nu_1+\nu_{31}\nu_{13})\Upsilon \\
&\hat{D}^e_{1133} = \hat{D}^e_{3311} = \hat{D}^e_{2233} = \hat{D}^e_{3322} = E_1(\nu_{31}+\nu_{31}\nu_{12})\Upsilon = E_3(\nu_{13}+\nu_{13}\nu_{12})\Upsilon \\
&\hat{D}^e_{1212} = \hat{D}^e_{2121} = \hat{D}^e_{1221} = \hat{D}^e_{2112} = G_{12} \\
&\hat{D}^e_{1313} = \hat{D}^e_{3131} = \hat{D}^e_{1331} = \hat{D}^e_{3113} = G_{13} \\
&\hat{D}^e_{2323} = \hat{D}^e_{3232} = \hat{D}^e_{2332} = \hat{D}^e_{3223} = G_{13}
\end{aligned}
\tag{3.35}
$$

where

$$
\begin{aligned}
&\Upsilon = (1-\nu_{12}^2-2\nu_{13}\nu_{31}-2\nu_{12}\nu_{13}\nu_{31})^{-1} \\
&G_{12} = \frac{1}{2}\left(D_{1111}-D_{1122}\right) = \frac{E_1}{2(1+\nu_{12})} \\
&E_1\nu_{31} = E_3\nu_{13}
\end{aligned}
\tag{3.36}
$$

In above equations, the shear strains are the tensorial strains (ε_{ij} ; $i \neq j$). The transformation rule from the material to the global coordinate system takes the form

$$
\hat{\sigma}_{pq} = R_{pi}\sigma_{ij}R_{qj} \;\;,\;\; \sigma_{ij} = R_{pi}\hat{\sigma}_{pq}R_{qj} \;\;,\;\; \hat{\varepsilon}_{st} = R_{sk}\varepsilon_{kl}R_{tl} \tag{3.37}
$$

so that

$$
\sigma_{ij} = D^e_{ijkl}\varepsilon_{kl} \;\Rightarrow\; D^e_{ijkl} = R_{pi}R_{qj}\hat{D}^e_{pqst}R_{sk}R_{tl} \tag{3.38}
$$

3.4.2.2 Anisotropy in Plastic Behavior

In order to consider anisotropy in the plastic behavior some modifications should be introduced in the definition of basic functions that are involved in the formulation of the problem, i.e. the yield surface and plastic potential functions, the hardening rule, etc.

As mentioned earlier, the modeling of the mechanical response of anisotropic

materials is typically based on the notion of a continuum with microstructure and requires the introduction of a tensorial measure that describes the anisotropy. In this work, the approach proposed by Pietruszczak and Mroz (2001) and Pietruszczak et al. (2002) is adopted, in which the effects of anisotropy are attributed to variation of material properties. In general, the material parameters are assumed to depend on the orientation of material axes relative to the principal stress system. Using the framework outlined in the article by Pietruszczak and Mroz (2001), the following representation is employed

$$\Psi = \bar{\Psi}(1+\xi+\psi_1\xi^2+\psi_2\xi^3+\psi_3\xi^4+...) \;\; , \;\; \xi = A_{ij}l_i l_j = \frac{A_{ik}\sigma_{ij}\sigma_{kj}}{\sigma_{pq}\sigma_{pq}} \tag{3.39}$$

Here Ψ represents any material parameter that is orientation-dependent, A_{ij} is a deviatoric part of a symmetric second order microstructure tensor whose eigenvectors are co-linear with preferred material directions, while l_i is the so-called *loading direction*. The latter can be defined as

$$l_i = \frac{L_i}{(L_k L_k)^{1/2}} \;\; ; \;\; L_i = L_1 e_i^{(1)} + L_2 e_i^{(2)} + L_3 e_i^{(3)} \tag{3.40}$$

where the components of L_i represent the traction moduli on the planes normal to the principal material axes $e_i^{(\alpha)}, \alpha = 1,2,3$, i.e.

$$L_1^2 = e_i^{(1)} e_k^{(1)} \sigma_{ij}\sigma_{kj} \;\; , \;\; L_2^2 = e_i^{(2)} e_k^{(2)} \sigma_{ij}\sigma_{kj} \;\; , \;\; L_3^2 = e_i^{(3)} e_k^{(3)} \sigma_{ij}\sigma_{kj} \tag{3.41}$$

The above formulation can be applied to incorporate the anisotropic effects in any constitutive model. For the model presented in this thesis, orientation dependency of η_f and T introduces the strength anisotropy while the orientation-dependency of (η_c, B) enables to capture the anisotropy in the deformation characteristics of the material. In view of (3.39) and the definition of ξ, it is worth to mention that the anisotropic effects in the mathematical formulation are more pronounced at lower level of stress, and tend to fade as the level of stress increases. A similar pattern was observed and pointed out in the experimental data obtained in triaxial tests (see Fig. 2-12 to Fig. 2-15).

When deriving the elastoplastic constitutive equations, the expression for the gradient of yield/plastic potential functions needs to be modified to

$$\frac{\partial F}{\partial \sigma_{ij}} = \left(\frac{\partial F}{\partial p}\frac{\partial p}{\partial \sigma_{ij}} + \frac{\partial F}{\partial \bar{\sigma}}\frac{\partial q}{\partial \sigma_{ij}} + \frac{\partial F}{\partial \theta}\frac{\partial \theta}{\partial \sigma_{ij}} \right) + \left(\frac{\partial F}{\partial \Psi}\frac{\partial \Psi}{\partial \sigma_{ij}} \right) \tag{3.42}$$

In (3.42), the first term in the parenthesis is a standard one in classical elasto-plasticity, while the second term is the contribution of the anisotropy. The derivative of Ψ becomes

$$\frac{\partial \Psi}{\partial \sigma_{ij}} = \frac{\partial \Psi}{\partial \xi}\frac{\partial \xi}{\partial \sigma_{ij}} = 2\bar{\Psi}(1 + 2\psi_1 \xi + 3\psi_2 \xi^2 + \ldots)\frac{A_{ki}\sigma_{kj}\sigma_{pq}\sigma_{pq} - A_{pk}\sigma_{pq}\sigma_{kq}\sigma_{ij}}{(\sigma_{mn}\sigma_{mn})^2} \tag{3.43}$$

These derivatives should be considered in the integration of the elastoplastic constitutive equation as well as the calculation of the gradient operator.

3.5 Strain Localization

In this section the kinematics of strong discontinuity is discussed first. Later, the formulation is applied to bifurcation analysis to determine the onset of discontinuity. The section is concluded by examining the formulation describing the propagation of strain localization.

3.5.1 Kinematics of Strong Discontinuities

Consider a body Ω under a displacement field $\mathbf{u}(\mathbf{x})$. Furthermore, focus on the case when localization occurs that is associated with formation of an internal surface δ in Ω with bandwidth h and the normal vector $\mathbf{n}$. It is assumed that a discontinuity in the displacement field starts to develop along the internal surface δ. This surface divides the body into the sub domains Ω^+ and Ω^- as shown in Fig 3-3. The rate of displacement field at time t, $\dot{\mathbf{u}}(\mathbf{x},t)$, can be expressed as (Simo et al. 1993, Oliver 1995, Oliver et al. 1999, Oliver and Huespe 2004):

$$\dot{u}_k(\mathbf{x},t) = \dot{\bar{u}}_k(\mathbf{x},t) + H_{\Omega|\delta}(\mathbf{x},t)[\![\dot{u}]\!]_k(\mathbf{x},t) \tag{3.44}$$

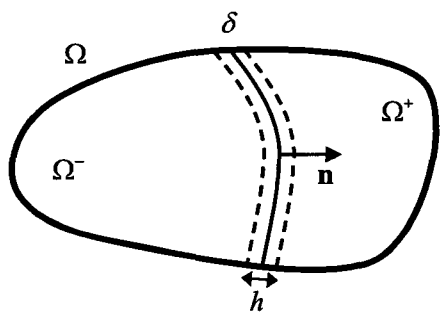

Fig 3-3 Body Ω with discontinuity surface δ

In eq. (3.44) $\dot{\bar{\mathbf{u}}}$ is a continuous rate of displacement field, and $[\![\dot{\mathbf{u}}]\!]$ is the displacement jump across δ from Ω^- to Ω^+, and $H_{\Omega|\delta}$ is the unit jump function

$$H_{\Omega|\delta}(\mathbf{x},t)=\begin{cases}0 & \mathbf{x}\in\Omega^- \\ 1 & \mathbf{x}\in\Omega^-\end{cases} \tag{3.45}$$

Assuming small deformations, the strain field can be calculated by applying the proper spatial derivative operator on (3.44),

$$\dot{\varepsilon}_{kl}=\frac{1}{2}(\dot{u}_{k,l}+\dot{u}_{l,k})=\underbrace{\frac{1}{2}(\dot{\bar{u}}_{k,l}+\dot{\bar{u}}_{l,k})+\frac{1}{2}H_{\Omega|\delta}([\![\dot{u}]\!]_{k,l}+[\![\dot{u}]\!]_{l,k})}_{\dot{\bar{\varepsilon}}_{kl}}+\underbrace{\frac{\mu_\delta}{h}[\![\dot{u}]\!]_k n_l}_{[\![\dot{\varepsilon}]\!]_{kl}} \tag{3.46}$$

where μ_δ is the collocation function placed at δ:

$$\mu_\delta(\mathbf{x},t)=\begin{cases}0 & \mathbf{x}\notin\delta \\ 1 & \mathbf{x}\in\delta\end{cases} \tag{3.47}$$

Note that depending on the value of h, i.e. the bandwidth of the discontinuity plane, the kinematics of discontinuity described in (3.44) and (3.46) can imply different kinds of discontinuity.

3.5.2 Onset of Strain Localization; Bifurcation

The inception of strain localization and formation of a shear band is commonly considered as a bifurcation problem, i.e. loss of uniqueness of solution to the set of equations governing incremental equilibrium which admits an alternative deformation mode associated with formation of a shear band (Rudnicki and Rice 1975, Pietruszczak

and Niu 1993, Vardoulakis and Sulem 1995).

Given the kinematics of discontinuity as discussed in the previous subsection, the problem can be stated as follows: find the conditions under which the strain field, continuous in a neighborhood of a material point P on the discontinuity surface δ, bifurcates into discontinuous field

$$P \in \delta, \underbrace{\left[(\sigma_{ij})_{\Omega\setminus\delta} = (\sigma_{ij})_{\delta}\,,\ (\varepsilon_{kl})_{\Omega\setminus\delta} = (\varepsilon_{kl})_{\delta}\right]}_{\text{continuous}} \rightarrow \underbrace{\left((\dot{\varepsilon}_{kl})_{\Omega\setminus\delta} = \dot{\bar{\varepsilon}}_{kl}\,,\ (\dot{\varepsilon}_{kl})_{\delta} = \dot{\bar{\varepsilon}}_{kl} + \frac{1}{h}(\llbracket \dot{u} \rrbracket_k\, n_l)_{\delta}\right)}_{\text{discontinuous}} \tag{3.48}$$

such that the traction remains continuous across the discontinuity

$$n_i(\sigma_{ij})_{\Omega\setminus\delta} = n_i(\sigma_{ij})_{\delta} \tag{3.49}$$

Given the constitutive equations

$$\begin{aligned} (\dot{\sigma}_{ij})_{\Omega/\delta} &= (D_{ijkl})_{\Omega\setminus\delta}\,\dot{\bar{\varepsilon}}_{kl} \\ (\dot{\sigma}_{ij})_{\delta} &= (D_{ijkl})_{\delta}\left(\dot{\bar{\varepsilon}}_{kl} + \frac{1}{h}(\llbracket \dot{u} \rrbracket_k\, n_l)_{\delta}\right) \end{aligned} \tag{3.50}$$

and substituting (3.50) into (3.49) leads to

$$\begin{aligned} n_i(D_{ijkl})_{\Omega\setminus\delta}\,\dot{\bar{\varepsilon}}_{kl} &= n_i(D_{ijkl})_{\delta}\left(\dot{\bar{\varepsilon}}_{kl} + \frac{1}{h}(\llbracket \dot{u} \rrbracket_k\, n_l)_{\delta}\right) \\ \underbrace{\left(n_i(D_{ijkl})_{\delta}\, n_l\right)}_{Q_{jk}} \llbracket \dot{u} \rrbracket_k &= h n_i\left((D_{ijkl})_{\Omega\setminus\delta} - (D_{ijkl})_{\delta}\right)\dot{\bar{\varepsilon}}_{kl} \end{aligned} \tag{3.51}$$

where $\mathbf{Q}$ is the acoustic (or localization) tensor.

In view of equation (3.51) different mechanisms for the onset of bifurcation can be considered (Runesson et al. 1991 , Oliver et al. 1999):

1- The stress state is in the elastic range, both at the discontinuity surface and its neighborhood, i.e. $\mathbf{D}_{\Omega\setminus\delta} = \mathbf{D}_{\delta} = \mathbf{D}^{e}$. In this case, the right hand side of (3.51) will be zero and the equation simplifies to $Q^{e}_{jk}[\![\dot{u}]\!]_{k} = 0_{j}$. Here, $\mathbf{Q}^{e}$ is the elastic acoustic tensor which is shown to be non singular and positive definite, $\det(\mathbf{Q}^{e}) > 0$, and all the eigenvalues of $\mathbf{Q}^{e}$ are positive. Therefore, $[\![\dot{\mathbf{u}}]\!] = 0$ and bifurcation is precluded.

2- The stress state is in the elastoplastic range, both at the discontinuity surface and its neighborhood, i.e. $\mathbf{D}_{\Omega\setminus\delta} = \mathbf{D}_{\delta} = \mathbf{D}^{ep}$. In this case again, the right hand side of (3.51) will be zero and the equation simplifies to $Q^{ep}_{jk}[\![\dot{u}]\!]_{k} = 0_{j}$. To have $[\![\dot{\mathbf{u}}]\!] \neq 0$, the operator $\mathbf{Q}^{ep}$ should be singular with at least one zero eigenvalue, i.e.

$$\det(\mathbf{Q}^{ep}) = \det\left(n_i D^{ep}_{ijkl} n_l\right) = 0 \tag{3.52}$$

3- The stress state is in the elastoplastic range at the discontinuity surface and in the elastic range in its neighborhood, i.e. $\mathbf{D}_{\Omega/\delta} = \mathbf{D}^{ep}$, $\mathbf{D}_{\delta} = \mathbf{D}^{ep}$. In this case (3.51) can be rewritten as

$$\begin{aligned}\underbrace{\left(n_i D^{ep}_{ijkl} n_l\right)}_{Q_{jk}}[\![\dot{u}]\!]_{k} &= h n_i \left(D^{e}_{ijkl} - D^{ep}_{ijkl}\right)\dot{\bar{\varepsilon}}_{kl} = h n_i \left(\frac{D^{e}_{ijkl}\dfrac{\partial Q}{\partial \sigma_{kl}}\dfrac{\partial F}{\partial \sigma_{ij}} D^{e}_{ijkl}}{\dfrac{\partial F}{\partial \sigma_{ij}} D^{e}_{ijkl}\dfrac{\partial Q}{\partial \sigma_{kl}} + H^{p}}\right)\dot{\bar{\varepsilon}}_{kl} \\ &= h n_i \dot{\lambda}_{\Omega\setminus\delta} D^{e}_{ijkl}\frac{\partial Q}{\partial \sigma_{kl}}\end{aligned} \tag{3.53}$$

In this case, it can be proven (Runesson et al. 1991) that the minimum eigenvalue of $\mathbf{Q}^{ep}$ is negative. Considering the fact that all the eigenvalues of $\mathbf{Q}$ are positive in the elastic range, it can be concluded that before the minimum eigenvalue becomes negative it would be zero, so that the problem is again formulated by (3.52). Thus, the condition for the onset of localization requires the vanishing of the determinant of the acoustic tensor (e.g., Rudnicki and Rice 1975)

The bifurcation problem in eq. (3.52) can be solved by an optimization/minimization analysis, e.g. Renegar (2001). The variable in this optimization problem is $\mathbf{n} = n_i$, the normal vector to the discontinuity surface, and when the minimum value of the function is zero the onset of localization takes place.

Some examples of bifurcation analysis in the context of a biaxial compression test are presented in figures below. Unlike the triaxial tests where an axial symmetry condition holds with $\sigma_2 = \sigma_3$, biaxial tests are carried out under plane strain condition, i.e. the strain in the direction of x_2-axis is zero. The typical results are shown in Fig 3-4. The simulations correspond to axial compression at hydrostatic pressure of 100 kPa. The selected material parameters are $\eta_f = 1.2$, $\eta_c = 1.0$, $B = 0.003$, and the only active mechanism is the deviatoric hardening. The variation of deviatoric stress and the evolution of volumetric strain are presented in Fig 3-4a and Fig 3-4b, respectively. Fig 3-4c shows the orientation of the shear band and the distribution of the determinant of the acoustic tensor as a function of n_i (see eqn. (3.52)) at bifurcation point.

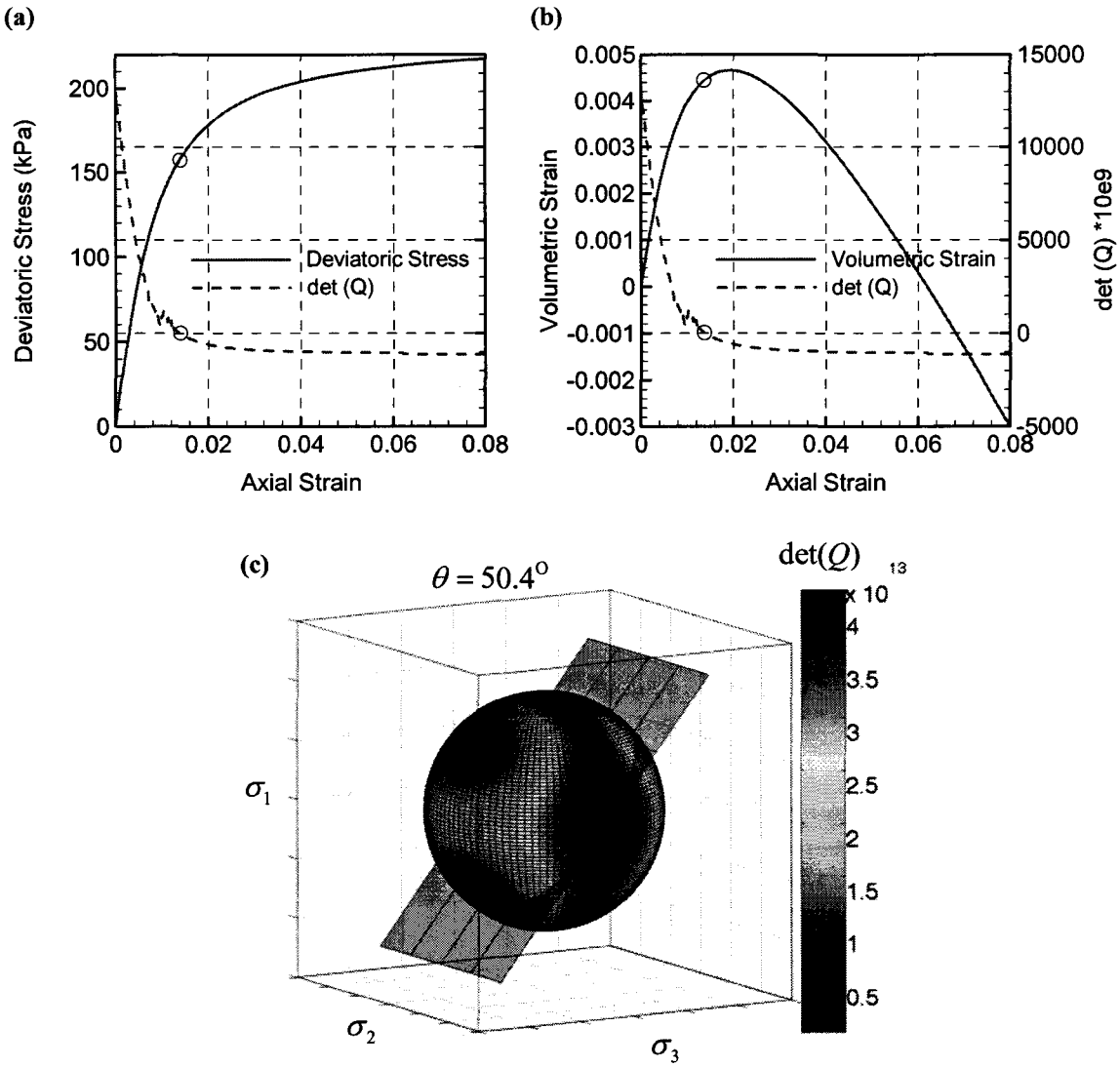

Fig 3-4 Biaxial tests simulation; (a) variation of deviatoric stress and (b) volumetric strain with axial strain, (c) variation of $\det(Q)$ and the orientation of shear band at bifurcation

The results of a similar simulation with $\eta_f = \eta_c = 1.2$, are shown in Fig 3-5. Another simulation with an associated flow rule was carried out and the results are presented in Fig 3-6. In this case, no bifurcation takes place and the deformation mode remains homogeneous.

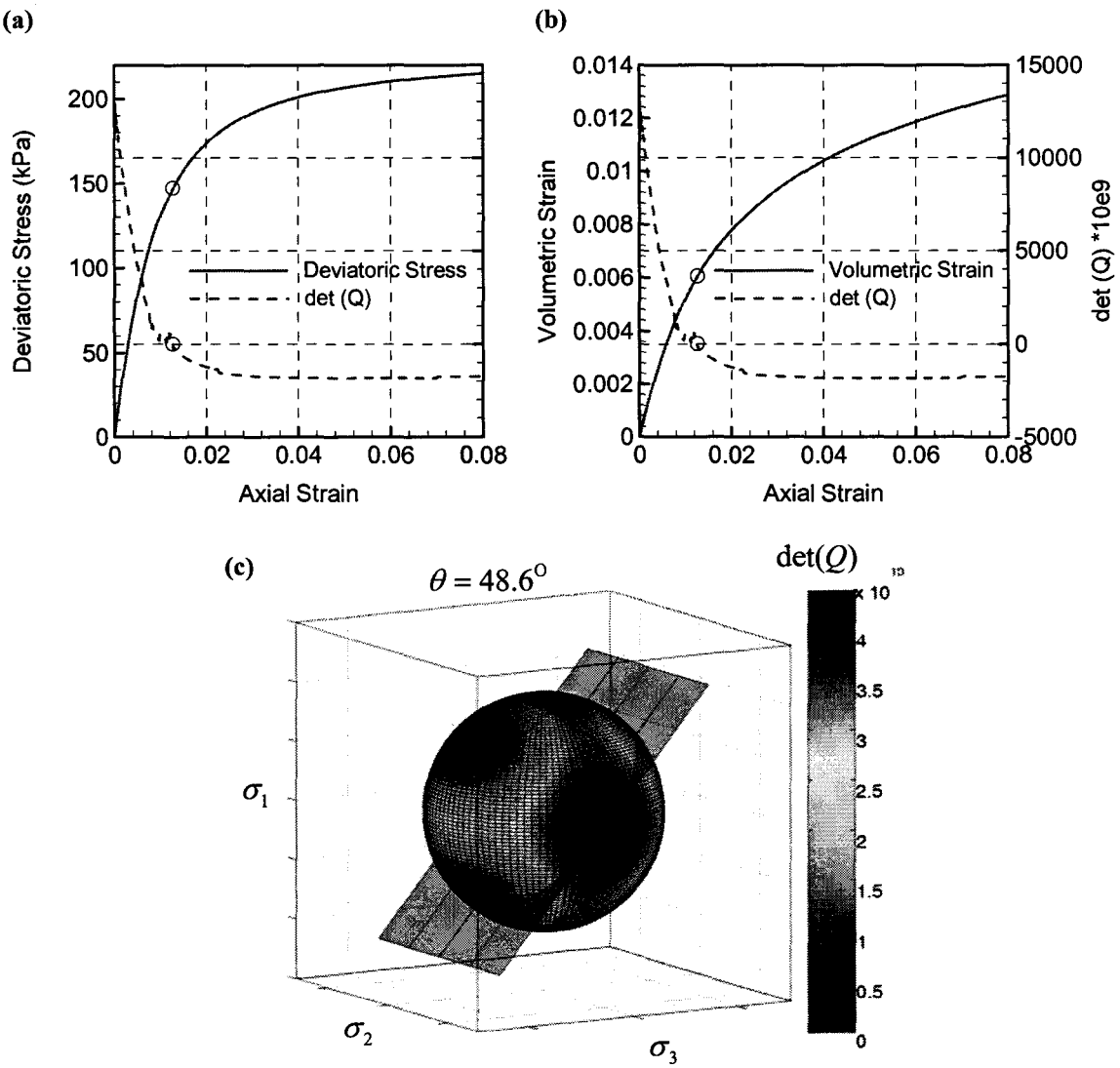

Fig 3-5 Biaxial tests simulation; (a) variation of deviatoric stress and (b) volumetric strain with axial strain, (c) variation of $\det(Q)$ and the orientation of shear band at bifurcation

Note that for an isotropic material the bifurcation analysis provides two solutions corresponding to two conjugate shear band orientations. In the case of anisotropic material, however, the solution leads to only one particular inclination for the shear band.

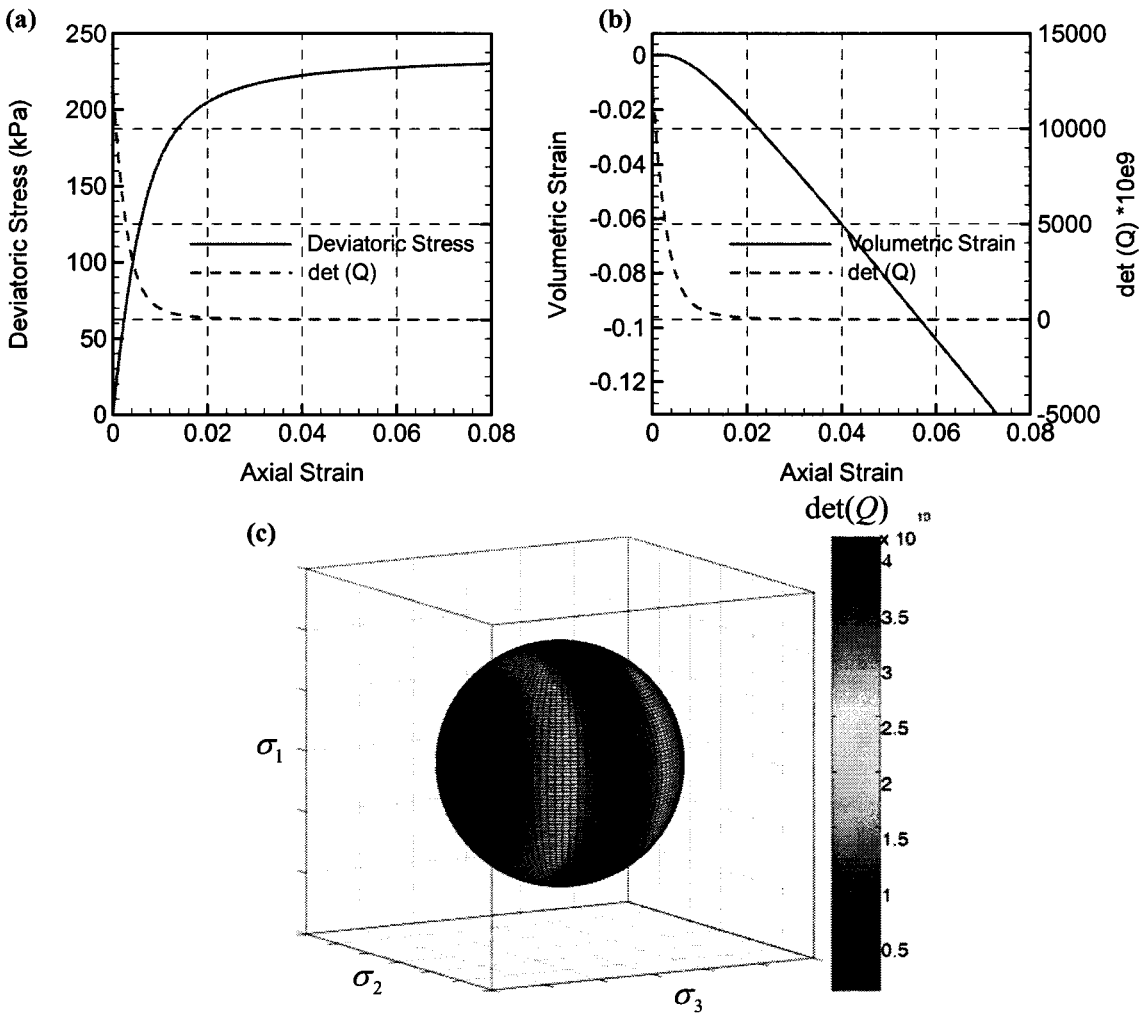

Fig 3-6 Biaxial tests simulation; (a) variation of deviatoric stress and (b) volumetric strain with axial strain (c) variation of $\det(Q)$

3.5.3 Post Localization Behavior, Homogenization Technique

After bifurcation and formation of a shear band the displacement field is no longer continuous, thus the classical continuum mechanics approaches cannot be used to deal with this problem. In order to handle the discontinuous deformation mode, the approaches like non-local approach (e.g., Bazant and Lin 1988, Bazant and Pijaudier-Cabot 1988), gradient-dependent description (e.g., Triantafyllidis and Aifantis 1986), or

similar could be applied. The framework employed in this thesis is based on a simple volume averaging procedure as reported in the work of Pietruszczak (1999). This approach distinguishes between the properties of the shear band and those of the intact material, thereby accounting for the inherent anisotropy of the microstructure. The method handles the issue locally at the material level by employing a homogenization technique.

Fig 3-7 shows schematically a material intercepted by a shear band. Such a composite consists of two simultaneously existing constitutes, i.e. matrix (1) and the material in the discontinuity band (2). Assuming that the constitutes remain homogeneous within themselves, the volume averaging scheme may be employed (Hill 1950).

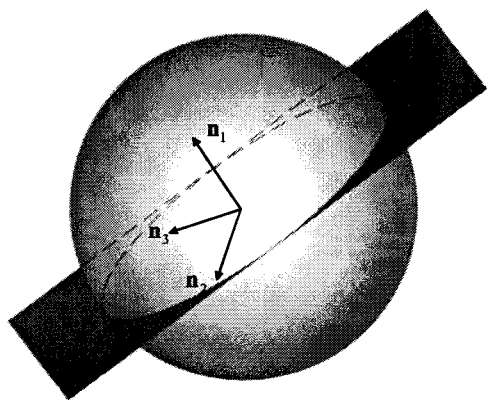

Fig 3-7 Representative element of material intercepted by a discontinuity band

$$\dot{\sigma}_{ij} = \upsilon^{(1)}\dot{\sigma}_{ij}^{(1)} + \upsilon^{(2)}\dot{\sigma}_{ij}^{(2)}$$
$$\dot{\varepsilon}_{ij} = \upsilon^{(1)}\dot{\varepsilon}_{ij}^{(1)} + \upsilon^{(2)}\dot{\varepsilon}_{ij}^{(2)} \tag{3.54}$$

υ_1 and υ_2 are the volume fractions of the matrix and the shear band respectively, i.e.

$$\upsilon^{(1)} = 1 - \frac{At}{V} \quad , \quad \upsilon^{(2)} = \frac{At}{V} \tag{3.55}$$

where V is the volume of the element, A is the area of the cross section and t is the thickness of the shear band. The thickness of shear band (around 10 times of the mean particle size, Muhlhaus and Vardulakis 1987) can be considered as negligible compared to other physical dimensions, so that the shear band can be treated as a discontinuity plane (strong discontinuity). Therefore, it is convenient to express the deformations field within the shear band in terms of velocity discontinuities

$$\dot{g}_i = \{\dot{g}_1 \quad \dot{g}_2 \quad \dot{g}_3\}^T \tag{3.56}$$

Thus, the strain rates generated within the band can be defined as

$$\dot{\varepsilon}_{ij}^{(2)} = \frac{1}{2t}\left(n_i \dot{g}_j + n_j \dot{g}_i\right) \tag{3.57}$$

where n_i is the unit vector normal to the band surface ($\mathbf{n}_1$ in Fig 3-7).

Tractions along the shear band can be related to the velocity discontinuities in the band through a separate constitutive relation:

$$\dot{t}_i = K_{ij} \dot{g}_j \tag{3.58}$$

where K_{ij} is the elastoplastic operator defining the properties in the shear band. Imposing now the requirement of continuity of traction, t_i, along the localization plane, one obtains

$$\dot{t}_i = \dot{\sigma}_{ij}^{(1)} n_j = D_{ijkl} \dot{\varepsilon}_{kl}^{(1)} n_j \tag{3.59}$$

Combining eqs. (3.54), (3.57), (3.58), (3.59) and noting that the thickness t is negligible compared to other dimensions of the representative volume, the following averaged constitutive relation is obtained after some transformations

$$\begin{gathered} \dot{\sigma}_{ij} = D_{ijkl}^{H} \dot{\varepsilon}_{kl} \;\; ; \;\; D_{ijkl}^{H} = D_{ijpq} \left(\delta_{pk} \delta_{ql} - \upsilon n_p S_{qkl} \right) \\ S_{ijk} = \left(K_{ip} + \upsilon D_{imlp} n_m n_l \right)^{-1} D_{pqjk} n_q \end{gathered} \tag{3.60}$$

where, $\upsilon = \upsilon^{(2)}/t$ is a characteristic dimension that is defined as the ratio of the surface area of the localization plane to the volume of the element.

The elastoplastic operator K_{ij} is obtained by incorporating a strain-softening plasticity framework. Referring the problem to a local coordinate system along the shear band and taking x_1-axis along the normal n_i, the yield and plastic potential functions may be defined in a simple linear form

$$f = \tau - \mu\sigma - c = 0; \qquad \psi = \tau - \bar{\mu}\sigma = const. \tag{3.61}$$

Here, $\tau = \sqrt{t_2^2 + t_3^2}$, $\sigma = t_1$ are the shear and normal components of the traction vector (t_i) and $\bar{\mu}$ is a material constant (dilation angle). The softening characteristics may be defined by taking $c = \text{const.}$ and $\mu = \mu(g^p)$ such that

$$\mu = \mu_r + (\mu_0 - \mu_r)e^{-\beta g^p}; \qquad \dot{g}^p = \sqrt{\dot{g}_2^p + \dot{g}_3^p} \tag{3.62}$$

where μ_0 is evaluated at the onset of localization, μ_r is the residual value and β is a material constant. Assuming now the additivity of elastic and plastic parts of the velocity discontinuity vector, and following the standard plasticity procedure, the stiffness operator K_{ij} may be defined as

$$K_{ij} = K_{ij}^e - H^{-1}\left(K_{ip}^e \frac{\partial f}{\partial t_p}\frac{\partial f}{\partial t_q} K_{qj}^e\right); \quad H = \left(\mu\bar{\mu}k_N + k_T\right) + \sigma\kappa(\mu - \mu_r) \tag{3.63}$$

Here, K_{ij}^e is the elastic operator

$$K_{ij}^e = \begin{bmatrix} k_N & 0 & 0 \\ 0 & k_T & 0 \\ 0 & 0 & k_T \end{bmatrix} \tag{3.64}$$

where:

$$K_N = \frac{(1-\nu)E}{(1+\nu)(1-2\nu)t} \tag{3.65}$$

$$K_T = \frac{E}{2(1+\nu)t} \tag{3.66}$$

E and ν are the elastic parameters of the band and t is the thickness of the band.

The numerical results presented later in Chapters 5 show the applicability of the proposed constitutive framework in simulation of the mechanical behavior of geomaterials.

Appendix I

The derivation of equation(3.24):

$$D_{ijkl}^{ep} = D_{ijkl}^{e} - \frac{D_{ijkl}^{e}\frac{\partial Q_1}{\partial \sigma_{kl}}(N_1)_{ij} D_{ijkl}^{e}}{H^{ep}} - \frac{D_{ijkl}^{e}\frac{\partial Q_2}{\partial \sigma_{kl}}(N_2)_{ij} D_{ijkl}^{e}}{H^{ep}} \qquad (3.24)$$

The consistency condition should be satisfied for both mechanisms

$$dF_1 = \frac{\partial F_1}{\partial \sigma_{ij}}\dot{\sigma}_{ij} + \frac{\partial F_1}{\partial \kappa_1}\dot{\kappa}_1 = \frac{\partial F_1}{\partial \sigma_{ij}} D_{ijkl}^{e}(\dot{\varepsilon}_{kl} - \dot{\varepsilon}_{kl}^{p}) + \frac{\partial F_1}{\partial \kappa_1}\dot{\kappa}_1 = 0$$

$$dF_2 = \frac{\partial F_2}{\partial \sigma_{ij}}\dot{\sigma}_{ij} + \frac{\partial F_2}{\partial \kappa_2}\dot{\kappa}_2 = \frac{\partial F_2}{\partial \sigma_{ij}} D_{ijkl}^{e}(\dot{\varepsilon}_{kl} - \dot{\varepsilon}_{kl}^{p}) + \frac{\partial F_2}{\partial \kappa_2}\dot{\kappa}_2 = 0$$

The rate of plastic deformation can be calculated from the flow rule for each mechanism, i.e.

$$dF_1 = \frac{\partial F_1}{\partial \sigma_{ij}} D_{ijkl}^{e}(\dot{\varepsilon}_{kl} - \dot{\lambda}_1\frac{\partial Q_1}{\partial \sigma_{kl}} - \dot{\lambda}_2\frac{\partial Q_2}{\partial \sigma_{kl}}) + \frac{\partial F_1}{\partial \kappa_1}\dot{\kappa}_1 = 0$$

$$dF_2 = \frac{\partial F_2}{\partial \sigma_{ij}} D_{ijkl}^{e}(\dot{\varepsilon}_{kl} - \dot{\lambda}_1\frac{\partial Q_1}{\partial \sigma_{kl}} - \dot{\lambda}_2\frac{\partial Q_2}{\partial \sigma_{kl}}) + \frac{\partial F_2}{\partial \kappa_2}\dot{\kappa}_2 = 0$$

So that

$$dF_1 = \frac{\partial F_1}{\partial \sigma_{ij}} D_{ijkl}^{e}\dot{\varepsilon}_{kl} - \dot{\lambda}_1\frac{\partial F_1}{\partial \sigma_{ij}} D_{ijkl}^{e}\frac{\partial Q_1}{\partial \sigma_{kl}} - \dot{\lambda}_2\frac{\partial F_1}{\partial \sigma_{ij}} D_{ijkl}^{e}\frac{\partial Q_2}{\partial \sigma_{kl}} + \frac{\partial F_1}{\partial \kappa_1}\dot{\kappa}_1 = 0$$

$$dF_2 = \frac{\partial F_2}{\partial \sigma_{ij}} D_{ijkl}^{e}\dot{\varepsilon}_{kl} - \dot{\lambda}_1\frac{\partial F_2}{\partial \sigma_{ij}} D_{ijkl}^{e}\frac{\partial Q_1}{\partial \sigma_{kl}} - \dot{\lambda}_2\frac{\partial F_2}{\partial \sigma_{ij}} D_{ijkl}^{e}\frac{\partial Q_2}{\partial \sigma_{kl}} + \frac{\partial F_2}{\partial \kappa_2}\dot{\kappa}_2 = 0$$

The above representation can also be expressed as

$$dF_1 = \frac{\partial F_1}{\partial \sigma_{ij}} D^e_{ijkl} \dot{\varepsilon}_{kl} - \dot{\lambda}_1 \left(H^e_{11} + H^p_1 \right) - \dot{\lambda}_2 H^e_{12} = 0$$

$$dF_2 = \frac{\partial F_2}{\partial \sigma_{ij}} D^e_{ijkl} \dot{\varepsilon}_{kl} - \dot{\lambda}_1 H^e_{21} - \dot{\lambda}_2 \left(H^e_{22} + H^p_2 \right) = 0$$

where

$$H^p_\beta = -\frac{\partial F_\beta}{\partial \kappa_\beta} \frac{\dot{\kappa}_\beta}{\dot{\lambda}_\beta} \quad , \quad H^e_{\beta\gamma} = \frac{\partial F_\beta}{\partial \sigma_{ij}} D^e_{ijkl} \frac{\partial Q_\gamma}{\partial \sigma_{kl}} \qquad \beta, \gamma = 1,2$$

Now the plastic multipliers can be determined as

$$\dot{\lambda}_1 = \frac{\left(\left(H^e_{22} + H^p_2 \right) \frac{\partial F_1}{\partial \sigma_{ij}} - H^e_{12} \frac{\partial F_2}{\partial \sigma_{ij}} \right) D^e_{ijkl} \dot{\varepsilon}_{kl}}{\left(H^e_{11} + H^p_1 \right) \left(H^e_{22} + H^p_2 \right) - H^e_{12} H^e_{21}} = \frac{\left(N_1 \right)_{ij} D^e_{ijkl} \dot{\varepsilon}_{kl}}{H^{ep}}$$

$$\dot{\lambda}_2 = \frac{\left(\left(H^e_{11} + H^p_1 \right) \frac{\partial F_2}{\partial \sigma_{ij}} - H^e_{21} \frac{\partial F_1}{\partial \sigma_{ij}} \right) D^e_{ijkl} \dot{\varepsilon}_{kl}}{\left(H^e_{11} + H^p_1 \right) \left(H^e_{22} + H^p_2 \right) - H^e_{12} H^e_{21}} = \frac{\left(N_2 \right)_{ij} D^e_{ijkl} \dot{\varepsilon}_{kl}}{H^{ep}}$$

Using the above values of the plastic multipliers, the constitutive relation can be defined as

$$\dot{\sigma}_{ij} = D^e_{ijkl} \dot{\varepsilon}^e_{kl} = D^e_{ijkl} (\dot{\varepsilon}_{kl} - \dot{\varepsilon}^p_{kl}) = D^e_{ijkl} (\dot{\varepsilon}_{kl} - \dot{\lambda}_1 \frac{\partial Q_1}{\partial \sigma_{kl}} - \dot{\lambda}_2 \frac{\partial Q_2}{\partial \sigma_{kl}})$$

$$= D^e_{ijkl} \left(\dot{\varepsilon}_{kl} - \frac{\left(N_1 \right)_{ij} D^e_{ijkl} \dot{\varepsilon}_{kl}}{H^{ep}} \frac{\partial Q_1}{\partial \sigma_{kl}} - \frac{\left(N_2 \right)_{ij} D^e_{ijkl} \dot{\varepsilon}_{kl}}{H^{ep}} \frac{\partial Q_2}{\partial \sigma_{kl}} \right)$$

$$= \left(D^e_{ijkl} - \frac{D^e_{ijkl} \frac{\partial Q_1}{\partial \sigma_{kl}} \left(N_1 \right)_{ij} D^e_{ijkl}}{H^{ep}} - \frac{D^e_{ijkl} \frac{\partial Q_2}{\partial \sigma_{kl}} \left(N_2 \right)_{ij} D^e_{ijkl}}{H^{ep}} \right) \dot{\varepsilon}_{kl}$$

so that the tangent operator becomes

$$D_{ijkl}^{ep} = D_{ijkl}^{e} - \frac{D_{ijkl}^{e} \dfrac{\partial Q_1}{\partial \sigma_{kl}} \left(N_1\right)_{ij} D_{ijkl}^{e}}{H^{ep}} - \frac{D_{ijkl}^{e} \dfrac{\partial Q_2}{\partial \sigma_{kl}} \left(N_2\right)_{ij} D_{ijkl}^{e}}{H^{ep}}$$

Appendix II

The derivation of equation (3.43) :

$$\frac{\partial \Psi}{\partial \sigma_{ij}} = \frac{\partial \Psi}{\partial \xi}\frac{\partial \xi}{\partial \sigma_{ij}} = 2\bar{\Psi}(1+2\psi_1\xi+3\psi_2\xi+...)\frac{A_{ki}\sigma_{kj}\sigma_{pq}\sigma_{pq} - A_{pk}\sigma_{pq}\sigma_{kq}\sigma_{ij}}{(\sigma_{mn}\sigma_{mn})^2} \quad (3.43)$$

Above equation is derived from the definition of Ψ and ξ in (3.39), i.e.

$$\Psi = \bar{\Psi}\left(1+\xi+\psi_1\xi^2+\psi_2\xi^3+\psi_3\xi^4+.....\right), \quad \xi = A_{ij}l_i l_j = \frac{A_{ik}\sigma_{ij}\sigma_{kj}}{\sigma_{pq}\sigma_{pq}} \quad (3.39)$$

$$\frac{\partial \Psi}{\partial \sigma_{ij}} = \frac{\partial \Psi}{\partial \xi}\frac{\partial \xi}{\partial \sigma_{ij}}$$

$$\frac{\partial \Psi}{\partial \xi} = 2\bar{\Psi}(1+2\psi_1\xi+3\psi_2\xi+...)$$

$$\frac{\partial \xi}{\partial \sigma_{ij}} = \frac{\partial\left(\frac{A_{pk}\sigma_{pq}\sigma_{kq}}{\sigma_{mn}\sigma_{mn}}\right)}{\partial \sigma_{ij}} = \frac{\frac{\partial\left(A_{pk}\sigma_{pq}\sigma_{kq}\right)}{\partial \sigma_{ij}}\sigma_{mn}\sigma_{mn} - \frac{\partial\left(\sigma_{mn}\sigma_{mn}\right)}{\partial \sigma_{ij}}A_{pk}\sigma_{pq}\sigma_{kq}}{(\sigma_{mn}\sigma_{mn})^2}$$

$$\frac{\partial \xi}{\partial \sigma_{ij}} = \frac{A_{pk}\delta_{pi}\delta_{qj}\sigma_{kq}\sigma_{mn}\sigma_{mn} + A_{pk}\delta_{ki}\delta_{qj}\sigma_{pq}\sigma_{mn}\sigma_{mn} - 2A_{pk}\delta_{mi}\delta_{nj}\sigma_{mn}\sigma_{pq}\sigma_{kq}}{(\sigma_{mn}\sigma_{mn})^2}$$

$$\frac{\partial \xi}{\partial \sigma_{ij}} = \frac{A_{ki}\sigma_{kj}\sigma_{mn}\sigma_{mn} + A_{pi}\sigma_{pj}\sigma_{mn}\sigma_{mn} - 2A_{pk}\sigma_{ij}\sigma_{pq}\sigma_{kq}}{(\sigma_{mn}\sigma_{mn})^2}$$

$$\frac{\partial \xi}{\partial \sigma_{ij}} = 2\frac{A_{ki}\sigma_{kj}\sigma_{pq}\sigma_{pq} - A_{pk}\sigma_{ij}\sigma_{pq}\sigma_{kq}}{(\sigma_{mn}\sigma_{mn})^2}$$

$$\boxed{\frac{\partial \Psi}{\partial \sigma_{ij}} = \frac{\partial \Psi}{\partial \xi}\frac{\partial \xi}{\partial \sigma_{ij}} = 2\bar{\Psi}(1+2\psi_1\xi+3\psi_2\xi+...)\frac{A_{ki}\sigma_{kj}\sigma_{pq}\sigma_{pq} - A_{pk}\sigma_{pq}\sigma_{kq}\sigma_{ij}}{(\sigma_{mn}\sigma_{mn})^2}}$$

Appendix III

The derivation of equation (3.60)

$$\dot{\sigma}_{ij} = D^{H}_{ijkl}\dot{\varepsilon}_{kl}; \quad D^{H}_{ijkl} = D^{(1)}_{ijpq}\left(\delta_{pk}\delta_{ql} - \upsilon n_p S_{qkl}\right); \quad S_{ijk} = \left(D^{(2)}_{ip} + \upsilon D^{(1)}_{imlp} n_m n_l\right)^{-1} D^{(1)}_{pqjk} n_q$$

The above equations were derived by combining equations of homogenization (3.54), kinematic and static constraints viz (3.57) and (3.59), and invoking the two constitutive relations for the two constitutes, i.e. $\dot{\sigma}^{(1)}_{ij} = D^{(1)}_{ijkl}\dot{\varepsilon}^{(1)}_{kl}$ and $\dot{t}_i = K_{ij}\dot{g}_j$.

$$\left.\begin{aligned} &\dot{\sigma}_{ij} = \dot{\sigma}^{(1)}_{ij} \\ &\dot{\varepsilon}_{ij} = \dot{\varepsilon}^{(1)}_{ij} + \frac{\upsilon}{2}\left(n_i\dot{g}_j + n_j\dot{g}_i\right) \end{aligned}\right\} \begin{array}{l}\text{Averaging/Homogenization} \\ \text{Kinematic Constraints}\end{array}$$

$$\left.\begin{aligned} &\dot{t}_i = \dot{\sigma}^{(1)}_{ij} n_j \end{aligned}\right\} \begin{array}{l}\text{Static Constraints} \\ \text{Traction Continuity Across the Band}\end{array}$$

$$\Rightarrow \begin{cases} \dot{t}_i = \dot{\sigma}^{(1)}_{ij} n_j = D_{ijkl}\dot{\varepsilon}^{(1)}_{kl} n_j = D_{ijkl}\left(\dot{\varepsilon}_{kl} - \dfrac{\upsilon}{2}\left(n_k\dot{g}_l + n_l\dot{g}_k\right)\right) n_j \\ \dot{t}_i = K_{iq}\dot{g}_q \end{cases}$$

$$\Rightarrow K_{im}\dot{g}_m = D_{ijkl}\left(\dot{\varepsilon}_{kl} - \frac{\upsilon}{2}\left(n_k\dot{g}_l + n_l\dot{g}_k\right)\right) n_j$$

$$\Rightarrow K_{im}\dot{g}_m = D_{ijkl}\dot{\varepsilon}_{kl} n_j - \frac{\upsilon}{2}\left(D_{ijkl} n_k\dot{g}_l n_j + D_{ijkl} n_l\dot{g}_k n_j\right)$$

$$\Rightarrow K_{im}\dot{g}_m = D_{ijkl}\dot{\varepsilon}_{kl} n_j - \upsilon D_{ijkl} n_k\dot{g}_l n_j$$

$$\Rightarrow \left[K_{im} + \upsilon D_{ijkm} n_k n_j\right]\dot{g}_m = D_{ijkl}\dot{\varepsilon}_{kl} n_j$$

$$\Rightarrow \dot{g}_m = \left[K_{im} + \upsilon D_{ijkm} n_k n_j\right]^{-1} D_{ijkl} n_j\dot{\varepsilon}_{kl} = S_{mkl}\dot{\varepsilon}_{kl}$$

$$\dot{\sigma}_{ij} = \dot{\sigma}_{ij}^{(1)} = D_{ijkl}\varepsilon_{kl}^{(1)} = D_{ijkl}\left(\dot{\varepsilon}_{kl} - \frac{\upsilon}{2}\left(n_k\dot{g}_l + n_l\dot{g}_k\right)\right)$$

$$\dot{\sigma}_{ij} = D_{ijkl}\left(\dot{\varepsilon}_{kl} - \frac{\upsilon}{2}\left(n_k\dot{g}_l + n_l\dot{g}_k\right)\right) = D_{ijkl}\left(\dot{\varepsilon}_{kl} - \frac{\upsilon}{2}\left(n_k S_{lpq}\dot{\varepsilon}_{pq} + n_l S_{kpq}\dot{\varepsilon}_{pq}\right)\right)$$

$$\dot{\sigma}_{ij} = D_{ijkl}\dot{\varepsilon}_{kl} - \frac{\upsilon}{2}\left(D_{ijkl}n_k S_{lpq}\dot{\varepsilon}_{pq} + D_{ijkl}n_l S_{kpq}\dot{\varepsilon}_{pq}\right)$$

$$\dot{\sigma}_{ij} = D_{ijkl}\dot{\varepsilon}_{kl} - \upsilon D_{ijpq}n_p S_{qkl}\dot{\varepsilon}_{kl} = D_{ijpq}\left(\delta_{pk}\delta_{ql} - \upsilon n_p S_{qkl}\right)\dot{\varepsilon}_{kl}$$

$$\dot{\sigma}_{ij} = D^H_{ijkl}\dot{\varepsilon}_{kl}$$

$$\boxed{D^H_{ijkl} = D_{ijpq}\left(\delta_{pk}\delta_{ql} - \upsilon n_p S_{qkl}\right)}$$

CHAPTER 4

IDENTIFICATION OF MATERIAL FUNCTIONS/PROPERTIES

4.1 Introduction

Implementation of the framework outlined in Chapter 3, requires the specification of material functions/parameters prior to localization as well as the properties of the material contained within the shear band. The experimental studies conducted in this thesis, which include the direct shear, triaxial and hollow cylinder tests, were designed to provide the necessary data for the identification of all material parameters. Most of the parameters used in the formulation have a clear physical significance and the identification procedure is rather straightforward. The parameters that need to be identified implicitly, through the best fit, include the constant B in definition of the deviatoric hardening mechanism, as well as the parameters defining the anisotropy functions.

4.2 Material Functions/Parameters Prior to Strain Localization

The material parameters for the volumetric hardening mechanism, (λ, κ, e_0), can be identified using the data from a hydrostatic compression test with loading and unloading paths. Here , $e_0 = 0.6$ is the initial void ratio of the material, while the parameters λ and κ define the slope of loading and unloading branches, respectively, in the relation between the void ratio and the natural logarithm of p. Note that for

hydrostatic compression, the only active mechanism is the volumetric hardening. This mechanism is more likely to be employed for a cohesive material. For sands, it would in general be sufficient to use the deviatoric hardening mechanism alone. For the sake of completeness a multimechanism framework is considered here and a general formulation is presented.

In the deviatoric hardening mechanism, η_f is related to the shear strength, i.e. the friction angle, while C is the hydrostatic tension resistance. More ever, η_c is the stress ratio at which the volumetric behavior changes from compaction to dilation. Strength anisotropy can be simulated by directional-dependency in η_f. With the directional dependency in η_c and B, along with an anisotropic elastic behavior, the formulation can capture all aspects of the anisotropy in the deformation characteristics.

Consider first the directional dependency of the strength parameter η_f that appears in the deviatoric hardening mechanism. The identification of the material function (3.39) requires the information on the conditions at failure in samples tested at different orientations relative to the direction of loading. As mentioned earlier, such tests cannot be performed without overcoming significant difficulties. In triaxial testing setup the problem stems from the fact that an anisotropic material subjected to triaxial compression tends to distort. This distortion, however, is constrained by the presence of loading platens, rendering the results for inclined samples unreliable. In case of hollow cylinder tests with equal internal and external cell pressures, the effects of intermediate principal stress on the material behavior cannot be decoupled form the effects of

anisotropy. The stress path with $\sigma_2 = \sigma_3$ can only be achieved at the expense of nonuniformity in the stress distribution, and this makes the experimental data unreliable.

In view of these difficulties, an implicit approach has been adopted here. In this strategy, the results of direct shear tests at different angles of deposition (Chapter 2.2) were employed to predict, using the critical plane approach (Chapter 3.4.1), the response in axial compression at different orientations of the sample. The latter information was subsequently used to identify the variation of strength parameter η_f with loading direction. Assume that the conditions at failure are defined by Coulomb's linear form

$$F = \tau - \mu\sigma - c = 0; \quad \mu = \mu(n_i), \; c = c(n_i) \tag{4.1}$$

where (τ, σ) are the shear and normal components of the traction vector on a plane with unit normal n_i and μ and c are both said to be orientation dependent. The distribution of strength parameters can be directly defined based on the results of direct shear tests. Let the distribution of $\mu = \tan\phi$ be described by

$$\mu = \hat{\mu}\left(1 + \Omega_{ij} n_i n_j + b_1 (\Omega_{ij} n_i n_j)^2 + b_2 (\Omega_{ij} n_i n_j)^3 + b_3 (\Omega_{ij} n_i n_j)^4 + ...\right) \tag{4.2}$$

where Ω_{ij} is a traceless symmetric tensor. Referring the problem to the principal material system and assuming that x_3-axis is along the direction of deposition, so that $n_i = (0, \sin\alpha, \cos\alpha)$, there is

$$\Omega_1 = \Omega_2; \quad \Omega_1 + \Omega_2 + \Omega_3 = 0; \qquad \Omega_{ij} n_i n_j = \Omega_1 (1 - 3\cos^2\alpha) \tag{4.3}$$

so that

$$\mu = \hat{\mu}\left(1+\Omega_1(1-3\cos^2\alpha)+b_1\Omega_1^2(1-3\cos^2\alpha)^2+b_2\Omega_1^3(1-3\cos^2\alpha)^3+.....\right) \quad (4.4)$$

The best-fit approximations employing representation (4.4) are shown in Fig 4-1a. The results incorporate the dyadic products of degrees up to 2 and 4, respectively. Evidently, the approximation including terms up to order 4 is more accurate and corresponds to

$$\Omega_1 = 0.1419679,\ \hat{\mu} = 1.06463,\ b_1 = 5.1768,\ b_2 = 31.2851,\ b_3 = 87.8614$$

A similar methodology may be applied to describe the bias in the spatial variation of cohesion c. Employing the representation analogous to that of (4.4) and denoting the respective material parameters as $\hat{c}, \Omega_{ij}^c, d_1, d_2, ...$, the second-order approximation, as shown in Fig 4-1b, yields

$$\Omega_1^c = 0.2229053,\ \hat{c} = 3.509254,\ d_1 = 0.8161$$

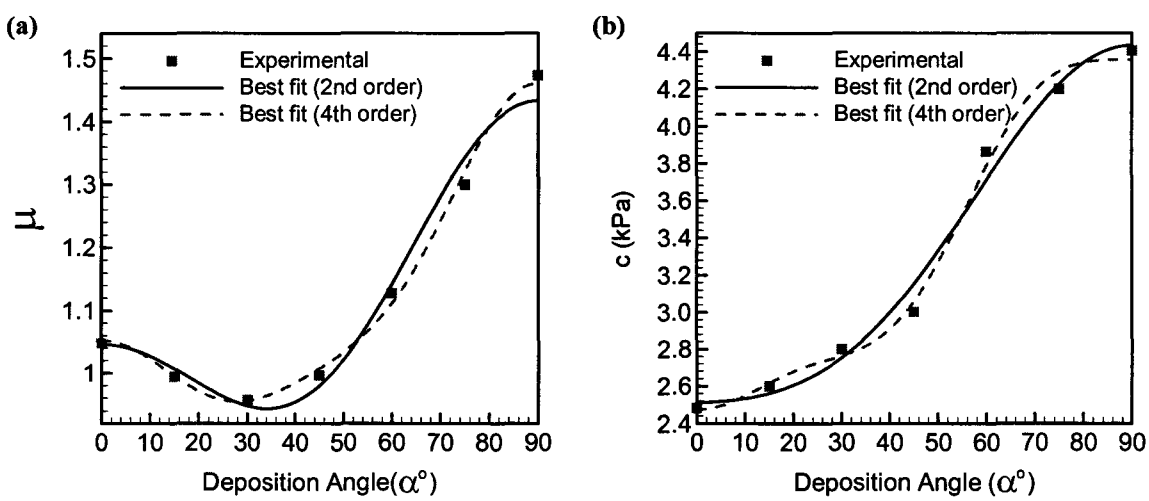

Fig 4-1 Variation of (a) μ and (b) cohesion with the angle of deposition

The framework outlined above can now be incorporated to generate a set of data describing the variation of compressive strength at different confining pressures and different orientations of the sample. The latter information may then be employed to identify the material function $\eta_f = \eta_f(l_i)$

$$\eta_f = \bar{\eta}_f \left(1 + A_{ij} l_i l_j + a_1 (A_{ij} l_i l_j)^2 + a_2 (A_{ij} l_i l_j)^3 + a_3 (A_{ij} l_i l_j)^4 + ...\right) \tag{4.5}$$

The prediction of strength under triaxial conditions represents a constrained optimization problem which can be solved by Lagrange multipliers or any other known technique (e.g. interior point method, see Renegar 2001). The problem is defined as

$$F = \underbrace{\max}_{n_i} \left(\tau - \mu\sigma - c\right) = 0; \quad \mu = \mu(n_i), \; c = c(n_i), \; n_i n_i = 1 \tag{4.6}$$

Fig 4-2 shows the predicted variation of compressive strength, $R_c = \sigma_1$, at p_0=0, 10, 50, 100 and 150kPa. For cases of p_0=10, 50, 100 and 150kPa the experimental data from triaxial tests are also included in the plots, and are clearly quite consistent with the predictions made by the critical plane analysis.

For the triaxial compression and hollow cylinder tests, the function $\eta_f = \eta_f(l_i)$, eq.(4.5), reduces to

$$A_{ij} l_i l_j = A_1 (1 - 3l_3^2); \qquad l_3^2 = \frac{\sigma_3^2 \sin^2\alpha + \sigma_1^2 \cos^2\alpha}{\sigma_1^2 + \sigma_2^2 + \sigma_3^2}; \quad \alpha^* = \cos^{-1}(l_3) \tag{4.7}$$

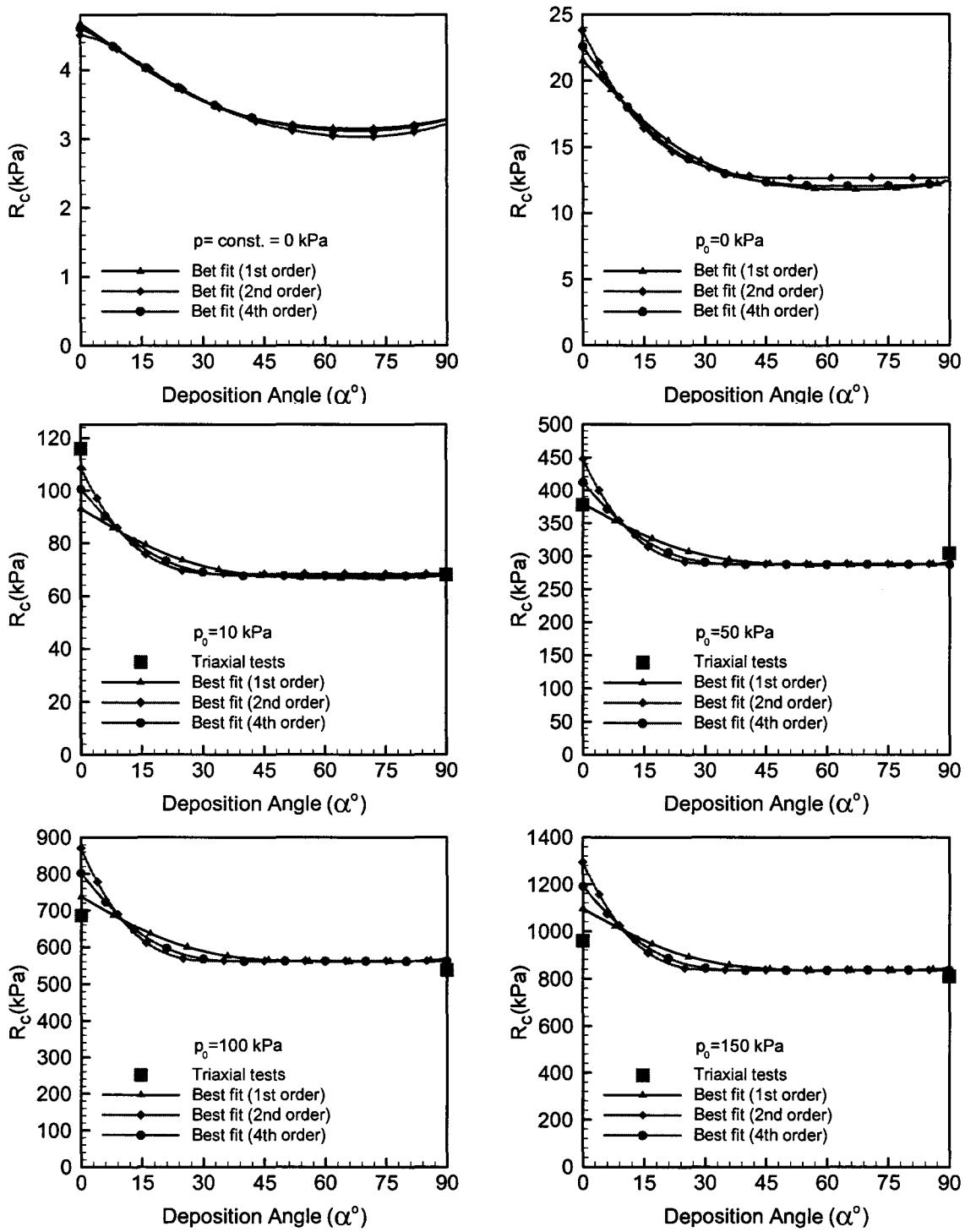

Fig 4-2 Estimate of maximum axial stress by critical plane analysis for $p = const. = 0$ kPa , triaxial state of stress with confining pressures $p_0 = 0,10,50,100,150$kPa and experimental results on the samples with $\alpha = 0^{\circ}$ and $\alpha = 90^{\circ}$

so that

$$\eta_f = \overline{\eta}_f \left(1 + A_1(1-3l_3^2) + a_1 A_1^2 (1-3l_3^2)^2 + a_2 A_1^3 (1-3l_3^2)^3 + a_3 A_1^4 (1-3l_3^2)^4 + ...\right) \quad (4.8)$$

Fig 4-3 shows the best-fit approximations to the set of data obtained for all values of p_0 within the range from 0 to 150kPa. The results are plotted in the affined space $\{\eta_f, l_3\}$ and correspond to representation (4.8). For comparison and validation of the proposed method, the experimental data from the triaxial (TC) and hollow cylinder (HC) tests are also shown on the same plot. The material parameters for the 2nd order best-fit curve are:

$$A_1 = .0078412, \ \overline{\eta}_f = 1.6978, \ \ a_1 = 835.7128$$

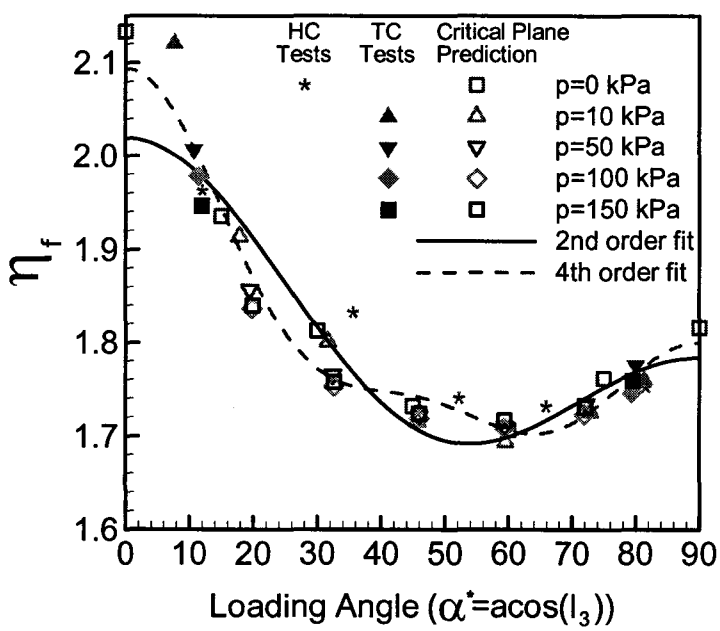

Fig 4-3 Variation of η_f with the loading angle

The value of the strength parameter C, can be defined by examining the response under hydrostatic tension σ_t. In this case, for any orientation n_i there is $\tau = 0$, $\sigma = \sigma_t$, so that the representation (4.6) reduces to

$$F = \underbrace{\max}_{n_i}\left(\sigma_t - c/\mu\right) = 0 \quad \Rightarrow \quad \sigma_t = C = \underbrace{\min}_{n_i}\left(c/\mu\right) = const. \tag{4.9}$$

Thus, for an oriented microstructure, the tensile strength parameter C is invariant with respect to orientation and its value corresponds to $\min\left(c/\mu\right) = 2.4$.

The specification of deformation characteristics requires the assessment of elastic properties, the hardening parameter B and plastic potential parameter η_c. The elastic moduli for vertical ($\alpha = 0^0$) and horizontal ($\alpha = 90^0$) samples were identified from unloading probes along the triaxial compression paths. In general, these values are affected by the stress state; particularly, by the magnitude of the confining pressure. For simplicity and transparency of the framework, constant values were assigned to these parameters

$$E_1 = 6.0 \text{ MPa},\ E_3 = 12.0 \text{ MPa},\ \nu_{12} = 0.25,\ \nu_{13} = 0.20,\ G_{13} = 3.75 \text{MPa}$$

Directional dependency of B and η_c can be described using a similar representation to that of η_f in (4.8). Here, again for the sake of simplicity, it is assumed that $\eta_c = 0.8\eta_f$, while $B = 0.003 = const.$ for all loading directions.

To verify the performance of the constitutive framework outlined in Chapter 3, the triaxial and hollow cylinder experiments have been simulated numerically. The details of the integration procedure are provided in the next chapter.

Fig 4-4 to Fig 4-7 present the results of simulations of triaxial tests performed at confinements of $p_0 = 10, 50, 100$ and $150\,\text{kPa}$.

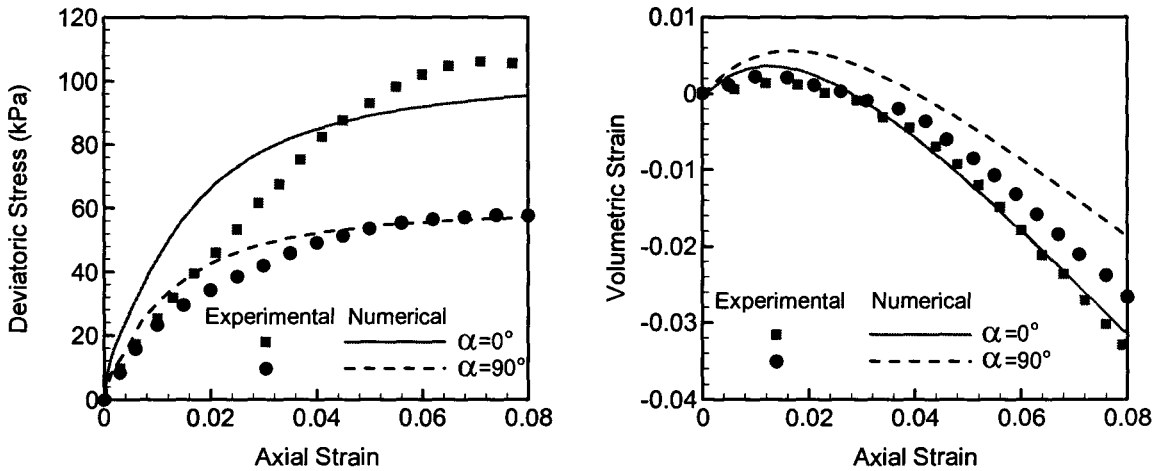

Fig 4-4 Numerical simulations of triaxial tests at confining pressure $p_0 = 10\,\text{kPa}$; variation of deviatoric stress and volumetric strain with axial deformation

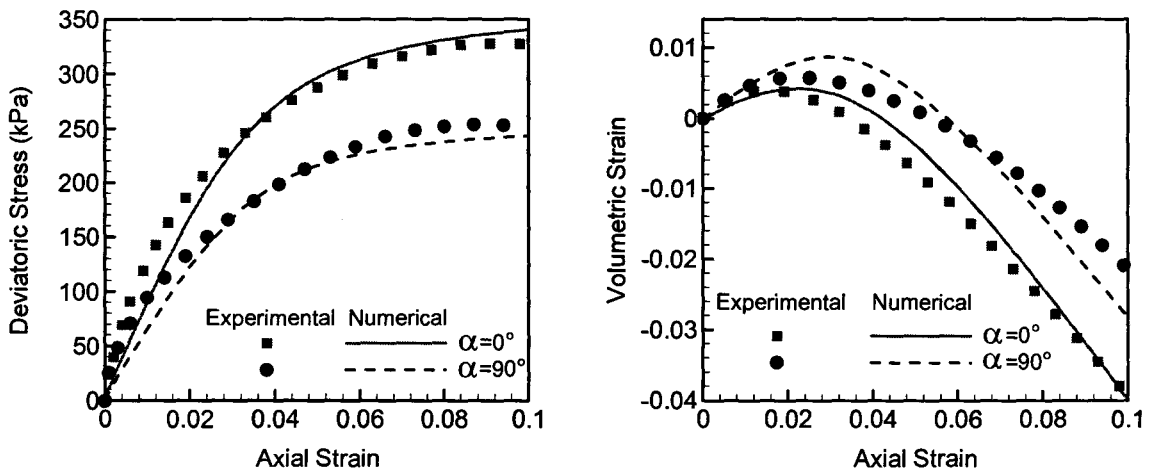

Fig 4-5 Numerical simulations of triaxial tests at confining pressure $p_0 = 50\,\text{kPa}$; variation of deviatoric stress and volumetric strain with axial deformation

The simulations were terminated at the onset of localized deformation, as the response in the post-localization regime represents a boundary-value problem.

Fig 4-8 shows the set of results for hollow cylinder tests at constant pressure of $p = 100\,\text{kPa}$ for $\alpha = 0^{\circ}, 45^{\circ}, 90^{\circ}$ and $\alpha = 30^{\circ}, 60^{\circ}$, respectively.

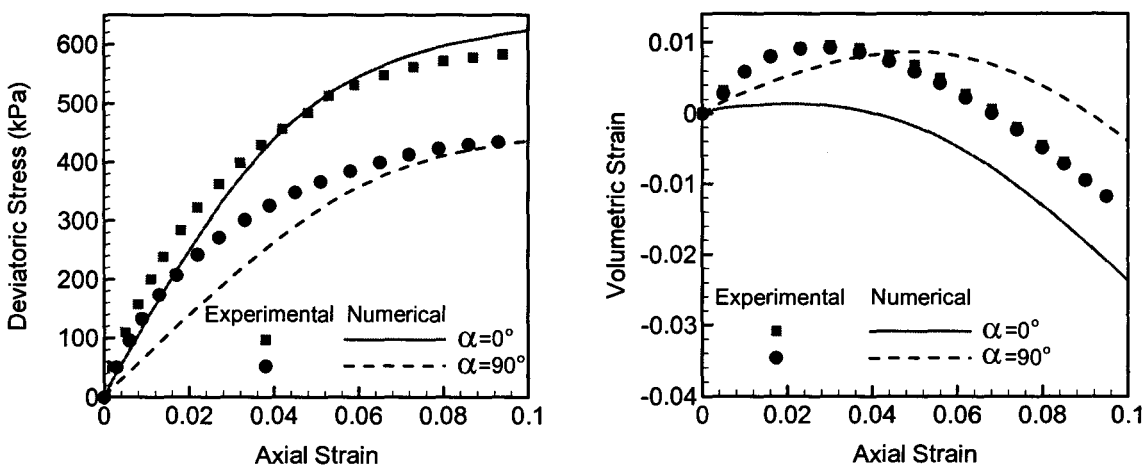

Fig 4-6 Numerical simulations of triaxial tests at confining pressure $p_0 = 100\,\text{kPa}$; variation of deviatoric stress and volumetric strain with axial deformation

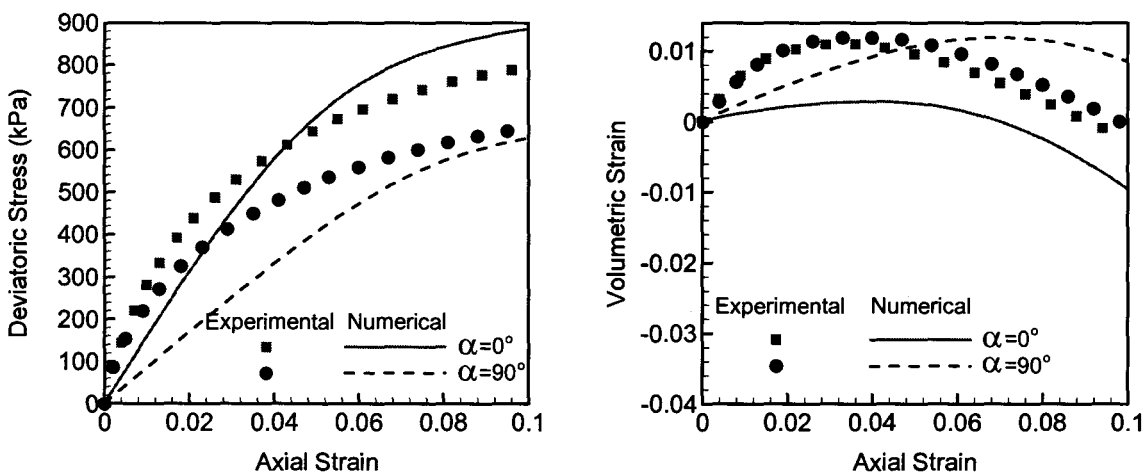

Fig 4-7 Numerical simulations of triaxial tests at confining pressure $p_0 = 150\,\text{kPa}$; variation of deviatoric stress and volumetric strain with axial deformation

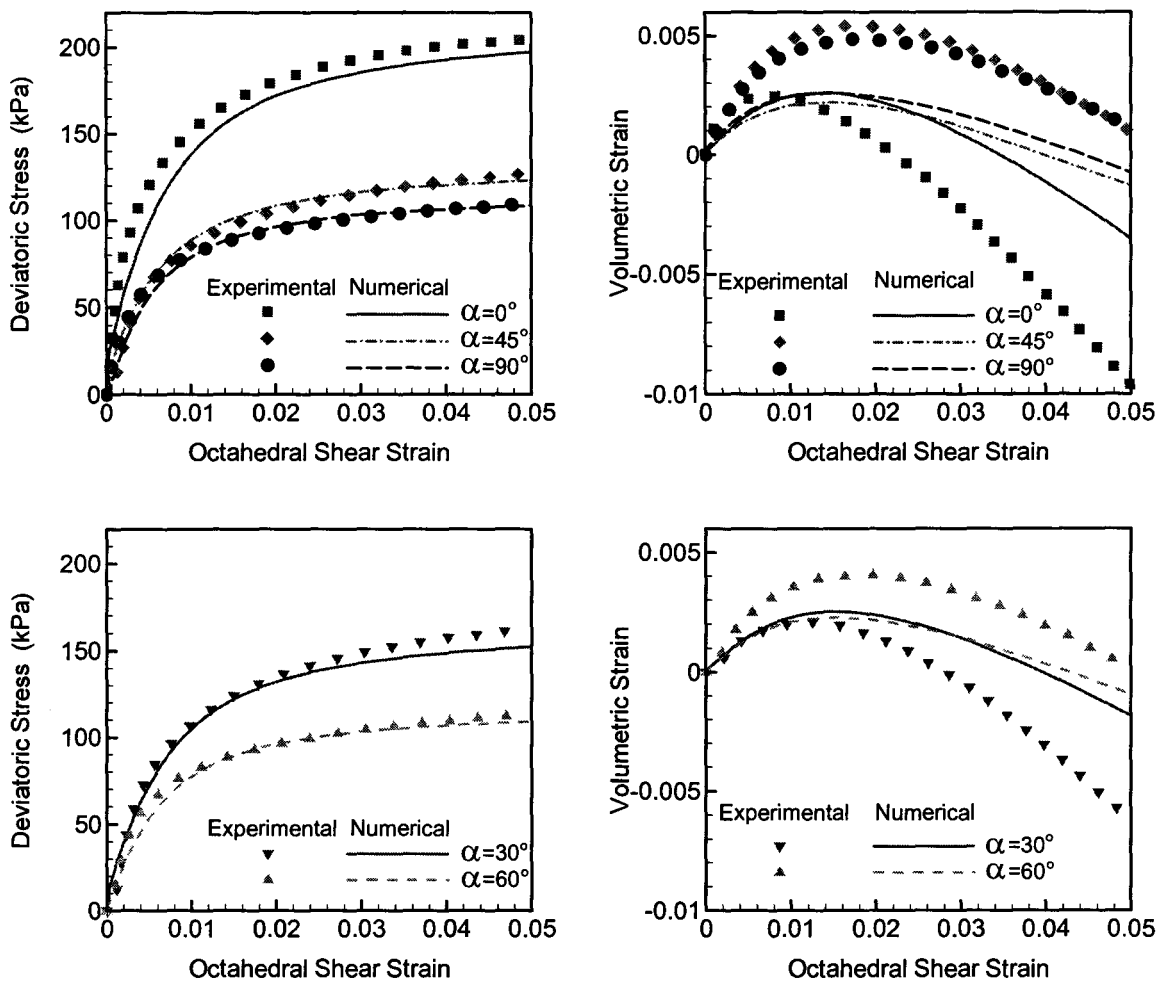

Fig 4-8 Numerical simulations of hollow cylinder tests at a constant confining pressure $p = 100\,\text{kPa}$; variation of deviatoric stress and volumetric strain with octahedral shear strain

It is evident that for both the triaxial and hollow cylinder tests the predicted response, in terms of strength and volume change characteristics, is fairly consistent with the experimental data.

Note that for the cases depicted in Fig 4-5 and Fig 4-8, the initial slope of the stress-strain characteristics is close to that observed experimentally. This is because the values of elastic modulus were selected for the mean stress level close to 100 kPa. For

tests at lower confinement (Fig 4-4) the initial slope is overpredicted, while for those at higher stress levels (Fig 4-6 and Fig 4-7) it is underpredicted. The maximum level of the deviatoric stress intensities is close to the observed values in most cases. This provides a justification for the procedure implemented in the identification of strength parameter η_f, i.e. combination of the data obtained from direct shear tests on inclined samples with the critical plane analysis.

4.3 Identification of Material Parameters in the Shear Band

The description of post-localization response, within the context of a boundary-value problem, requires the specification of properties along the shear band. These can best be assessed by examining the deformation characteristics obtained from direct shear tests. Note that in a shear test the sample is failed along a pre-defined localization plane. Therefore, the traction-displacement characteristics in the post-peak regime are representative of those along the shear band. Referring to Fig 2-5 to Fig 2-8, it is evident that the unstable response commences at horizontal displacements of approximately 2mm, while the residual state is reached at displacement in the range of 7mm. At the same time, the residual friction angle may be estimated as 45°, irrespective of the value of α. Given this information, the parameters in the evolution law (3.62) have been estimated as

$$\mu_r = 1.0, \qquad \beta = 800\,\mathrm{m}^{-1}$$

Fig 4-9 shows the shear band characteristics corresponding to this choice of parameters. Apparently, the exponential law (3.62) is restrictive; the general trends, however, are consistent with the experimental data. The value of the characteristic dimension υ, eq.(3.60), is assessed at the level of a boundary-value problem based on the volume associated with the respective integration point within the finite element mesh (Pietruszczak and Niu 1993).

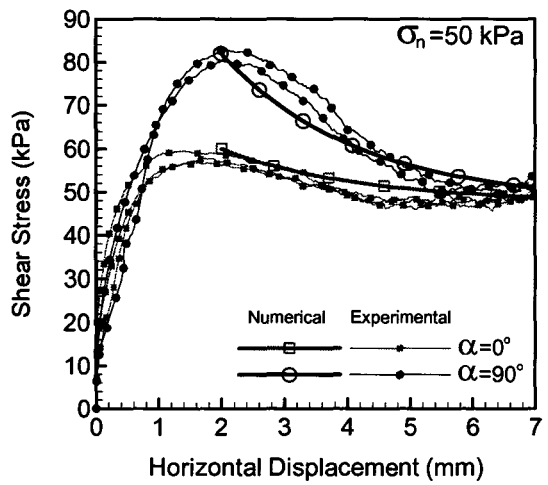

Fig 4-9 Specification of shear band characteristics (Note: results correspond to direct shear at normal stress $\sigma_n = 50$ kPa)

CHAPTER 5
NUMERICAL ANALYSIS

5.1 Introduction

In a numerical analysis of an elasto-plastic problem it becomes necessary to integrate the incremental constitutive equations governing the behavior of the material. Whereas accuracy in the computation of the tangent stiffness matrix can be substantially relaxed at the expense of convergence speed, the precision with which the constitutive relations are integrated has a direct impact on the overall accuracy of the analysis (Oritz and Popov 1985). The existing integration schemes can be classified into two different categories; one uses the trapezoidal rule and the other uses the midpoint rule. The classical approaches, viz. radial return, mean normal and closest point procedures, are particular cases of those families (e.g. Borja and Lee 1990, Hofstetter et al. 1993, Simo and Hughes 1998). In this chapter, general integration algorithms are outlined for the elastoplastic constitutive equations employing single and multi yield surface formulations. The trapezoidal rule is subsequently applied for the constitutive model proposed in Chapter 3. Later the simulations of some undrained hollow cylinder tests are presented to verify the performance of the constitutive model and the integration scheme.

The proposed constitutive framework and the integration algorithm have been implemented in a commercial FE package (ABAQUS). In the second part of this chapter, the numerical simulations of the scaled footing tests, as described in Chapter 2, were

carried out using FE analysis that incorporated the material properties identified in Chapter 4. The detailed results, including an extensive parametric study, are presented and compared with the experimental data.

5.2 Integration Algorithm for a Single Yield Surface Formulation

The mechanical behavior of a wide range of elasto-plastic materials can be characterized by means of a set of constitutive relations in the general form

$$F\left(\sigma_{ij},\boldsymbol{\kappa}\right)=0\ ;\quad Q\left(\sigma_{ij}\right)=const. \tag{5.1}$$

$$\dot{\varepsilon}_{kl}=\dot{\varepsilon}^{e}_{kl}+\dot{\varepsilon}^{p}_{kl} \tag{5.2)a}$$

$$\dot{\sigma}_{ij}=D^{e}_{ijkl}\dot{\varepsilon}^{e}_{kl} \tag{5.2)b}$$

$$\dot{\varepsilon}^{p}_{kl}=\dot{\lambda}\frac{\partial Q}{\partial\sigma_{kl}} \tag{5.2)c}$$

$$\dot{\kappa}=\dot{\lambda}\frac{\partial\kappa}{\partial\varepsilon^{p}_{kl}}\frac{\partial Q}{\partial\sigma_{kl}} \tag{5.2)d}$$

In the equations above, D^{e}_{ijkl} is the elastic constitutive tensor, $\dot{\lambda}$ is the plastic multiplier and κ is the hardening parameter. Eqn. (5.2)a is the additivity postulate that allows division of the increment of total strain into the elastic and plastic parts, eqn. (5.2)b is the generalized Hooke's law, while eqn. (5.2)d is the hardening rule.

The loading/unloading criteria are defined by the Kuhn-Tucker conditions (Luenberger 1984)

$$F\left(\sigma_{ij},\kappa\right)\le 0\;;\;\; \dot{\lambda}\ge 0\;;\;\; \dot{\lambda}F=0 \tag{5.3}$$

The case of $F\left(\sigma_{ij},\kappa\right)<0$ yields $\dot{\lambda}=0$, and corresponds to elastic behavior. For $\dot{\lambda}>0$ the material undergoes plastic deformation and the stress state remains on the yield surface, i.e. $F\left(\sigma_{ij},\kappa\right)=0$. During plastic flow the consistency condition ($dF=0$) is automatically satisfied by (5.3).

In the context of finite element analysis the constitutive equations are integrated at the Gaussian points. The main function of the constitutive subroutine is to get increment of strain as input, and to calculate the updated state of stress and the updated hardening parameters as output. If the global iteration scheme of the finite element analysis is based on Newton-Raphson method, the consistent tangent operator (or the elasto-plastic constitutive tensor) also needs to be calculated. As mentioned previously, the precision with which the constitutive relations are integrated has a direct impact on the overall accuracy of the analysis. An acceptable integration algorithm should satisfy the basic requirements of numerical stability and accuracy. The following subsections present two families of integration algorithms for elastoplastic constitutive equations in case of a single yield surface models.

5.2.1 Generalized Trapezoidal Rule

This approach incorporates a class of algorithms for the integration of eqns. (5.2) under constraints (5.3). The governing equations are

$$\left(\dot{\sigma}_{ij}\right)_{n+1} = D^{e}_{ijkl}\left(\dot{\varepsilon}_{n+1} - \dot{\varepsilon}^{p}_{n+1}\right) \tag{5.4)a}$$

$$\left(\dot{\varepsilon}_{ij}\right)^{p}_{n+1} = \dot{\lambda}\left((1-\omega)\left(\frac{\partial Q}{\partial \sigma_{ij}}\right)_{n} + \omega\left(\frac{\partial Q}{\partial \sigma_{ij}}\right)_{n+1}\right) \tag{5.4)b}$$

$$\dot{\kappa}_{n+1} = \dot{\lambda}\frac{\partial \kappa}{\partial \varepsilon^{p}_{ij}}\left((1-\omega)\left(\frac{\partial Q}{\partial \sigma_{ij}}\right)_{n} + \omega\left(\frac{\partial Q}{\partial \sigma_{ij}}\right)_{n+1}\right) \tag{5.4)c}$$

$$F\left(\left(\sigma_{ij}\right)_{n+1}, \kappa_{n+1}\right) = F\left(\left(\sigma_{ij}\right)_{n} + \left(\dot{\sigma}_{ij}\right)_{n+1}, \kappa_{n} + \dot{\kappa}_{n+1}\right) = 0 \tag{5.4)d}$$

where subscripts $(n,\ n+1)$ are the step/increment counters and ω is a constant $0 \le \omega \le 1$. Geometric representation of the integration scheme is presented in Fig 5-1, and is obtained by rephrasing the set equation (5.4) as

$$\left(\sigma_{ij}\right)^{Trial}_{n+1} = \left(\sigma_{ij}\right)_{n} + D^{e}_{ijkl}\left(\dot{\varepsilon}_{kl}\right)_{n+1} \tag{5.5)a}$$

$$\left(\sigma_{ij}\right)_{n+1} = \left(\sigma_{ij}\right)^{Trial}_{n+1} - \dot{\lambda}D^{e}_{ijkl}\left((1-\omega)\left(\frac{\partial Q}{\partial \sigma_{kl}}\right)_{n} + \omega\left(\frac{\partial Q}{\partial \sigma_{kl}}\right)_{n+1}\right) \tag{5.5)b}$$

$$\kappa_{n+1} = \kappa_{n} + \dot{\lambda}\left(\frac{\partial \kappa}{\partial \varepsilon^{p}_{ij}}\right)\left((1-\omega)\left(\frac{\partial Q}{\partial \sigma_{ij}}\right)_{n} + \omega\left(\frac{\partial Q}{\partial \sigma_{ij}}\right)_{n+1}\right) \tag{5.5)c}$$

$$F\left(\left(\sigma_{ij}\right)_{n+1}, \kappa_{n+1}\right) = 0 \tag{5.5)d}$$

Fig 5-1 illustrates how the stress state is updated in two steps. In the first step, assuming the material is in elastic range, the increment of stress is calculated from (5.5)a. This trial stress, i.e. $\left(\sigma_{ij}\right)_{n+1}^{Trial}$, is called the elastic predictor. If the trial stress is not in the elastic domain, such as in the case shown in Fig 5-1, according to Kuhn-Tucker conditions the material undergoes plastic deformation and the stress state should be mapped onto the updated yield surface. This is done in the second step using (5.5)b and (5.5)c, where the plastic flow is calculated based on the state parameters at the current and the previous steps (n and $n+1$). At the end of calculations, the updated state of stress satisfies the equation of the updated yield surface (5.5)d.

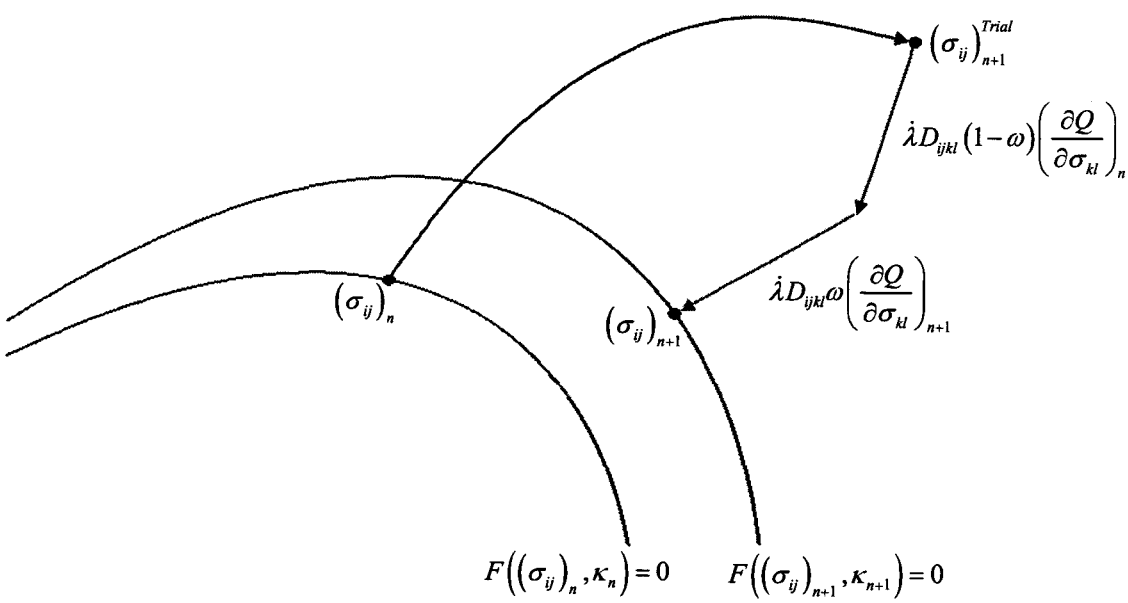

Fig 5-1 Geometric interpretation of the generalized trapezoidal rule

When $\omega = 0$ the algorithm is explicit. The method resembles the classical approach, where the plastic multiplier can be evaluated directly from the consistency condition (see section 3.2). For $\omega > 0$ the algorithm is implicit, and the plastic multiplier should be evaluated by an iterative procedure. By considering $\omega = 0.5$ and a particular case of an elasto-perfect plastic von-Mises model with an associated flow rule, the algorithm coincides with the mean-normal procedure proposed by Rice and Tracy (1973). Choosing $\omega = 1$ along with an associated flow rule, the closest point projection algorithm is obtained (Borja and Lee 1990, Hofstetter et al. 1993). The closest projection algorithm is known to be unconditionally stable if the yield function is convex, but it is only of first order accuracy. Choosing $\omega = 0.5$ provides unconditional stability and boosts the integration accuracy to the second order (Oritz and Popov 1985).

In an implicit scheme, the plastic multiplier and subsequently the updated state of stress and hardening parameters, are obtained using an iterative algorithm. The consecutive steps for the generalized trapezoidal rule are presented in Flowchart 5-1. The algorithm begins with the trial elastic stress, which does not satisfy the Kuhn-Tuker conditions. The algorithm consist of two iterative levels; i.e. global iterative procedure shown by superscript s, within which a local iteration procedure is embedded shown by superscript m. Before starting the iterative loops, the initial value for the updated stress state is set to be the elastic predictor; initial plastic multiplier is considered to be zero and the updated hardening parameters are equal to their values at step n. Then the loop for the global iteration starts, by calculating the plastic deformation based on the stress state at step n, and step $n+1$ at global iteration $s = 0$. The Kuhn-Tuker conditions are

checked, and if not satisfied, the algorithm enters the local iteration loop. Inputs to the local iteration loop are state of stress, hardening parameters and the plastic multiplier at the end of the recent global iteration, and the outputs are the updated values satisfying the Kuhn-Tuker conditions. The values updated in the local iteration loop are then inputs for the next global iteration, where plastic strain is recalculated and the updated state of stress and hardening parameters are found for iteration $s+1$. If the new values satisfy the Kuhn-Tuker conditions, the global iteration loop is terminated and the analysis moves to the next step/increment. Otherwise, the new values are inputs for another round of local iterations.

To update the plastic multiplier in the local iteration process, the following relations are applied

$$\dot{\lambda}^{k,m+1} = \dot{\lambda}^{k,m} + \frac{F\left(\left(\sigma_{ij}\right)_{n+1}^{k,m}, \kappa_{n+1}^{k,m}\right)}{\left(H^e\right)_{n+1}^{k} + \left(H^p\right)_{n+1}^{k}} \tag{5.6a}$$

$$\left(H^e\right)_{n+1}^{s} = \left(\left(\frac{\partial F}{\partial \sigma_{ij}}\right)_{n+1}^{s}\right) D_{ijkl}^{e} \left((1-\omega)\left(\frac{\partial Q}{\partial \sigma_{kl}}\right)_{n} + \omega\left(\frac{\partial Q}{\partial \sigma_{kl}}\right)_{n+1}^{s}\right) \tag{5.6b}$$

$$\left(H^p\right)_{n+1}^{s} = -\left(\left(\frac{\partial F}{\partial \kappa}\right)_{n+1}^{s}\right)^{T} \left(\frac{\partial \kappa}{\partial \varepsilon_{ij}^{p}}\right)^{T} \left((1-\omega)\left(\frac{\partial Q}{\partial \sigma_{ij}}\right)_{n} + \omega\left(\frac{\partial Q}{\partial \sigma_{ij}}\right)_{n+1}^{s}\right) \tag{5.6c}$$

Details of the numerical procedure are presented in Appendix I.

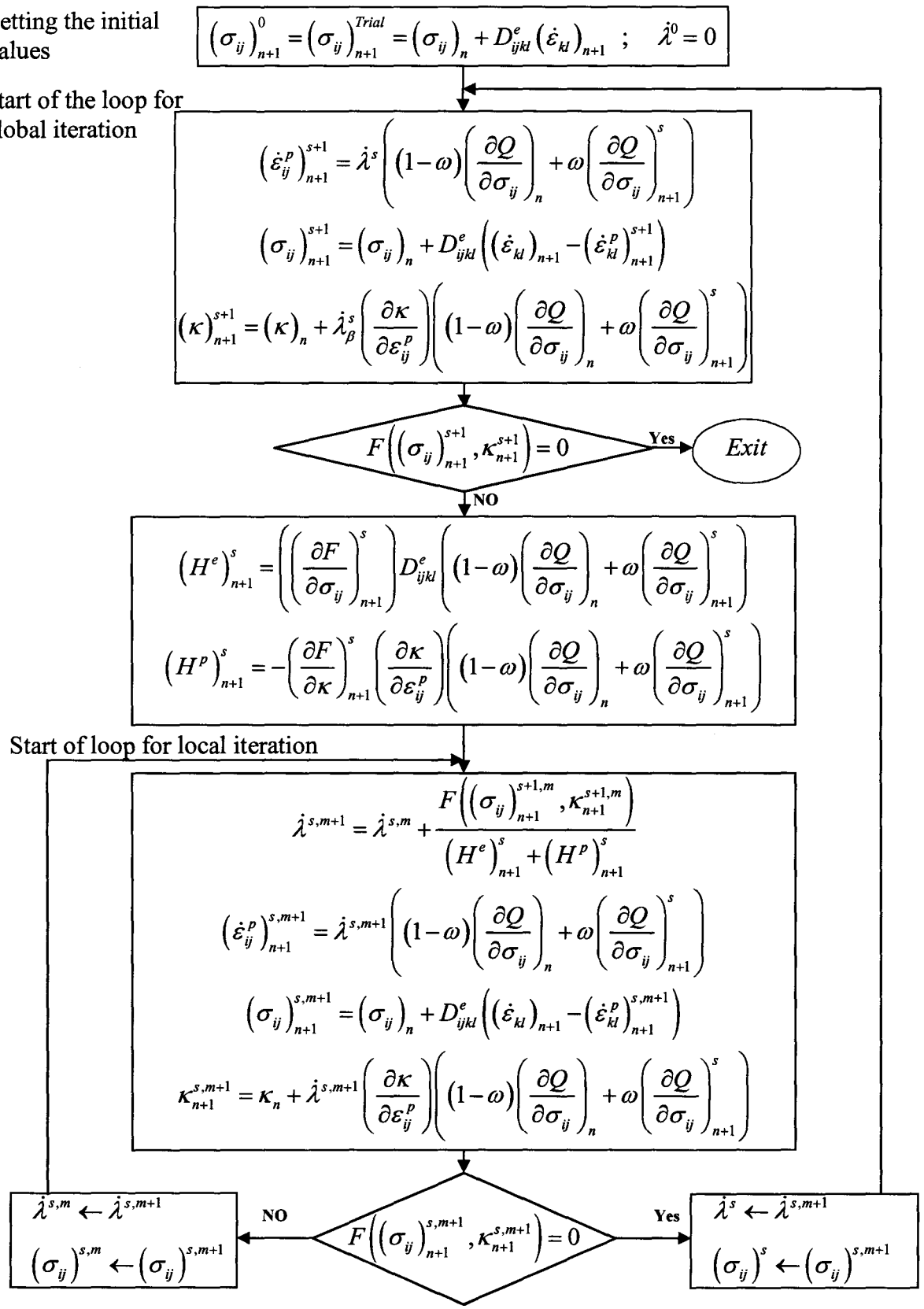
Setting the initial values
$\left(\sigma_{ij}\right)_{n+1}^{0}=\left(\sigma_{ij}\right)_{n+1}^{Trial}=\left(\sigma_{ij}\right)_{n}+D_{ijkl}^{e}\left(\dot{\varepsilon}_{kl}\right)_{n+1}\ ;\quad \dot{\lambda}^{0}=0$
Start of the loop for global iteration
$\left(\dot{\varepsilon}_{ij}^{p}\right)_{n+1}^{s+1}=\dot{\lambda}^{s}\left((1-\omega)\left(\frac{\partial Q}{\partial\sigma_{ij}}\right)_{n}+\omega\left(\frac{\partial Q}{\partial\sigma_{ij}}\right)_{n+1}^{s}\right)$
$\left(\sigma_{ij}\right)_{n+1}^{s+1}=\left(\sigma_{ij}\right)_{n}+D_{ijkl}^{e}\left(\left(\dot{\varepsilon}_{kl}\right)_{n+1}-\left(\dot{\varepsilon}_{kl}^{p}\right)_{n+1}^{s+1}\right)$
$\left(\kappa\right)_{n+1}^{s+1}=\left(\kappa\right)_{n}+\dot{\lambda}_{\beta}^{s}\left(\frac{\partial\kappa}{\partial\varepsilon_{ij}^{p}}\right)\left((1-\omega)\left(\frac{\partial Q}{\partial\sigma_{ij}}\right)_{n}+\omega\left(\frac{\partial Q}{\partial\sigma_{ij}}\right)_{n+1}^{s}\right)$
$F\left(\left(\sigma_{ij}\right)_{n+1}^{s+1},\kappa_{n+1}^{s+1}\right)=0$
Yes
Exit
NO
$\left(H^{e}\right)_{n+1}^{s}=\left(\left(\frac{\partial F}{\partial\sigma_{ij}}\right)_{n+1}^{s}\right)D_{ijkl}^{e}\left((1-\omega)\left(\frac{\partial Q}{\partial\sigma_{ij}}\right)_{n}+\omega\left(\frac{\partial Q}{\partial\sigma_{ij}}\right)_{n+1}^{s}\right)$
$\left(H^{p}\right)_{n+1}^{s}=-\left(\frac{\partial F}{\partial\kappa}\right)_{n+1}^{s}\left(\frac{\partial\kappa}{\partial\varepsilon_{ij}^{p}}\right)\left((1-\omega)\left(\frac{\partial Q}{\partial\sigma_{ij}}\right)_{n}+\omega\left(\frac{\partial Q}{\partial\sigma_{ij}}\right)_{n+1}^{s}\right)$
Start of loop for local iteration
$\dot{\lambda}^{s,m+1}=\dot{\lambda}^{s,m}+\frac{F\left(\left(\sigma_{ij}\right)_{n+1}^{s+1,m},\kappa_{n+1}^{s+1,m}\right)}{\left(H^{e}\right)_{n+1}^{s}+\left(H^{p}\right)_{n+1}^{s}}$
$\left(\dot{\varepsilon}_{ij}^{p}\right)_{n+1}^{s,m+1}=\dot{\lambda}^{s,m+1}\left((1-\omega)\left(\frac{\partial Q}{\partial\sigma_{ij}}\right)_{n}+\omega\left(\frac{\partial Q}{\partial\sigma_{ij}}\right)_{n+1}^{s}\right)$
$\left(\sigma_{ij}\right)_{n+1}^{s,m+1}=\left(\sigma_{ij}\right)_{n}+D_{ijkl}^{e}\left(\left(\dot{\varepsilon}_{kl}\right)_{n+1}-\left(\dot{\varepsilon}_{kl}^{p}\right)_{n+1}^{s,m+1}\right)$
$\kappa_{n+1}^{s,m+1}=\kappa_{n}+\dot{\lambda}^{s,m+1}\left(\frac{\partial\kappa}{\partial\varepsilon_{ij}^{p}}\right)\left((1-\omega)\left(\frac{\partial Q}{\partial\sigma_{ij}}\right)_{n}+\omega\left(\frac{\partial Q}{\partial\sigma_{ij}}\right)_{n+1}^{s}\right)$
$F\left(\left(\sigma_{ij}\right)_{n+1}^{s,m+1},\kappa_{n+1}^{s,m+1}\right)=0$
NO
Yes
$\dot{\lambda}^{s,m}\leftarrow\dot{\lambda}^{s,m+1}$
$\left(\sigma_{ij}\right)^{s,m}\leftarrow\left(\sigma_{ij}\right)^{s,m+1}$
$\dot{\lambda}^{s}\leftarrow\dot{\lambda}^{s,m+1}$
$\left(\sigma_{ij}\right)^{s}\leftarrow\left(\sigma_{ij}\right)^{s,m+1}$

5.2.2 Generalized Midpoint Rule

An alternative family of algorithms can be obtained from a midpoint rule, which takes the following general form

$$\left(\dot{\sigma}_{ij}\right)_{n+1} = D^{e}_{ijkl}\left(\left(\dot{\varepsilon}_{kl}\right)_{n+1} - \left(\dot{\varepsilon}^{p}_{kl}\right)_{n+1}\right) \tag{5.7a}$$

$$\left(\dot{\varepsilon}^{p}_{ij}\right)_{n+1} = \dot{\lambda}\left(\frac{\partial Q}{\partial \sigma_{ij}}\right)_{n+\omega} \tag{5.7b}$$

$$\dot{\kappa}_{n+1} = \dot{\lambda}\left(\frac{\partial \kappa}{\partial \varepsilon^{p}_{ij}}\right)\left(\frac{\partial Q}{\partial \sigma_{ij}}\right)_{n+\omega} \tag{5.7c}$$

$$F\left(\left(\sigma_{ij}\right)_{n+1}, \kappa_{n+1}\right) = F\left(\left(\sigma_{ij}\right)_{n} + \left(\dot{\sigma}_{ij}\right)_{n+1}, \kappa_{n} + \dot{\kappa}_{n+1}\right) = 0 \tag{5.7d}$$

Here $0 \le \omega \le 1$, while $n+\omega$ means that the values have to be evaluated for a midpoint between the n and $n+1$. Geometric representation of (5.7) is presented in Fig 5-2. Similar to the trapezoidal rule, in the midpoint rule the stress state is also updated in two steps. In the first step the elastic predictor is calculated, $\left(\sigma_{ij}\right)^{Trial}_{n+1}$. If the trial state is not in the elastic domain, the material undergoes plastic deformation and the stress state should be mapped onto the updated yield surface. In this case, the plastic deformation is calculated based on state parameters evaluated at a midpoint between the current and the previous steps (n and $n+1$). By analogy to trapezoidal rule, when $\omega = 0$ the algorithm is explicit and when $\omega > 0$ the algorithm is implicit. For the implicit case, the plastic multiplier should be evaluated by an iterative procedure similar to that presented in Flowchart 5-1.

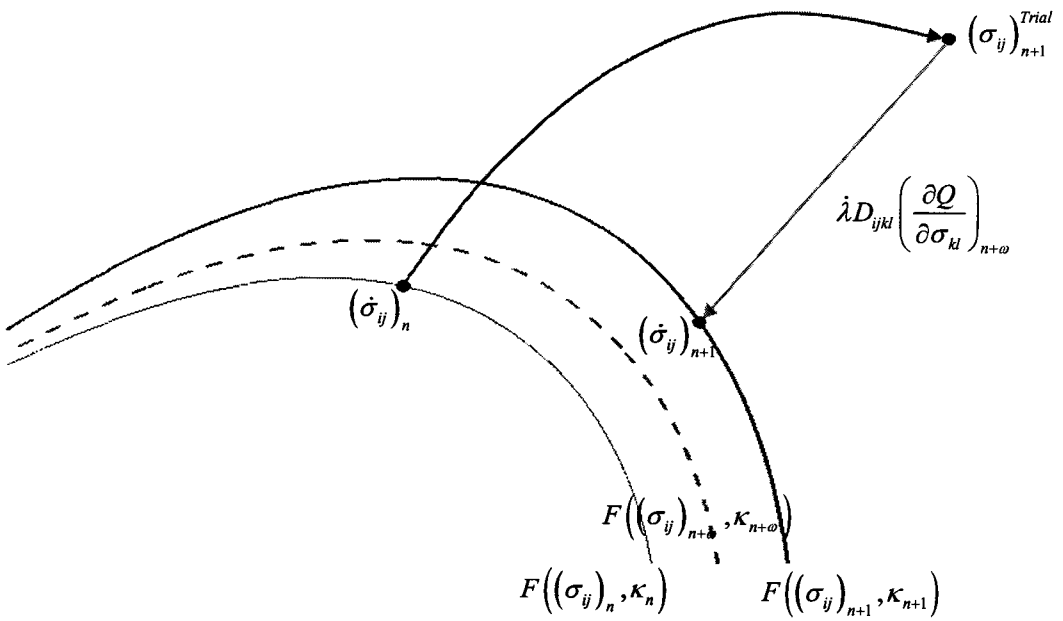

Fig 5-2 Geometric interpretation of the midpoint rule

5.3 Integration Algorithm for Multi Yield Surface Formulation

Consider now a multi-surface constitutive model, where $F_\alpha(\sigma_{ij}, \kappa) = 0$ is a set of yield surfaces and $Q_\alpha(\sigma_{ij}) = const$ the corresponding set of plastic potentials. The basic elasto-plastic constitutive relations are

$$\dot{\varepsilon}_{ij} = \dot{\varepsilon}^e_{ij} + \dot{\varepsilon}^p_{ij} \tag{5.8)a}$$

$$\dot{\sigma}_{ij} = D^e_{ijkl}\dot{\varepsilon}^e_{kl} \tag{5.8)b}$$

$$\dot{\varepsilon}^p_{ij} = \sum_\alpha \left(\dot{\varepsilon}^p_{ij}\right)_\alpha = \sum_\alpha \dot{\lambda}_\alpha \frac{\partial Q_\alpha}{\partial \sigma_{ij}} \tag{5.8)c}$$

$$\dot{\kappa}_\alpha = \dot{\lambda}_\alpha \frac{\partial \kappa_\alpha}{\partial \varepsilon^p_{ij}} \frac{\partial Q_\alpha}{\partial \sigma_{ij}} \tag{5.8)d}$$

where subscript α stands for each yield surface or mechanism. Eqns. (5.8) represent additivity postulate, Hooke's law, flow and hardening rules for each mechanism (Vermeer 1978, Simo et al. 1988, Hofstetter et al. 1993, Simo and Hughes 1998). The total rate of plastic strain in eqn. (5.8)c is the sum of the strain rates for all the mechanisms that contribute to the plastic flow. The loading/unloading criteria are defined by the Kuhn-Tucker conditions for all the mechanisms involved, i.e.

$$F_\alpha\left(\sigma_{ij},\kappa\right)\le 0 \quad ; \quad \dot{\lambda}_\alpha \ge 0 \quad ; \quad \dot{\lambda}_\alpha F_\alpha = 0 \tag{5.9}$$

The integration algorithm discussed here is based on the generalized trapezoidal rule, presented in section 5.2.1. The method automatically identifies the active mechanisms that contribute to the plastic flow, and integrates the relations (5.8) while satisfying the conditions (5.9).

Since the integration scheme employed in this study is based on this approach, the numerical algorithm is described here in more details. The integration begins with the elastic predictor

$$\left(\sigma_{ij}\right)_{n+1}^{Trial} = \left(\sigma_{ij}\right)_n + D^e_{ijkl}\left(\dot{\varepsilon}_{kl}\right)_{n+1} \tag{5.10}$$

Then the first Kuhn-Tuker criterion is checked for all the yield surfaces

$$F_\alpha\left(\left(\sigma_{ij}\right)_{n+1}^{Trail},\boldsymbol{\kappa}_n\right)\le 0 \qquad \text{for} \quad \forall\alpha\in\{1,2,\ldots,m\} \Rightarrow \text{Elastic Step} \tag{5.11}$$

$$F_\beta\left(\left(\sigma_{ij}\right)_{n+1}^{Trail},\boldsymbol{\kappa}_n\right)> 0 \qquad \text{for} \quad \exists\beta\in\{1,2,\ldots,m\} \Rightarrow \text{Plastic Step} \tag{5.12}$$

If the trial stress from (5.10) satisfies the condition (5.11) the material is in the elastic range, i.e. the stress state is admissible, and the analysis can continue to the next step.

If the trial stress satisfies the condition (5.12), for at least one yield surface, then the response is assumed to be elastoplastic. Note that, when the trial stress satisfies (5.12) for several yield surfaces, this does not necessarily imply that all those yield surfaces are active. According to Kuhn-Tuker conditions, an active yield surface should have a positive plastic multiplier. In case of an inelastic response, the algorithm enters a trial-error procedure to find all active mechanisms, plastic multipliers and the final updated state of stress and hardening parameters.

The detailed integration algorithm, for the case of plastic deformation, is presented in Flowchart 5-2. The iteration starts with the assumption that all the yield surfaces satisfying (5.12) are active. The updated state of stress and state parameters, i.e. $\left(\sigma_{ij}\right)_{n+1}$ and κ_{n+1}, are then found by a global iterative procedure (superscript s) within which a local iteration scheme is embedded (superscript m). Before starting the iterative loop, the initial value for the updated stress state is set to be the elastic trial stress, initial plastic multipliers are considered to be zero and the updated hardening parameters are equal to their values at step n. Using the generalized trapezoidal rule, at the global iteration level, the flow and hardening rules can be rewritten as follows

$$\left(\dot{\varepsilon}_{ij}^{p}\right)_{n+1}^{s+1} = \sum_{\beta} \dot{\lambda}_{\beta}^{s} \left((1-\omega) \left(\frac{\partial Q_{\beta}}{\partial \sigma_{ij}} \right)_{n} + \omega \left(\frac{\partial Q_{\beta}}{\partial \sigma_{ij}} \right)_{n+1}^{s} \right) \qquad (5.13)\text{a}$$

$$\left(\kappa_{n+1}^{s+1}\right)_\beta = \left(\kappa_n\right)_\beta + \dot{\lambda}_\beta^s \frac{\partial \kappa_\beta}{\partial \varepsilon_{ij}^p}\left((1-\omega)\left(\frac{\partial Q_\beta}{\partial \sigma_{ij}}\right)_n + \omega\left(\frac{\partial Q_\beta}{\partial \sigma_{ij}}\right)_{n+1}^s\right) \tag{5.13)b}$$

$$\left(\sigma_{ij}\right)_{n+1}^{s+1} = \left(\sigma_{ij}\right)_n + D_{ijkl}^e\left(\left(\dot{\varepsilon}_{kl}\right)_{n+1} - \left(\dot{\varepsilon}_{kl}^p\right)_{n+1}^{s+1}\right) \tag{5.13)c}$$

The loop for the global iteration starts by calculating the plastic strain, the updated hardening parameters and the stress state viz. (5.13), based on the state variables at step n, and $n+1$ at global iteration $s=0$. Then, the updated values are checked in accordance with the Kuhn-Tucker conditions. If stress state is at the intersection of all the active yield surfaces, i.e. $F_\beta\left(\left(\sigma_{ij}\right)_{n+1}^{s+1}, \left(\kappa_{n+1}^{s+1}\right)_\beta\right) = 0$, the iteration process is complete for the current set of active mechanisms. A second check should be done on the positivity of all the plastic multipliers, i.e. $\dot{\lambda}_\beta^s > 0$. A negative value of a plastic multiplier means that the corresponding mechanism should be deactivated. The set of active mechanisms should then be revised and the whole process should be repeated with the new updated set.

If the stress state is not at the intersection of the active yield surfaces at the level of global iteration, the algorithm enters the local iteration process. Before the start of local iterations, all derivatives required for step $(n+1)$ are calculated based on the state of stress at the current global iteration. The local iteration loop is terminated when the stress state satisfies the equations of all active yield surfaces. The updated stress and plastic multipliers are then fed back to the global iteration process. The state of stress and hardening parameters are updated at the new global iteration $s+1$, and the first Kuhn-

Tuker condition is checked for all the active mechanisms. The global iteration loop is terminated only when the updated state of stress is at the intersection of all active yield surfaces and all plastic multipliers are positive, otherwise the iteration will either update the set of active mechanism or reenter the local iteration loop.

To update the plastic multipliers in the local iteration loop the following relations are used

$$\dot{\lambda}_{\beta}^{s,m+1} = \dot{\lambda}_{\beta}^{s,m} + \frac{F_{\beta}\left(\left(\sigma_{ij}\right)_{n+1}^{s,m},\left(\kappa_{\beta}\right)_{n+1}^{s,m}\right)}{\left(H_{\beta}^{e}\right)_{n+1}^{s}+\left(H_{\beta}^{p}\right)_{n+1}^{s}} \tag{5.14a}$$

$$\left(H_{\beta}^{e}\right)_{n+1}^{s} = \left(\frac{\partial F_{\beta}}{\partial \sigma_{ij}}\right)_{n+1}^{s} D_{ijkl}^{e}\left(\left(1-\omega\right)\left(\frac{\partial Q_{\beta}}{\partial \sigma_{kl}}\right)_{n} + \omega\left(\frac{\partial Q_{\beta}}{\partial \sigma_{kl}}\right)_{n+1}^{s}\right) \tag{5.14b}$$

$$\left(H_{\beta}^{p}\right)_{n+1}^{s} = -\left(\frac{\partial F_{\beta}}{\partial \kappa_{\beta}}\right)_{n+1}^{s}\left(\frac{\partial \kappa_{\beta}}{\partial \varepsilon_{ij}^{p}}\right)\left(\left(1-\omega\right)\left(\frac{\partial Q_{\beta}}{\partial \sigma_{ij}}\right)_{n} + \omega\left(\frac{\partial Q_{\beta}}{\partial \sigma_{ij}}\right)_{n+1}^{s}\right) \tag{5.14c}$$

The elastoplastic operator D_{ijkl}^{ep} can be calculated based on Koiter's postulate for the updated state parameters, i.e. $\left(\sigma_{ij},\kappa\right)_{n+1}$. The consistency condition and the flow rule for all the active mechanisms, together with Hooke's law, are used in the derivation of this operator (Pasternack and Timmerman 1986). For the case of two active mechanisms, as presented in Chapter 3, the constitutive matrix can be expressed in the form

$$D_{ijkl}^{ep} = D_{ijkl}^{e} - \frac{D_{ijkl}^{e}\dfrac{\partial Q_1}{\partial \sigma_{kl}}\left(N_1\right)_{ij} D_{ijkl}^{e}}{H^{ep}} - \frac{D_{ijkl}^{e}\dfrac{\partial Q_2}{\partial \sigma_{kl}}\left(N_2\right)_{ij} D_{ijkl}^{e}}{H^{ep}} \tag{5.15}$$

where

$$H_{\beta}^{p} = -\frac{\partial F_{\beta}}{\partial \kappa_{\beta}} \frac{\dot{\kappa}_{\beta}}{\dot{\lambda}_{\beta}} \quad ; \quad H_{\beta\gamma}^{e} = \frac{\partial F_{\beta}}{\partial \sigma_{ij}} D_{ijkl}^{e} \frac{\partial Q_{\gamma}}{\partial \sigma_{kl}} \tag{5.16}$$

$$\left(N_{\beta}\right)_{ij} = \left(H_{\gamma\gamma}^{e} + H_{\gamma}^{p}\right) \frac{\partial F_{\beta}}{\partial \sigma_{ij}} - H_{\beta\gamma}^{e} \frac{\partial F_{\gamma}}{\partial \sigma_{ij}} \quad ; \quad \beta, \gamma = 1,2$$

5.4 Numerical Simulations of Undrained Behavior of Sand

This section demonstrates the applicability of the constitutive relation proposed in Chapter 3, to model the mechanical characteristics of anisotropic granular materials. The employed integration scheme is the one presented in section 5.3 with $\omega = 0.5$, which is unconditionally stable and highly accurate. Simulations presented here involve undraind hollow cylinder tests on transversely isotropic sand samples. The discussion on the testing equipment and procedures were presented in Chapter 2.

Yoshimine et al. (1998) investigated the anisotropic behavior of Toyora sand with $D_r = 39 - 41\%$. The results of undrained hollow cylinder experiments on samples tested at different values of α are presented in Fig 5-3. The results of numerical simulations are also given in the same figure. The directional dependency is considered in η_f, η_c as well as the hardening parameter B, as shown in Fig 5-4. The material properties employed in the simulations are listed in Table 5-1. The notation used is consistent with eq. (4.8). Note that in order to identify the material parameters properly, a more comprehensive experimental investigation is required and the material parameters presented in Table 5-1 may not be accurate enough. However, the general trends in the simulated behavior are in a good agreement with the observed behavior.

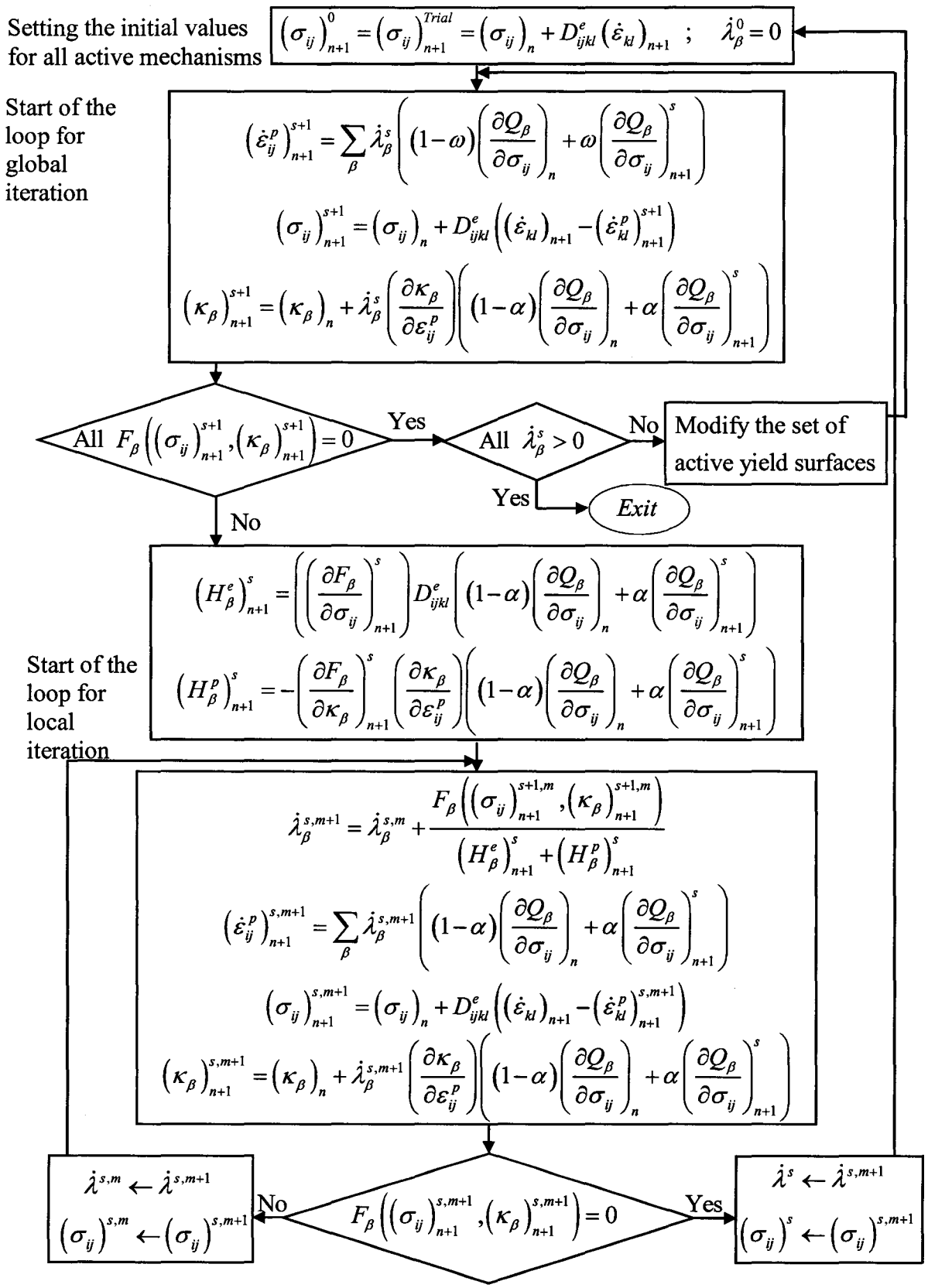
Setting the initial values for all active mechanisms
$\left(\sigma_{ij}\right)_{n+1}^{0}=\left(\sigma_{ij}\right)_{n+1}^{Trial}=\left(\sigma_{ij}\right)_{n}+D_{ijkl}^{e}\left(\dot{\varepsilon}_{kl}\right)_{n+1}\ ;\quad \dot{\lambda}_{\beta}^{0}=0$
Start of the loop for global iteration
$\left(\dot{\varepsilon}_{ij}^{p}\right)_{n+1}^{s+1}=\sum_{\beta}\dot{\lambda}_{\beta}^{s}\left((1-\omega)\left(\frac{\partial Q_{\beta}}{\partial\sigma_{ij}}\right)_{n}+\omega\left(\frac{\partial Q_{\beta}}{\partial\sigma_{ij}}\right)_{n+1}^{s}\right)$
$\left(\sigma_{ij}\right)_{n+1}^{s+1}=\left(\sigma_{ij}\right)_{n}+D_{ijkl}^{e}\left(\left(\dot{\varepsilon}_{kl}\right)_{n+1}-\left(\dot{\varepsilon}_{kl}^{p}\right)_{n+1}^{s+1}\right)$
$\left(\kappa_{\beta}\right)_{n+1}^{s+1}=\left(\kappa_{\beta}\right)_{n}+\dot{\lambda}_{\beta}^{s}\left(\frac{\partial\kappa_{\beta}}{\partial\varepsilon_{ij}^{p}}\right)\left((1-\alpha)\left(\frac{\partial Q_{\beta}}{\partial\sigma_{ij}}\right)_{n}+\alpha\left(\frac{\partial Q_{\beta}}{\partial\sigma_{ij}}\right)_{n+1}^{s}\right)$
All $F_{\beta}\left(\left(\sigma_{ij}\right)_{n+1}^{s+1},\left(\kappa_{\beta}\right)_{n+1}^{s+1}\right)=0$
Yes
All $\dot{\lambda}_{\beta}^{s}>0$
No
Modify the set of active yield surfaces
Yes
Exit
No
$\left(H_{\beta}^{e}\right)_{n+1}^{s}=\left(\left(\frac{\partial F_{\beta}}{\partial\sigma_{ij}}\right)_{n+1}^{s}\right)D_{ijkl}^{e}\left((1-\alpha)\left(\frac{\partial Q_{\beta}}{\partial\sigma_{ij}}\right)_{n}+\alpha\left(\frac{\partial Q_{\beta}}{\partial\sigma_{ij}}\right)_{n+1}^{s}\right)$
$\left(H_{\beta}^{p}\right)_{n+1}^{s}=-\left(\frac{\partial F_{\beta}}{\partial\kappa_{\beta}}\right)_{n+1}^{s}\left(\frac{\partial\kappa_{\beta}}{\partial\varepsilon_{ij}^{p}}\right)\left((1-\alpha)\left(\frac{\partial Q_{\beta}}{\partial\sigma_{ij}}\right)_{n}+\alpha\left(\frac{\partial Q_{\beta}}{\partial\sigma_{ij}}\right)_{n+1}^{s}\right)$
Start of the loop for local iteration
$\dot{\lambda}_{\beta}^{s,m+1}=\dot{\lambda}_{\beta}^{s,m}+\frac{F_{\beta}\left(\left(\sigma_{ij}\right)_{n+1}^{s+1,m},\left(\kappa_{\beta}\right)_{n+1}^{s+1,m}\right)}{\left(H_{\beta}^{e}\right)_{n+1}^{s}+\left(H_{\beta}^{p}\right)_{n+1}^{s}}$
$\left(\dot{\varepsilon}_{ij}^{p}\right)_{n+1}^{s,m+1}=\sum_{\beta}\dot{\lambda}_{\beta}^{s,m+1}\left((1-\alpha)\left(\frac{\partial Q_{\beta}}{\partial\sigma_{ij}}\right)_{n}+\alpha\left(\frac{\partial Q_{\beta}}{\partial\sigma_{ij}}\right)_{n+1}^{s}\right)$
$\left(\sigma_{ij}\right)_{n+1}^{s,m+1}=\left(\sigma_{ij}\right)_{n}+D_{ijkl}^{e}\left(\left(\dot{\varepsilon}_{kl}\right)_{n+1}-\left(\dot{\varepsilon}_{kl}^{p}\right)_{n+1}^{s,m+1}\right)$
$\left(\kappa_{\beta}\right)_{n+1}^{s,m+1}=\left(\kappa_{\beta}\right)_{n}+\dot{\lambda}_{\beta}^{s,m+1}\left(\frac{\partial\kappa_{\beta}}{\partial\varepsilon_{ij}^{p}}\right)\left((1-\alpha)\left(\frac{\partial Q_{\beta}}{\partial\sigma_{ij}}\right)_{n}+\alpha\left(\frac{\partial Q_{\beta}}{\partial\sigma_{ij}}\right)_{n+1}^{s}\right)$
$\dot{\lambda}^{s,m}\leftarrow\dot{\lambda}^{s,m+1}$
$\left(\sigma_{ij}\right)^{s,m}\leftarrow\left(\sigma_{ij}\right)^{s,m+1}$
No
$F_{\beta}\left(\left(\sigma_{ij}\right)_{n+1}^{s,m+1},\left(\kappa_{\beta}\right)_{n+1}^{s,m+1}\right)=0$
Yes
$\dot{\lambda}^{s}\leftarrow\dot{\lambda}^{s,m+1}$
$\left(\sigma_{ij}\right)^{s}\leftarrow\left(\sigma_{ij}\right)^{s,m+1}$

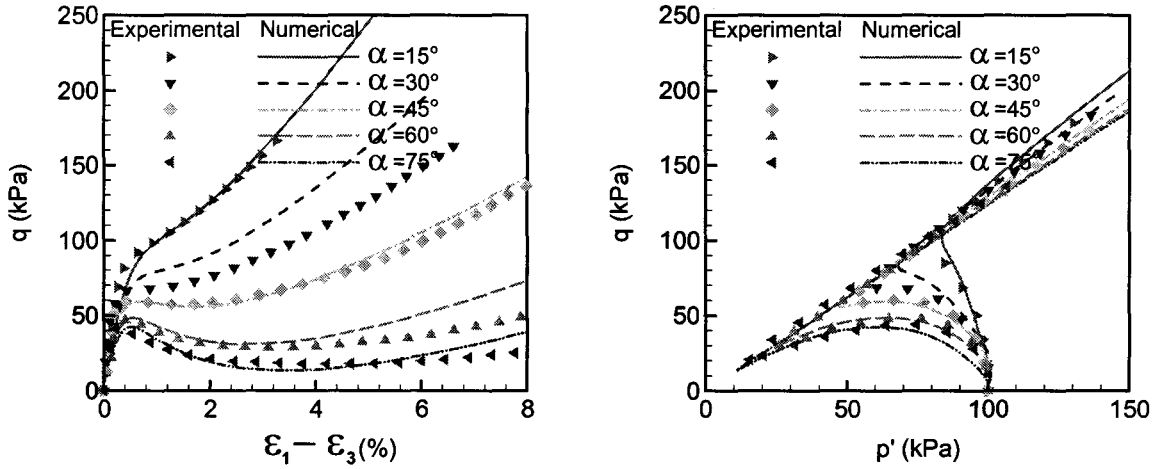

Fig 5-3 Comparison of experimental data reported by Yoshimine et al. (1998) on Toyoura sand with the simulation results

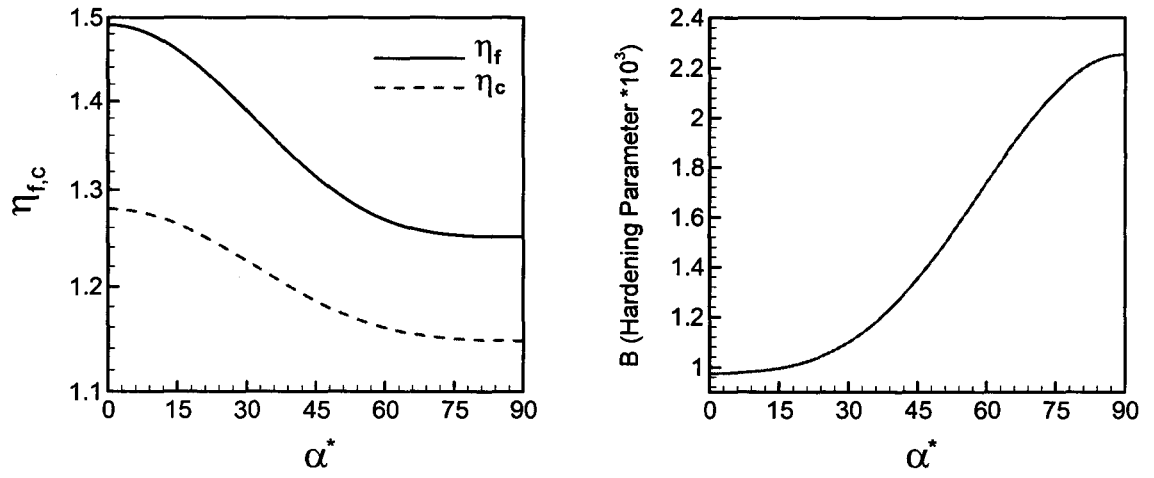

Fig 5-4 Variation of η_f, η_c and B with the loading angle

Table 5-1 Material parameters for the simulations of mechanical response of Toyora sand

$E_1 = 25.0$ kPa	$\overline{\eta}_f = 1.28$	$\overline{\eta}_c = 1.1668$	$\overline{B} = 0.0015965$	$\overline{T} = 0.0$ kPa
$E_3 = 50.0$ kPa	$A_1 = 0.05585$	$A_1 = 0.03536$	$A_1 = -0.44077$	$A_1 = 0.0$
$\nu_{12} = 0.3$	$a_1 = 10.527$	$a_1 = 14.25$	$a_1 = 0.6291$	
$\nu_{13} = 0.2$	$a_2 = a_3 = ... = 0$	$a_2 = a_3 = ... = 0$	$a_2 = a_3 = ... = 0$	$C = 1.0$ kPa
$G_{13} = 60.0$ kPa				$\lambda = 0.00475$
				$\kappa = 0.002$

Similar experimental data has been reported by Vaid et al. (2001) on the anisotropic behavior of loose Fraser River sand ($D_r = 30\%$). The experimental results of undrained hollow cylinder tests are presented in Fig 5-5. The results of numerical simulations are also provided in the same figure. Fig 5-6 shows the directional dependency of η_f, η_c and B for Fraser River sand, while all the material properties are listed in Table 5-2. Once again, the predicted behavior is in a good agreement with the general trends in the observed behavior.

In the next step of the numerical analyses, the constitutive model described in Chapter 3 was programmed in a UMAT subroutine for ABAQUS finite element software. The subroutine employed the integration scheme described in Section 5.3. The next section is focused on the assessment of bearing capacity of a shallow foundation in a transversely isotropic granular medium and the validation of the model by a comparison with the experimental data.

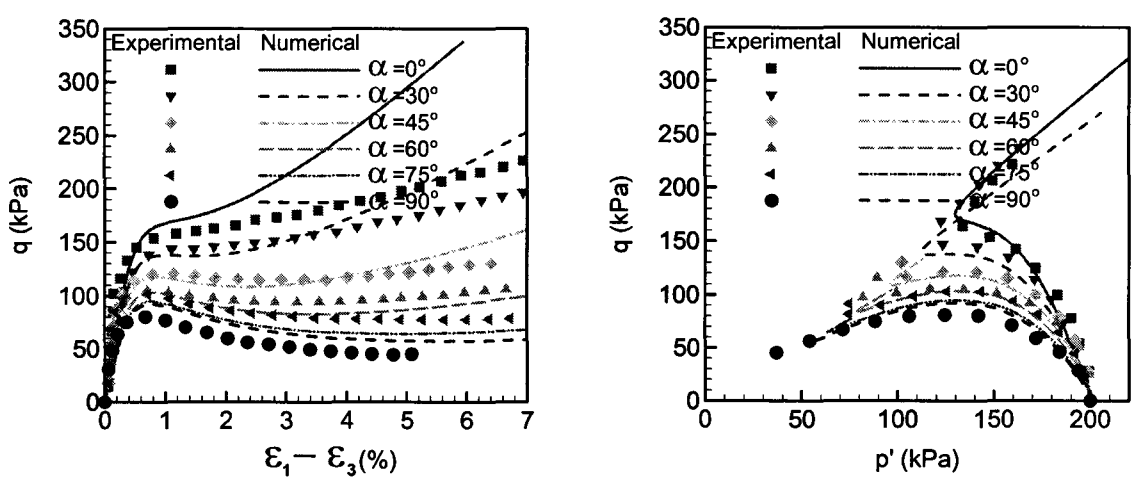

Fig 5-5 Comparison of experimental data reported by Vaid et al. (2001) on Fraser River sand with the simulation results

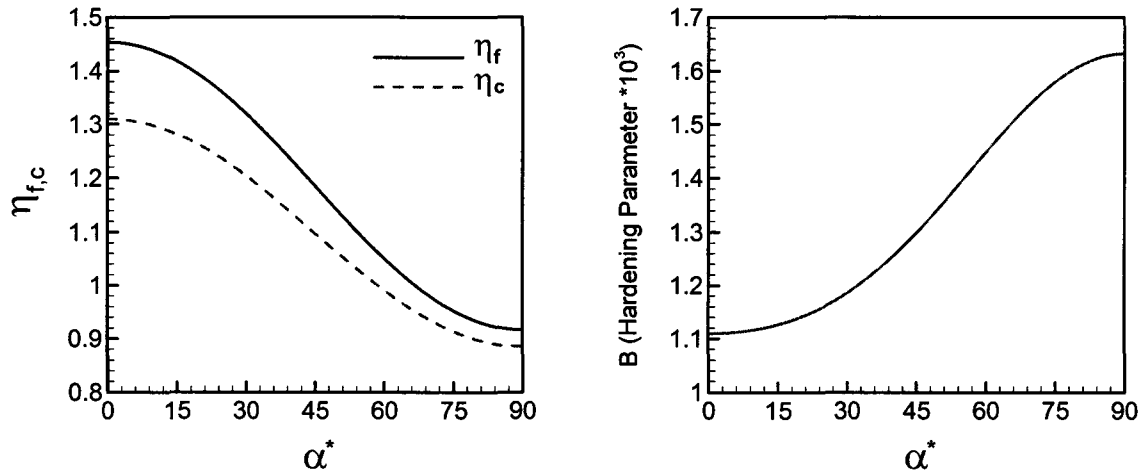

Fig 5-6 Variation of η_f, η_c and B with the loading angle

Table 5-2 Material parameters for the simulations of mechanical response of Fraser River sand

$E_1 = 46.0$ kPa	$\overline{\eta}_f = 1.09577$	$\overline{\eta}_c = 1.02694$	$\overline{B} = 0.0013937$	$\overline{T} = 0.0$ kPa
$E_3 = 69.0$ kPa	$A_1 = 0.21199$	$A_1 = 0.178759$	$A_1 = -0.192248$	$A_1 = 0.0$
$\nu_{12} = 0.35$	$a_1 = a_2 = ... = 0$	$a_1 = a_2 = ... = 0$	$a_1 = a_2 = ... = 0$	
$\nu_{13} = 0.36$				$C = 1.0$ kPa
$G_{13} = 60.0$ kPa				$\lambda = 0.00475$
				$\kappa = 0.002$

5.5 Numerical Analysis of Shallow Foundation in a Transversely Isotropic Granular Medium

The FE discretization used in the simulations is shown in Fig 5-7a. The mesh employed 860 eight-noded quadrilateral elements with reduced Gaussian integration. In order to assess the sensitivity of the solution to discretization, a coarser mesh (226 elements) was also employed, as shown in Fig 5-7b. Note that although the meshes were symmetric with respect to the centerline of the footing, the resulting stress/displacement fields were not, due to anisotropy of the material. The dimensions of the FE model were the same as those of the experimental setup (see Chapter 2). The footing was assumed as rigid relative to the soil (elastic material; E=10^4MPa). The loading process consisted of applying vertical displacement at the top midpoint of the footing while allowing for the in-plane rotation.

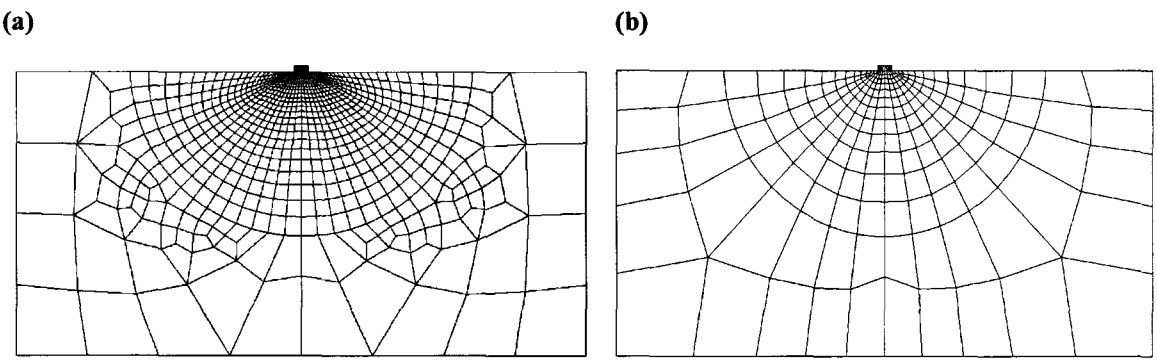

Fig 5-7 Finite element discretization for the analyzed problem; (a) fine mesh and (b) coarse mesh

Fig 5-8 shows the load-displacement characteristics of the footing for the deposition angles of $\alpha = 0^\circ$ and $\alpha = 90^\circ$. Two sets of predictions are provided, viz. with

and without taking into account the localized deformation mode. In the former case, the simulations employ the averaged constitutive law (3.60), while in the latter, a homogeneous deformation mode is enforced locally (i.e. no localization). It is evident that without invoking strain-softening characteristics associated with the localized deformation, the numerical predictions are quite poor. In fact, the bearing capacity is significantly overestimated and the predicted values are almost the same for both directions of deposition, which contradicts the experimental evidence. On the other hand, the simulations incorporating the strain-softening mode result in predictions that are fairly consistent with experimental measurements for both orientations considered. The issue of mesh sensitivity of the solution is addressed in Fig 5-9, which shows two sets of simulations for $\alpha = 0^{\circ}$, corresponding to two different discretizations, as shown in Fig 5-7. Clearly, the results are virtually the same, which is consistent with the notion of mesh-objectivity, as originally addressed in the article by Pietruszczak and Mroz (1981).

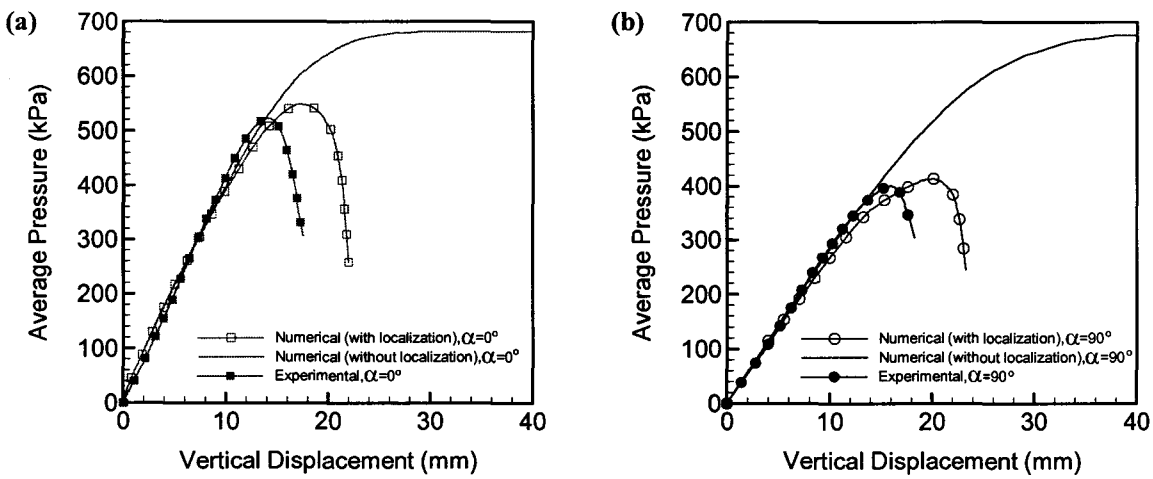

Fig 5-8 Load - displacement characteristics of the footing for $\alpha = 0^{\circ}$ and $\alpha = 90^{\circ}$ (Note: numerical simulations are with/without invoking the localized deformation mode)

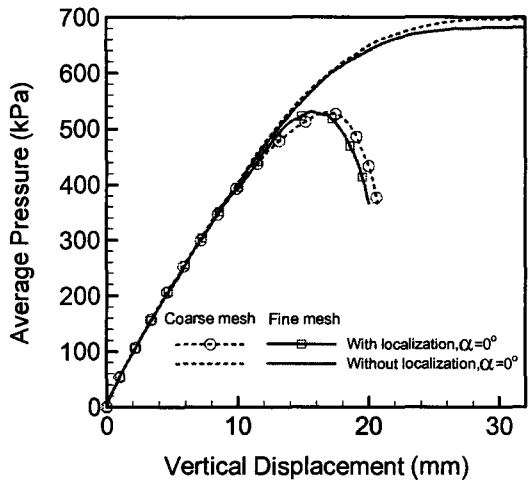

Fig 5-9 Mesh sensitivity analysis ($\alpha = 0^{o}$)

Fig 5-10 gives a more comprehensive picture of the evolution of mechanical characteristics with the angle of deposition. The results, once again, correspond to the standard approach (without localization) and the one incorporating the strain-softening mode. For the latter case, the predicted load-displacement response is again fairly consistent with the experimental data presented in Fig 5-10c.

For completeness, Fig 5-11 shows the load-displacement characteristics of the footing for the deposition angles of $\alpha = 30^{o}$, $\alpha = 60^{o}$ and $\alpha = 45^{o}$. The conclusions are similar to those derived from the results in Fig 5-8, i.e. incorporation of localized deformation mode is essential for obtaining reliable predictions. Furthermore, it is noted that for orientations of $\alpha = 30^{o}, \alpha = 45^{o}$ and $\alpha = 60^{o}$, the in-plane rotation of the footing was predicted from the early stages of the loading process. This is consistent with the experimental data as reported in Chapter 2. Also, there was no indication of any global localization mechanism developing at the macroscale. Instead, a diffused mode of failure was predicted with damage zones adjacent to the footing.

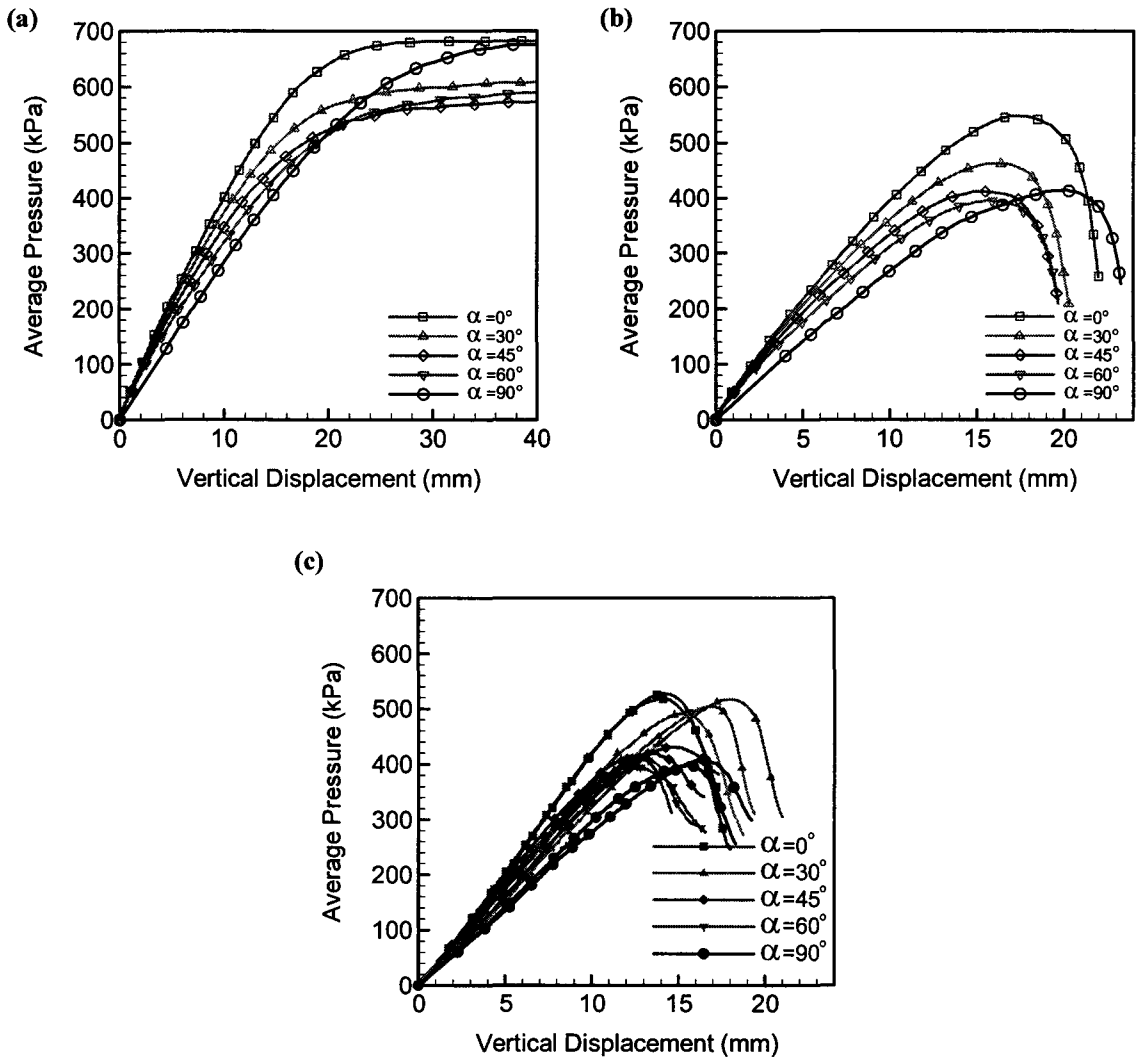

Fig 5-10 Load - displacement characteristics of the footing for different values of α (a) without localization treatment, (b) with localization treatment and (c) experimental results

The issue of variation of ultimate bearing capacity with the angle of deposition is addressed in Fig 5-12. Clearly, the numerical predictions are again in a good agreement with the experimental results.

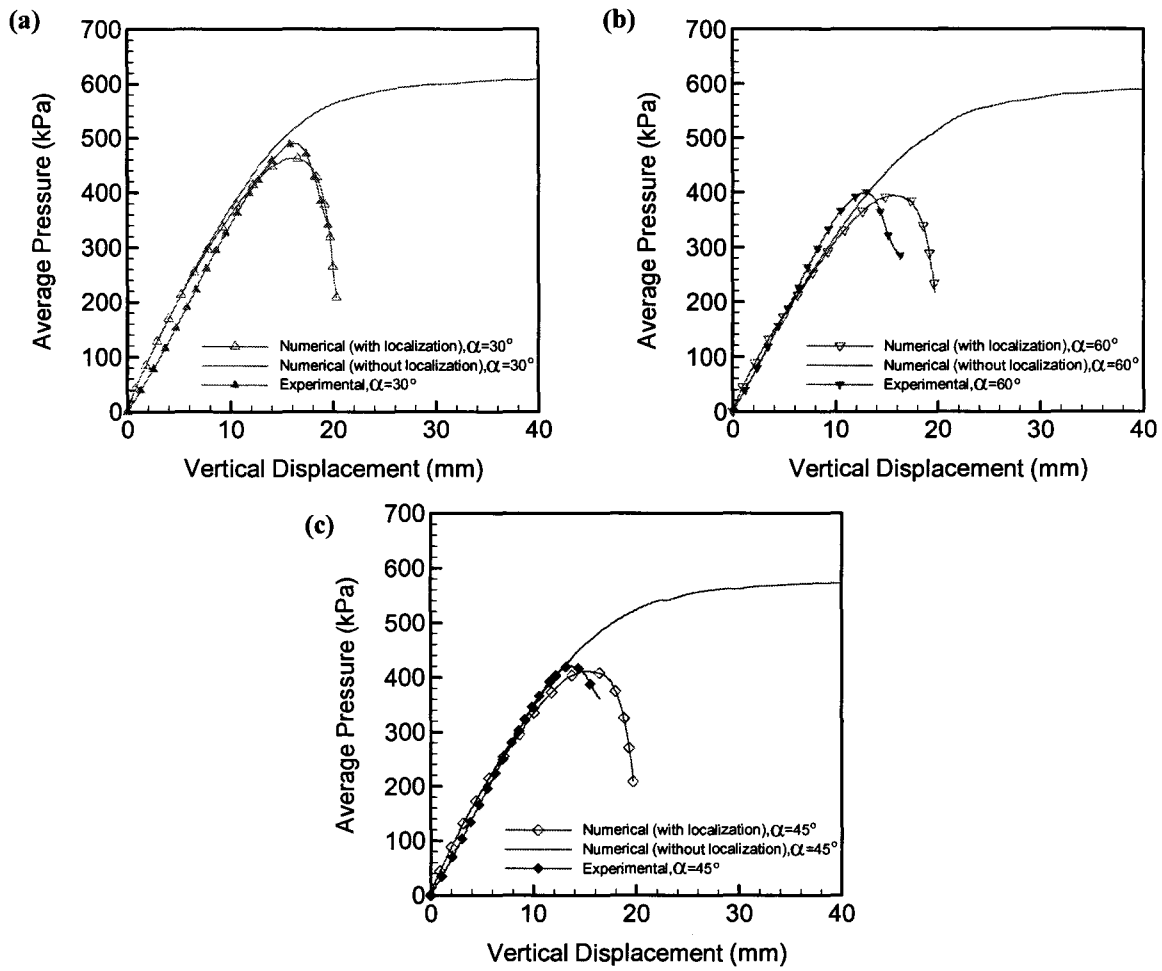

Fig 5-11 Load - displacement characteristics of the footing for $\alpha = 30^{\circ}$, $\alpha = 60^{\circ}$ and $\alpha = 45^{\circ}$

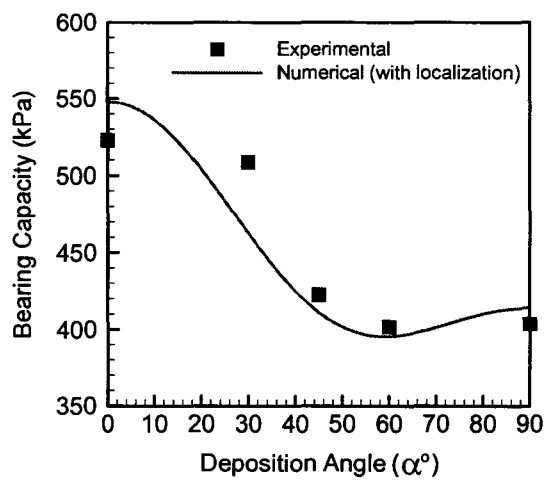

Fig 5-12 Variation of the bearing capacity with α ; comparison of experimental and numerical results

5.5.2 Parametric Study

The simulations presented in the previous section were carried out using the deviatoric hardening mechanism, as described in Chapter 3. The analysis was carried out with and without taking into account the localized deformation mode. In this section, parametric studies are performed to examine the influence of various assumptions embedded in the model.

The incorporation of the associated flow rule was motivated by the fact that at low confining pressures, which are representative of conditions in the scaled-model tests, a progressive dilation has been recorded. The latter is particularly evident in the context of direct shear tests, Fig 2-5b. In triaxial tests, the initial compaction (Fig 2-13b, Fig 2-14b and Fig 2-15b) is associated primarily with elastic deformation, while the dilation in the later stages of these tests is attributed to plastic deformations. It should be mentioned that, in general, the use of a non-associated flow rule for materials exhibiting a high friction angle leads to numerical instabilities. This may occur even if some very robust solution techniques are employed. The problem is addressed in more details in the articles by de Borst and Vermeer (1984) and Yin et al. (2001).

In the parametric studies reported here, a series of simulations were carried out first to investigate the significance of considering the hardening behavior on the prediction of bearing capacity. These involved simulations incorporating perfect-plasticity, with and without the provision for localized deformation. Note that the perfectly-plastic formulation corresponds to $\beta = 1$ in eq. (3.20), so that the yield function is assumed to coincide with the Mohr-Coulomb failure criterion. The predicted values of

bearing capacity, together with the experimental ones are shown in Fig 5-13. It appears that consideration of the hardening in the elastoplastic constitutive model has an insignificant effect on the assessment of the ultimate load.

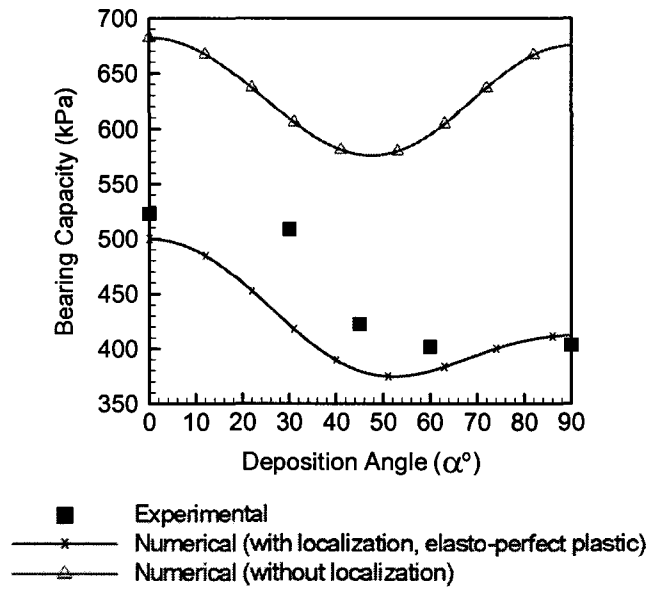

Fig 5-13 Variation of the bearing capacity with α ; comparison of experimental and numerical results assuming an elasto-perfect plastic behavior

Three additional sets of simulations were carried out to examine the significance of incorporating the anisotropic effects. First, it was assumed that $\eta_f = \min(\eta_f)$ for all orientations, which led to underestimating the ultimate load. The second set involved $\eta_f = \text{mean}(\eta_f)$, in which case the predicted bearing capacity was higher than the measured values. The last case corresponded to $\eta_f = \max(\eta_f)$, and the resulting bearing capacity was significantly overestimated.

Fig 5-14 summarizes the results of all the parametric studies. The results clearly indicate the importance of accounting for inherent anisotropy and strain localization in order to obtain reliable assessments of the bearing capacity. The best estimate of the ultimate load is obtained by incorporating the most general framework.

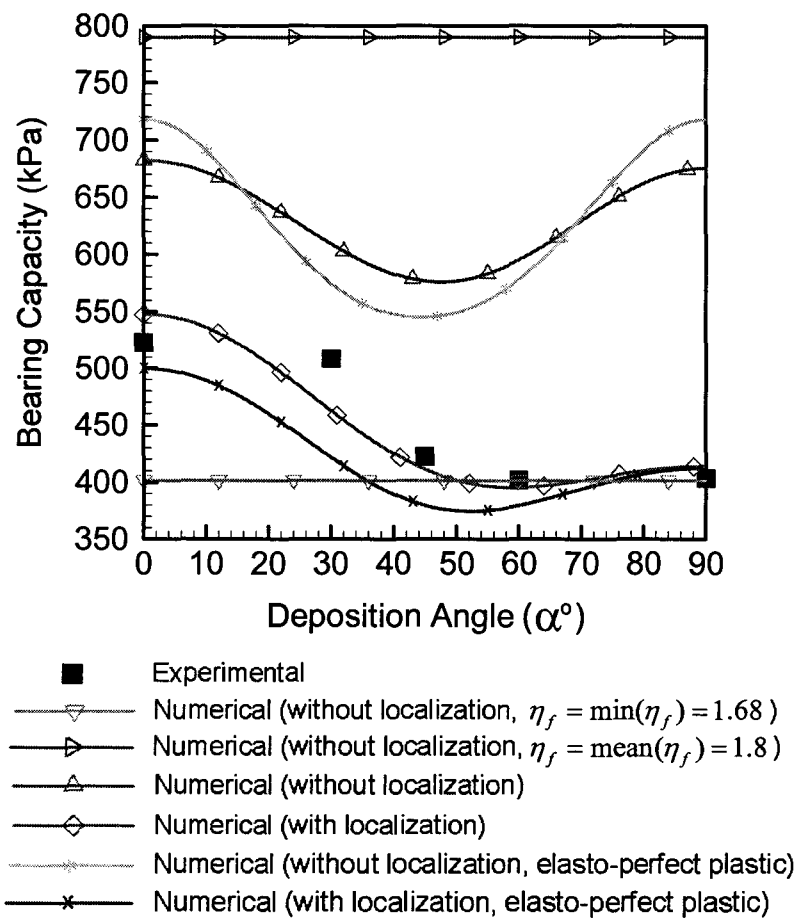

Fig 5-14 Variation of the bearing capacity with α ; comparison of experimental and numerical results

By examining the other predictions, it is evident that accounting for progressive development of localized deformation is of more importance than incorporating strain-

hardening effects prior to the onset of localization. Also, an adequate description of anisotropy seems essential in order to obtain a reliable assessment, as the variation of bearing capacity with the angle of deposition is quite significant. Finally, it is noted that in the engineering design the effects of both anisotropy and localized deformation are commonly neglected. In this case, the predictions are, in general, inadequate as the solution corresponding to the mean value of η_f significantly overestimates the bearing capacity, while the prediction employing $\min(\eta_f)$ gives a conservative estimate.

Appendix I

The derivation of equation (5.6):

The new state of stress should be on the updated yield surface, i.e. $F\left(\left(\sigma_{ij}\right)_{n+1}^{s,m+1},\kappa_{n+1}^{s,m+1}\right)=0$. Thus,

$$
\begin{aligned}
F\left(\left(\sigma_{ij}\right)_{n+1}^{s,m+1},\kappa_{n+1}^{s,m+1}\right) &= F\left(\left(\sigma_{ij}\right)_{n+1}^{s,m},\kappa_{n+1}^{s,m}\right)+\left(\left(\frac{\partial F}{\partial \sigma_{ij}}\right)^{s}_{n+1}\right)\left(\left(\dot{\sigma}_{ij}\right)_{n+1}^{s,m+1}-\left(\dot{\sigma}_{ij}\right)_{n+1}^{s,m}\right)+\left(\left(\frac{\partial F}{\partial \kappa}\right)^{s}_{n+1}\right)\left(\dot{\kappa}_{n+1}^{s,m+1}-\dot{\kappa}_{n+1}^{s,m}\right)\\
&= F\left(\left(\sigma_{ij}\right)_{n+1}^{s,m},\kappa_{n+1}^{s,m}\right)+\left(\left(\frac{\partial F}{\partial \sigma_{ij}}\right)^{s}_{n+1}\right)\left(D^{e}_{ijkl}\left(\dot{\varepsilon}_{n+1}-\left(\dot{\varepsilon}^{p}_{n+1}\right)^{s,m+1}\right)-D^{e}_{ijkl}\left(\dot{\varepsilon}_{n+1}-\left(\dot{\varepsilon}^{p}_{n+1}\right)^{s,m}\right)\right)\\
&\quad+\left(\left(\frac{\partial F}{\partial \kappa}\right)^{s}_{n+1}\right)\left(\dot{\lambda}^{s,m+1}\left(\frac{\partial \kappa}{\partial \varepsilon^{p}}\right)\left((1-\omega)\left(\frac{\partial Q}{\partial \sigma_{ij}}\right)_{n}+\omega\left(\frac{\partial Q}{\partial \sigma_{ij}}\right)^{s}_{n+1}\right)\right.\\
&\qquad\left.-\dot{\lambda}^{k,m}\left(\frac{\partial \kappa}{\partial \varepsilon^{p}}\right)\left((1-\omega)\left(\frac{\partial Q}{\partial \sigma_{ij}}\right)_{n}+\omega\left(\frac{\partial Q}{\partial \sigma_{ij}}\right)^{s}_{n+1}\right)\right)\\
&= F\left(\left(\sigma_{ij}\right)_{n+1}^{s,m},\kappa_{n+1}^{s,m}\right)+\left(\left(\frac{\partial F}{\partial \sigma_{ij}}\right)^{s}_{n+1}\right)D^{e}_{ijkl}\left(\dot{\lambda}^{s,m}-\dot{\lambda}^{s,m+1}\right)\left((1-\omega)\left(\frac{\partial Q}{\partial \sigma_{kl}}\right)_{n}+\omega\left(\frac{\partial Q}{\partial \sigma_{kl}}\right)^{s}_{n+1}\right)\\
&\quad+\left(\left(\frac{\partial F}{\partial \kappa}\right)^{s}_{n+1}\right)\left(\dot{\lambda}^{s,m+1}-\dot{\lambda}^{s,m}\right)\left(\frac{\partial \kappa}{\partial \varepsilon^{p}}\right)\left((1-\omega)\left(\frac{\partial Q}{\partial \sigma_{kl}}\right)_{n}+\omega\left(\frac{\partial Q}{\partial \sigma_{kl}}\right)^{s}_{n+1}\right)\\
&= 0
\end{aligned}
$$

$$
\dot{\lambda}^{k,m+1}=\dot{\lambda}^{k,m}+\frac{F\left(\left(\sigma_{ij}\right)_{n+1}^{k,m},\kappa_{n+1}^{k,m}\right)}{\left(H^{e}\right)^{k}_{n+1}+\left(H^{p}\right)^{k}_{n+1}} \tag{5.6)a}
$$

$$
\left(H^{e}\right)^{s}_{n+1}=\left(\left(\frac{\partial F}{\partial \sigma_{ij}}\right)^{s}_{n+1}\right)D^{e}_{ijkl}\left((1-\omega)\left(\frac{\partial Q}{\partial \sigma_{kl}}\right)_{n}+\omega\left(\frac{\partial Q}{\partial \sigma_{kl}}\right)^{s}_{n+1}\right) \tag{5.6)b}
$$

$$
\left(H^{p}\right)^{s}_{n+1}=-\left(\left(\frac{\partial F}{\partial \kappa}\right)^{s}_{n+1}\right)^{T}\left(\frac{\partial \kappa}{\partial \varepsilon^{p}}\right)^{T}\left((1-\omega)\left(\frac{\partial Q}{\partial \sigma_{ij}}\right)_{n}+\omega\left(\frac{\partial Q}{\partial \sigma_{ij}}\right)^{s}_{n+1}\right) \tag{5.6)c}
$$

Appendix II

The derivation of equation (5.14):

The updated state should be at the intersection of all the active yield surfaces, i.e. $F_\beta\left(\left(\sigma_{ij}\right)_{n+1}^{s,m+1},\left(\kappa_\beta\right)_{n+1}^{s,m+1}\right)=0$. Thus,

$$
\begin{aligned}
F_\beta\left(\left(\sigma_{ij}\right)_{n+1}^{s,m+1},\left(\kappa_\beta\right)_{n+1}^{s,m+1}\right) &= F_\beta\left(\left(\sigma_{ij}\right)_{n+1}^{s,m},\left(\kappa_\beta\right)_{n+1}^{s,m}\right)+dF_\beta\left(\left(\sigma_{ij}\right)_{n+1}^{s,m+1},\left(\kappa_\beta\right)_{n+1}^{s,m+1}\right)\\
&= F_\beta\left(\left(\sigma_{ij}\right)_{n+1}^{s,m},\left(\kappa_\beta\right)_{n+1}^{s,m}\right)+\left(\frac{\partial F_\beta}{\partial\sigma_{ij}}\right)_{n+1}^{s}\left(\left(\sigma_{ij}\right)_{n+1}^{s,m+1}-\left(\sigma_{ij}\right)_{n+1}^{s,m}\right)+\left(\frac{\partial F_\beta}{\partial\kappa_\beta}\right)_{n+1}^{s}\left(\left(\dot{\kappa}_\beta\right)_{n+1}^{s,m+1}-\left(\dot{\kappa}_\beta\right)_{n+1}^{s,m}\right)\\
&= F_\beta\left(\left(\sigma_{ij}\right)_{n+1}^{s,m},\left(\kappa_\beta\right)_{n+1}^{s,m}\right)+\left(\frac{\partial F_\beta}{\partial\sigma_{ij}}\right)_{n+1}^{s}\left(D_{ijkl}^{e}\left(\left(\dot{\varepsilon}_{kl}\right)_{n+1}-\left(\dot{\varepsilon}_{kl}^{p}\right)_{n+1}^{s,m+1}\right)-D_{ijkl}^{e}\left(\left(\dot{\varepsilon}_{kl}\right)_{n+1}-\left(\dot{\varepsilon}_{kl}^{p}\right)_{n+1}^{s,m}\right)\right)\\
&\quad+\left(\frac{\partial F_\beta}{\partial\kappa_\beta}\right)_{n+1}^{s}\left(\dot{\lambda}_\beta^{s,m+1}\left(\frac{\partial\kappa_\beta}{\partial\varepsilon_{ij}^{p}}\right)\left(\left(1-\omega\right)\left(\frac{\partial Q_\beta}{\partial\sigma_{ij}}\right)_{n}+\omega\left(\frac{\partial Q_\beta}{\partial\sigma_{ij}}\right)_{n+1}^{s}\right)\right.\\
&\quad\left.-\dot{\lambda}_\beta^{s,m}\left(\frac{\partial\kappa_\beta}{\partial\varepsilon_{ij}^{p}}\right)\left(\left(1-\omega\right)\left(\frac{\partial Q_\beta}{\partial\sigma_{ij}}\right)_{n}+\omega\left(\frac{\partial Q_\beta}{\partial\sigma_{ij}}\right)_{n+1}^{s}\right)\right)\\
&= F_\beta\left(\left(\sigma_{ij}\right)_{n+1}^{s,m},\left(\kappa_\beta\right)_{n+1}^{s,m}\right)+\left(\frac{\partial F_\beta}{\partial\sigma_{ij}}\right)_{n+1}^{s}D_{ijkl}^{e}\left(\dot{\lambda}_\beta^{s,m}-\dot{\lambda}_\beta^{s,m+1}\right)\left(\left(1-\omega\right)\left(\frac{\partial Q_\beta}{\partial\sigma_{kl}}\right)_{n}+\omega\left(\frac{\partial Q_\beta}{\partial\sigma_{kl}}\right)_{n+1}^{s}\right)\\
&\quad+\left(\frac{\partial F_\beta}{\partial\kappa_\beta}\right)_{n+1}^{s}\left(\dot{\lambda}_\beta^{s,m+1}-\dot{\lambda}_\beta^{s,m}\right)\left(\frac{\partial\kappa_\beta}{\partial\varepsilon_{ij}^{p}}\right)\left(\left(1-\omega\right)\left(\frac{\partial Q_\beta}{\partial\sigma_{ij}}\right)_{n}+\omega\left(\frac{\partial Q_\beta}{\partial\sigma_{ij}}\right)_{n+1}^{s}\right)\\
&= F_\beta\left(\left(\sigma_{ij}\right)_{n+1}^{s,m},\left(\kappa_\beta\right)_{n+1}^{s,m}\right)+\left(\dot{\lambda}_\beta^{s,m}-\dot{\lambda}_\beta^{s,m+1}\right)\left(\left(H_\beta^{e}\right)_{n+1}^{s}+\left(H_\beta^{p}\right)_{n+1}^{s}\right)=0
\end{aligned}
$$

$$
\dot{\lambda}_\beta^{s,m+1}=\dot{\lambda}_\beta^{s,m}+\frac{F_\beta\left(\left(\sigma_{ij}\right)_{n+1}^{s,m},\left(\kappa_\beta\right)_{n+1}^{s,m}\right)}{\left(H_\beta^{e}\right)_{n+1}^{s}+\left(H_\beta^{p}\right)_{n+1}^{s}} \qquad (5.14)\text{a}
$$

$$\left(H_{\beta}^{e}\right)_{n+1}^{s}=\left(\frac{\partial F_{\beta}}{\partial \sigma_{ij}}\right)_{n+1}^{s} D_{ijkl}^{e}\left((1-\omega)\left(\frac{\partial Q_{\beta}}{\partial \sigma_{kl}}\right)_{n}+\omega\left(\frac{\partial Q_{\beta}}{\partial \sigma_{kl}}\right)_{n+1}^{s}\right) \tag{5.14)b}$$

$$\left(H_{\beta}^{p}\right)_{n+1}^{s}=-\left(\frac{\partial F_{\beta}}{\partial \kappa_{\beta}}\right)_{n+1}^{s}\left(\frac{\partial \kappa_{\beta}}{\partial \varepsilon_{ij}^{p}}\right)\left((1-\omega)\left(\frac{\partial Q_{\beta}}{\partial \sigma_{ij}}\right)_{n}+\omega\left(\frac{\partial Q_{\beta}}{\partial \sigma_{ij}}\right)_{n+1}^{s}\right) \tag{5.14)c}$$

CHAPTER 6
CONCLUSIONS AND RECOMMENDATIONS

6.1 Summary and Conclusions

The study presented here includes both the experimental and numerical aspects and it provides a comprehensive insight into the mechanical response of anisotropic granular materials. The specific engineering problem addressed here was the assessment of the ultimate bearing capacity of shallow foundations in a transversely isotropic granular medium. The study comprised the experimental and numerical components both at the material and structural levels.

The experimental investigations were conducted on crushed limestone sand with elongated angular-shaped aggregates. To induce a distinct microstructure, a sand rain method was used for sample preparation which enabled uniform anisotropic specimens to be produced at the selected void ratio. The material tests involved direct shear, triaxial and hollow cylinder experiments and were aimed at examining the effects of inherent anisotropy on both the deformation and strength characteristics. A scaled foundation setup was designed and a series of scaled-model tests was carried out to examine the dependency of ultimate bearing capacity on the material fabric.

A general constitutive framework was outlined that describes the mechanical response of transversely isotropic frictional materials. The framework is based on multi-yield loci plasticity and accounts for salient features that include the notions of

compaction/ dilatancy, pressure sensitivity, hardening induced by both densification and plastic distortion, as well as anisotropy in strength and deformation characteristics. The general formulation incorporates a scalar anisotropy parameter which is defined as a projection of the microstructure orientation tensor on the loading direction. Given the limitations of the triaxial and hollow cylinder tests in identification of anisotropic material parameters, an innovative procedure was employed for the specification of strength at different angles of deposition. In this approach, the results of direct shear tests were re-interpreted in terms of critical plane framework in order to assess the values of strength parameters under triaxial conditions.

As a part of constitutive modeling, an implicit integration algorithm was developed to integrate the constitutive equations. The integration scheme employs Koiter's postulate for the specification of the tangent operator. The proposed anisotropic multi-yield surface model and the integration scheme were tested in simulations of undrianed behavior of sand in triaxial configuration.

The performance of the model and the material parameters were verified for stress trajectories experienced in triaxial and hollow cylinder tests. A FORTRAN code (UMAT subroutine) was developed to incorporate the proposed constitutive model in a commercial FE package (ABAQUS). Numerical simulations were carried out aimed at evaluation of the bearing capacity of shallow foundation in transversely isotropic granular media. The numerical and experimental results were compared and showed a good agreement. Extensive parametric studies were conducted assessing the implications of introducing various simplifying assumptions in the mathematical framework. It has

been demonstrated that a reliable assessment of ultimate bearing capacity requires an adequate description of inherent anisotropy as well as that of the onset and propagation of localized deformation mode.

6.2 Recommendations for Further Work

The methodology presented here, comprising the experimental program and the constitutive modeling, can be applied to other geotechnical problems dealing with a transversely isotropic material. For example, it has been well known that the anisotropy of soil has a profound effect on the stability of natural slopes. Appropriate consideration of the anisotropy of geomaterials is also a challenge for the design and stability analysis of underground works, such as tunnels, chemical and nuclear waste storage as well as oil boreholes. In particular, wellbore instability is a serious problem that costs the petroleum industry over US$500–1000 million each year. It is reported that shales, which have a transversely isotropic structure, account for 75% of all formations drilled by the oil and gas industry, and 90% of wellbore stability problems occur in shale formations (Chen et al. 2003).

The framework presented here can be extended for the case of induced anisotropy. As mentioned before, the source of anisotropy in granular materials is the spatial arrangement of particles during the formation process (Oda and Koishikawa 1979). In the course of plastic deformation this arrangement of particles may change, thus triggering an induced anisotropy (Oda et al. 1985). For geomaterials with a weak inherent anisotropy, the induced anisotropy could become dominant. In this case, the effects of

directional dependency of material properties should be incorporated via an appropriate evolution law which couples the changes in the fabric with stress state.

BIBLIOGRAPHY

ASTM D2850–03a, Standard Test Method for Unconsolidated-Undrained Triaxial Compression Test on Cohesive Soils

ASTM D3080–04, Standard Test Method for Direct Shear Test of Soils under Consolidated-Drained Conditions.

ASTM D4767–04, Standard Test Method for Consolidated Undrained Triaxial Compression Test for Cohesive Soils

Attewell P.B. and Sandford M.R. (1974), Intrinsic shear strength of a brittle anisotropic rock I: experimental and mechanical interpretation, International Journal of Rock Mechanics and Mining Science, Vol. 11, No. 11, 423-430.

Bazant Z.P. and Lin F.B. (1988), Non-local yield limit degradation, International Journal of Numerical Methods in Engineering, Vol. 26, No. 8, 1805-1823.

Bazant Z.P. and Pijaudier-Cabot G. (1988), Nonlocal continuum damage, localization instability and convergence, Journal of Applied Mechanics, ASME, Vol. 55, No. 2, 287-293.

Boehler J.P., Applications of tensor functions in solid mechanics, Springer, 1987.

Boehler J.P. and Sawczuk A. (1970), Equilibre limite des sols anisotropes. Journ de Macanique; Vol. 3, 5-33.

Boehler J.P. and Sawezuk A. (1977), On yielding of oriented solids, Acta Mechanica, Vol. 27, No 1-4, 185-206.

Borja R.I. and Lee S.R. (1990), Cam-clay plasticity, Part I: implicit integration of elasto-plastic constitutive relations, Computer Methods in Applied Mechanics and Engineering, Vol. 78, No.1, 49-79.

Bowles J.E. (1996), Foundation analysis and design, 5th edition.

Budhu M. (2006), Soil Mechanics and Foundations, 2nd edition, John Wiley & Sons.

Chen W. F. (1975), Limit analysis and soil plasticity, Elsevier Science, Amsterdam.

Chen G., Chenevert M.E., Sharma M.M. and Yu M (2003), A study of wellbore stability in shales including poroelastic-chemical-and thermal effects, Journal of Petroleum Science and Engineering, Vol. 38, 167– 176,.

Cowin, S.C. (1986), Fabric dependence of an anisotropic strength criterion, Mech. Mater., Vol. 5, No. 3, 251-260.

Craig R.F. (2004), Craig's Soil Mechanics, 7th Edition, Spon Press.

Das B.M. (2002), Principles of Geotechnical Engineering, 5th Edition, Brooks/Cole.

Das B.M. (1999), Principles of Foundation Engineering, 4th Edition.

de Borst R. and Vermeer P.A. (1984), Possibilities and limitations of finite elements for limit analysis, Geotechnique, Vol. 34, No. 2, 199-210.

Drescher A. and Detournay E. (1993), Limit load in translational failure mechanisms for associative and non-associative materials, Geotechnique, Vol. 43, No. 3, 443–456.

Duveau G., Shao J.F. and Henry J.P. (1998), Assessment of some failure criteria for strongly anisotropic materials. Mechanics of Cohesive Frictional Materials, Vol. 3, No. 1, 1–26.

Frydman S. and Burd H.J. (1997), Numerical studies of bearing-capacity factor , Journal of Geotechnical and Geoenvironmental Engineering, ASCE, Vol. 123, No. 1, 20-29.

Graham J. and Houlsby G.T. (1983), Anisotropic elasticity of natural clay, Geotechnique, Vol. 33, No. 2, 165-180.

Graham J., Noonan M.L. and Lew K.V. (1983), Yield states and stress-strain relationship in a natural plastic clay, Canadian Geotechnical Journal, Vol. 20, No. 3, 502-516.

Griffiths D.V. (1982), Computation of bearing capacity factors using finite elements, Geotechnique, Vol. 32, No. 3, 195–202.

Griffiths D.V. (1989), Computation of collapse loads in geomechanics by finite elements, Ingenieur-Archiv, Vol. 59, No. 3 , 237- 244.

Guo P. (2008), Modified direct shear test for anisotropic strength of sand, Journal of Geotechnical and Geoenvironmental Engineering, ASCE, Vol. 134, No. 9, 1311-1318.

Head K.H. (1998), Effective Stress Tests, Volume 3, Manual of Soil Laboratory Testing, 2nd Edition, John Wiley & Sons.

Hight D. W., Gens A. and Symes M.J.P.R. (1983), The development of a new hollow cylinder apparatus for investigating the effects of principal stress rotation in soils, Geotechnique, Vol. 33, No. 4, 355-383.

Hill R. (1950), The mathematical theory of plasticity. Oxford University Press.

Hoek E. (1983), Strength of jointed rock masses. Geotechnique, Vol. 33, No. 3, 187-205.

Hoek E. and Brown E.T. (1980), Empirical strength criterion for rock masses. Journal of Geotechnical Engineering Division, ASCE, Vol. 106, No. 9, 1013-1035.

Hofstetter G., Simo J.C. and Taylor R.L. (1993), A modified cap model: closest point solution algorithm, Computers and Structures, Vol. 46, No. 2, 203-214.

Holtz R. and Kovacs W. (1981), An Introduction to Geotechnical Engineering, Prentice-Hall, Inc.

Jiang J. and Pietruszczak S. (1988), Convexity of yield loci for pressure sensitive materials, Computers and Geotechnics, Vol. 5, No. 1, 51-63.

Kirkgard M.M. and Lade P.V. (1991), Anisotropy of normally consolidated San Francisco bay mud, Geotechnical Testing Journal, Vol. 14, No. 3, 231-246.

Lade P.V., Nam J. and Hong W. P. (2008), Shear banding and cross-anisotropic behavior observed in laboratory sand tests with stress rotation, Canadian Geotechnical Journal, Vol. 45, No. 1, 74-84.

Lam W.K. and Tatsuoka F. (1988), Effects of initial anisotropic fabric and on strength and deformation characteristics of sand, Soils and Foundations, Vol. 28, No. 1, 89-106.

Lo K. Y. and Hori M. (1979), Deformation and strength properties of some rocks in southern Ontario, Canadian Geotechnical Journal, Vol. 16, No. 1, 108-120.

Luenberger D.G. (1984), Linear and Nonlinear Programming, Reading, Massachusetts, Addison-Wesley.

Meyerhof G. (1951), The ultimate bearing capacity of foundations, Geotechnique, Vol. 2, No. 4, 301–332.

Michalowski R.L. (1995), Slope stability analysis: A kinematical approach, Geotechnique, Vol. 45, No. 2, 283–293.

Michalowski R.L. (1997), An estimate of the influence of soil weight on bearing capacity using limit analysis, Soils and Foundations, Vol. 37, No. 4, 57–64.

Muhlhaus H.B. and Vardulakis I. (1987), the thickness of shear band in granular materials, Geotechnique, Vol. 37, No. 3, 271-283.

Nishimura S., Minh N.A. and Jardine R.J. (2007), Shear strength anisotropy of natural London clay, Geotechnique, Vol. 57, No. 1, 49-62.

Nova R. (1980), The failure of transversely anisotropic rocks in triaxial compression. Int Journal of Rock Mechanics and Mining Science & Geomech Abstr, Vol. 17, No. 6, 325-32.

Oda M. and Koishikawa I. (1979), Effect of strength anisotropy on bearing capacity of shallow footing in a Dense sand, Soils and Foundations, Vol. 19, No. 3, 15-28.

Oda M., Nemat-Nasser S. and Konishi J. (1985), Stress-induced anisotropy in granular masses, Soils and Foundations, Vol. 25, No. 3, 85-97.

Oka F., Kimoto S., Kobayashi H. and Adachi T. (2002), Anisotropic behavior of soft sedimentary rock and a constitutive model, Soils and Foundations, Vol. 42, No. 5, 59-70.

Oliver J. (1995), Continuum modeling of strong discontinuities in solid mechanics using damage models", Computational Mechanics, Vol. 17, No. 1-2, 49-63.

Oliver J., Cervera M. and Manzoli O. (1999), Strong discontinuities and continuum plasticity models: the strong discontinuity approach, International Journal of Plasticity, Vol. 15, No. 3, 319-351.

Oliver J. and Huespe A.E. (2004), Continuum approach to material failure in strong discontinuity settings, Computer Methods in Applied Mechanics and Engineering, Vol. 193, No. 30-32, 3195–3220.

Oritz M. and Popov E.P. (1985), Accuracy and stability of integration algorithms for elastoplastic constitutive relations, International Journal of Numerical Methods in Engineering, Vol. 21, No. 9, 1561-1576.

Owen D.R.J. and Hinton E. (1980), Finite Elements in Plasticity- Theory and Practice Pineridge Press, Swansea.

Pasternack S. and Timmerman D. (1986), On the numerical implementation of an elastoplastic two surface material model, Computers and Geotechnics, Vol. 2, No. 5, 275-307.

Pietruszczak S. (1999), On homogeneous and localized deformation in water-infiltrated soils, Journal of Damage Mechanics, Vol. 8, No. 3, 233-253.

Pietruszczak S. (1999), On inelastic behaviour of anisotropic frictional materials, Mechanics of Cohesive Frictional Materials, Vol. 4, No. 3, 281-293.

Pietruszczak S., Lydzba D. and Shao J.F. (2002), Modelling of inherent anisotropy in sedimentary rocks, International Journal of Solids and Structures, Vol. 39, No. 3, 637–648.

Pietruszczak S. and Mroz Z. (1981), Finite element analysis of strain softening materials, International Journal of Numerical Methods in Engineering, Vol. 17, No. 3, 327-334.

Pietruszczak S. and Mroz, Z. (2001), On failure criteria for anisotropic cohesive-frictional materials, International Journal for Numerical and Analytical Methods in Geomechanics, Vol. 25, No. 5, 509-524.

Pietruszczak S. and Niu X. (1993), On the discribtion of localized deformation, International Journal for Numerical and Analytical Methods in Geomechanics, Vol. 17, No. 11, 791-805.

Pietruszczak S. and Pande G.N. (2001), Description of soil anisotropy based on multi-laminate framework, International Journal for Numerical and Analytical Methods in Geomechanics, Vol. 5, No. 2, 197-206.

Renegar J. (2001), A mathematical view of interior-point methods in convex optimizations, Society of Industrial and Applied Mathematics (SIAM).

Rudnicki J.W. and Rice J.R. (1975), Conditions for the localization of deformation in pressure-sensitive dilatant materials, Journal of Mechanics and Physics of Solids, Vol. 23, No. 6, 371–394.

Runesson K., Ottosen N.S., Peric D. (1991), Discontinuous bifurcations of elastic-plastic solutions at phase stress and plane strain. International Journal of Plasticity, Vol. 7, No. 1, 99-121.

Saada A.S. (1988), State-of-the-art: Hollow cylinder torsional device: their advantage and limitations, Advanced Triaxial testing of Soils and Rocks, ASTM STP977, Robert T. Donaghe, Roald C. Chaney and Marshall L. Silver, Eds., American Society for testing and Materials, Philadelphia, 766-795.

Saada A.S. (1993), Elasticity; Theory and Applications, 2nd edition, published by Krieger Publishing Company, Pergamon Press Inc.

Saada A.S. (2000), Laboratory testing for the validation of constitutive models, in: Modeling in Geomechanics, Eds. Zaman, Gioda nad Booker, John Wiley & Sons, LTD.

Sarama S.K. and Iossifelis I.S. (1990), Seismic bearing capacity factors of shallow strip footings, Geotechnique, Vol. 40, No. 2, 265– 273.

Siddiquee M.S.A., Tatsouka F., Tanaka T., Tani K., Yoshida K. and Morimoto T. (2001), Model tests and FEM simulation of some factors affecting the bearing capacity of a footing on sand, Soils and Foundations, Vol. 41, No. 2, 53-76.

Simo J.C. and Hughes T.J.R. (1998), Computational Inelasticity, Springer Verlag.

Simo J.C., Kennedy J.G. and Govindgee S. (1988), Non-smooth multisurface plasticity and viscoplasticity. Loading/unloading conditions and numerical algorithms, International Journal of Numerical Methods in Engineering, Vol. 26, No. 10, 2161-2185.

Simo J.C., Oliver J. and Armero F. (1993), An analysis of strong discontinuities induced by strain-softening in rate-independent inelastic solids, Computational Mechanics, Vol. 12, No. 5, 277-296.

Simo J.C. and Taylor R.L. (1985), Consistent tangent operator for rate-independent elastoplasticity, Computer Methods in Applied Mechanics and Engineering, Vol. 48, No. 1, 101-118.

Sloan S.W. and Randolph M.F. (1982), Numerical prediction of collapse loads using finite element method, International Journal for Numerical and Analytical Methods in Geomechanics, Vol. 6, No. 1, 47-76.

Soil mechanics laboratory instruction, McMaster University, Department of Civil Engineering: Direct Shear test.

Soil mechanics laboratory instruction, McMaster University, Department of Civil Engineering: Triaxial test.

Symes M. J. P. R., Gens A., and Hight D.W. (1984), Undrained anisotropy and principal stress rotation in saturated sand, Geotechnique, Vol. 34, No.1, 11-27.

Terzaghi K. (1943), Theoretical soil mechanics, Wiley, New York.

Timoshenko S.P. and Goodier J.N. (1970), Theory of Elasticity, McGraw-Hill.

Triantafyllidis N. and Aifantis E.C. (1986), A gradient approach to localization of deformation. I. Hyperelastic materials, Journal of Elasticity, Vol. 16, No. 3, 225-237.

Tsai S.W. and Wu E. (1971), A general theory of strength of anisotropic materials. J Journal of Composite Materials, Vol. 5, No. 1, 58-80.

Ukritchon B., Whittle A.J. and Klangvijit C. (2003), Calculations of bearing capacity factor using numerical limit analysis, Journal of Geotechnical and Geoenvironmental Engineering, ASCE, Vol. 129, No. 6, 468–474.

Vaid Y.P., Eliadorani A., Sivathayalan S., and Uthayakumar M. (2001), Laboratory Characterization of Stress-Strain Behavior of Soils by Stress and/or Strain Path Loading, Geotechnical Testing Journal, Vol. 24, No. 2, 200–208.

Vardoulakis I. and Sulem J. (1995), Bifurcation Analysis in Geomechanics, Blackie Academic and Professional.

Vermeer P.A. (1978), A double hardening model for sand, Geotechnique, Vol. 28, No. 4, 413-433.

Walsh J.B. and Brace J.F. (1964), A fracture criterion for brittle anisotropic rock. Journal of Geophysical Research, Vol. 69, No. 16, 3449-3456.

Woodward P.K. and Griffiths D.V. (1998), Observations on the bearing capacity factor by finite elements, Geotechnique, Vol. 48, No. 1, 137-141.

Yamada Y. and Ishihara K. (1979), Anisotropic deformation characteristics of sand under three dimensional conditions, Soils and Foundations, Vol. 19, No. 2, 79-94.

Yin Jian-Hua, Wang Yu-Jie and Selvadurai A.P.S. (2001), Influence of nonassociativity on the bearing capacity of a strip footing, Journal of Geotechnical and Geoenvironmental Engineering, ASCE, Vol. 127, No. 11, 985-989.

Yoshimine M., Ishihara K. and Vargas W. (1998). Effects of principal stress direction and intermediate principal stress on undrained shear behaviour of sand. Soils Found. 38(3), 179–188.